Polarization maintaining and phase retarding properties of a birefringence controlled plastic optical fiber

Rei Athena Furukawa

A thesis submitted in partial fulfillment
of the requirements for the degree of

PhD (Engineering)

Keio University

2009

Program Authorized to Offer Degree: School of Integrated Design Engineering

Keio University

Abstract

Polarization maintaining and phase retarding properties of a birefringence controlled plastic optical fiber

Rei Athena Furukawa

Chair of the Supervisory Committee:
Professor Yasuhiro Koike
School of Integrated Design Engineering

The proposed work is a partial assembly of the technologies of the birefringence-reduced copolymer and the plastic optical fiber (POF). POF with P(MMA/BzMA) (copolymer of methyl methacrylate and benzyl methacrylate) core was experimentally investigated in terms of birefringence affection to the multimodal fiber optic waveguiding of polarized light. This dissertation investigates the unique application of P(MMA/BzMA), as a suitable material for fabricating a polarization-maintaining multimode fiber (MMF). As a result, extinction ratio of 14 dB was measured from 1 m P(MMA/BzMA)POF. The polarization-maintaining principle of the new fiber was discussed in the aspects of fiber mode and Gaussian beam. As a phase retarder, clear optical axis was observed when the fiber was bent and was under a vertical stress. Based on the properties mentioned above, a pressure sensor with a novel principle was proposed using the P(MMA/BzMA)POF. Structure simplification of the interferometric fiber optic sensor was succeeded by replacing the conventional dual SMF structure with an employment of one P(MMA/BzMA)POF. The preliminary model had demonstrated polarimetric sensitivity of 1.56×10^{-5} (MPa^{-1}) and dynamic range up to 0.45 MPa.

TABLE OF CONTENTS

LIST OF FIGURES

LIST OF TABLES

Table Number Page

ACKNOWLEDGMENTS

The presented work was supported by the Japan Science and Technology Agency ERATO-SORST Koike Photonics Polymer Project. The author wishes to express sincere appreciation to: Professors Yasuhiro Koike and Akihiro Tagaya for the opportunity of this interest-dragging research, former/current members in Koike's and Ishigure's groups for helps and trainings with measurements, YS Kagaku and Sanyo Rika for preparing equipments, Mr. Ogawa (Iwaken) for helps regarding polarized optical microscope, all the fiber manufacturers whom provided excellent products, and secretaries in Koike's group for making entire things smooth. The author wishes to express sincere appreciation to Professors Yoshinori Matsumoto, Hiroyuki Tsuda, and Naoaki Yamanaka (alphabetical) for fruitful comments regarding research and life as well as their favor of being the reading committee of this dissertation.

The author is grateful to the School of Integrated Design Engineering and the 21st century COE program for a kind mentor throughout the PhD program. The author would especially like to express the sincerest appreciation to her friends and family who kept her sane through the process.

The author wishes to express sincere appreciation to University of Washington Computing Services, where she has had the opportunity to work with the TeX formatting system, and to the author of TeX, Donald Knuth, *il miglior fabbro*.

Chapter 1

INTRODUCTION

1.1 Preface

While transparent plastic is capable for various applications in optical devices, an optical property called birefringence[1] has been a sensitive factor that had needed to be reduced[1, 2]. Several innovations regarding birefringence elimination such as polymer blending, molecule doping, crystal doping, and copolymerization have been reported[3, 4, 5, 6, 7]. Currently, the main application of the birefringence-free plastics are the displaying panels and pickup lens for the memory device, which are typically in geometries of film, tablet, or bulk.

On the other hand, plastic optical fiber (POF), that is know by its extremely large core diameter compared to the glass fiber, has been developed for the application of telecom cables in short/mid distance wirings[8, 9]. There has been reports mentioning about improvement in bandwidth, loss, and environmental stability by modifying the structure and the material[10, 11, 12, 13].

This dissertation summarizes the achievements from a partial combination of the above two technologies, namely, phase control in a POF using the birefringence-controllable polymer, and its application to a sensor. The concept of phase control of the POF led us to two targets, which are polarization-maintaining[2] and phase retarder[3]. Some of the backgrounds of the similar products in the market, and some more detail about the research motivation is explained in this section.

---

[1] Birefringence: optical anisotropy that changes the incident polarization state. Birefringence typically exhibits during the processing of the raw material.

[2] Polarization-maintaining (general): to conserve the vibration plane of either electrical or magnetic field of the light. Polarization state refers to the oscillation direction itself.

[3] Phase: the position of repeating sinusoidal of a lightwave.

1.2 Glass-based PMFs and their applications

The definition of the conventional polarization-maintaining fiber (PMF) is that it is an optical fiber in which the polarization of linearly polarized light waves launched into the fiber is maintained during propagation with little or no cross-coupling of optical power between the polarization modes.

A typical singlemode fiber (SMF) has core and cladding that are nearly circular. The fundamental mode[4] (LP_{01}) consists of mutually perpendicular polarization modes, namely, $\mathrm{HE}_{11}^{\mathrm{x}}$ and $\mathrm{HE}_{11}^{\mathrm{y}}$ modes. Each are linearly polarized into x and y directions (both in radial), respectively. The difference in propagation constants of these modes ($\Delta\beta = \beta_x - \beta_y$) are zero if the core and cladding are perfectly circular and completely stress-free, however, it is very difficult to achieve such structure even with the latest fabrication technology. Because of this intrinsic birefringence in which originated from geometry and stress anisotropy, $\mathrm{HE}_{11}^{\mathrm{x}}$ and $\mathrm{HE}_{11}^{\mathrm{y}}$ modes that is propagating in slightly different speed are likely to cause mode coupling. This mode coupling occurs periodically, which is expressed by beat length ($L_b = 2\pi/\Delta\beta$). Even with the SMF fabricated with the most sensitive care in geometry and stress, the achievable beat length is still around 15 m[14]. Hence, ordinary axially symmetrical SMFs hardly be able to maintain state of polarization because its LP_{01} mode is subject to the considerable fluctuation such as temperature, pressure, or vibration changes that are given only in slight changes in ambient conditions[15].

1.2.1 Large birefringence PMF

The fluctuation of the LP_{01} mode had been prevented or reduced in two ways[16]. One is to devise an axially asymmetric structure in which one of the two modes is cut off. Another method is have the $\Delta\beta$ very large so that the mode coupling hardly occurs. In order to obtain these property(ies), polarization maintaining fibers (PMFs) with axially asymmetric cross sections were invented. The left part of Figure 1.1 shows the variety of the structure of the highly birefringent type PMFs. Existing types of highly birefringent type PMFs are described below.

---

[4] Fiber modes: a specific solution of the wave equation that satisfies the appropriate boundary conditions. Its spatial distribution does not change with propagation. Structure of SMF has only one solution, which is called fundamental mode. Refer Section 2.3.2 for stricter explanations.

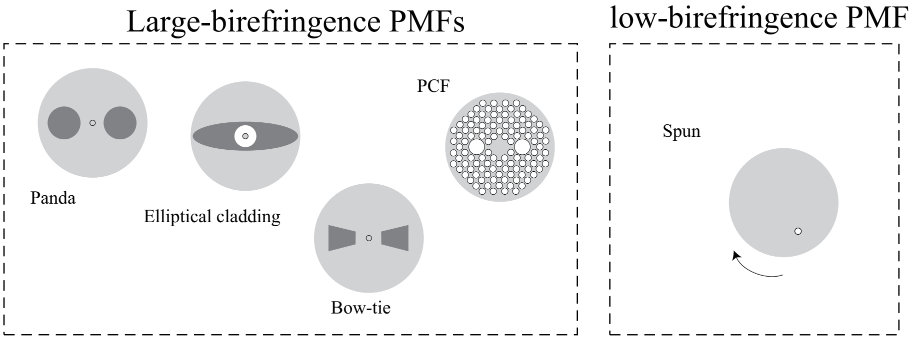

Figure 1.1: Structures of conventional PMFs

PANDA style fiber

PANDA (Polarization Maintaining and Absorption Reducing Fiber) type was produced by NTT (Nippon Telegraph and Telephone Co.) and Fujikura Ltd.[17]. It maintains polarization using round and symmetrical stress rods on either side of the core. Typical PANDA fiber has the polarization maintaining performance of 23 dB extinction ratio (ER) and 6 mm beat length[5]. Originally developed for the telecommunications industry, PMFs including the PANDA type filled the need for low-cost, high-volume, high-reproducibility fiber. Recently, specialty-fiber companies have introduced a variety of product developments aimed at diverse markets such as fiber-optic gyros and high-power fiber lasers. The technology is now being applied outside telecom to a new family of fiber products, which includes high-birefringence fibers for fiber optic sensors, such as the fiber gyro, as well as polarizing-fiber designs for linearly polarized fiber lasers.

Bow-tie

Bow-tie (sidepit) type is known as the PMF produced from Furukawa Denki Co., Ltd.[18]. ER of -25 dB and beat length of 6.3 mm is reported from this type. Those properties are said to be similar to the PANDA.

---

[5] Extinction ratio and beat length: parameters used to evaluate polarization-maintaining property of conventional SM-PMFs. Details are explained in Sections 2.4.2 and 3.5.1.

Elliptical cladding

Elliptical cladding type was produced by Hitachi Wire Ltd.[19]. Elliptical cladding type had a feature of lowest loss ever reported (0.8 dB/km at 1.55 μm) at the time when it was first reported[15], however, it isn't true anymore. This feature was precious at the time when PMFs were dragging attention as a telecom medium. ER of 30 dB and beat length of 2 mm were reported from this type. It has higher polarization-maintaining property compared to PANDA and bow-tie types.

Non-circular core

A high $\Delta\beta$ could also be obtained by deforming the optical fiber into an elliptical shape. Some numerical modeling of the birefringence distribution and phase retardation of this type were reported[20, 21]. Experimental studies on the birefringence measurement of elliptical core SMF was also reported[22]. However, this type was not popularly used in the practical application than the other types.

PCF

The same function as the above types can be obtained using a photonic crystal fiber (PCF)[23]. PCF is a class of optical fiber based on the properties of photonic crystals[24]. Because of its ability to confine light in hollow cores or with confinement characteristics not possible in conventional optical fiber, PCF is finding applications in telecom, fiber lasers, nonlinear devices, high-power transmission, highly sensitive gas sensors, and other areas.

PCFs have holes arranged regularly in the claddings as shown in Figure 1.1. Light propagates on the defect, missing air-holes, through the core by total internal reflections. The guiding mode of PCFs change drastically by the air-hole structure, such as hole diameter and pitch, therefore, optical properties of PCFs, such as dispersion and nonlinearity, are more controllable than the conventional fibers[25].

Another noteworthy characteristic of PCFs is their strong birefringence, which is induced by the size and arrangement of the air holes. Theoretical analysis[26] and experiments [27, 28] showed high birefringence of the order of 1×10^{-3}, which is three times larger than that of conventional PMFs.

Suzuki had demonstrated excellence of stability in polarization maintaining property under twisting and macrobending using PM-PCF compared to the conventional types[28]. The affect of temperature is similar compared to the other fibers.

1.2.2 Low birefringence PMF

A new type of PMF that covers several inconvenience of the large birefringence type is also in the market. A low birefringence spun fiber [29, 30, 31] is a PMF that is commercialized by IVG Fiber Ltd.. The polarization-maintaining mechanism of the spun fiber is described precisely in Section 2.4.3. This fiber has its internal birefringence averaged out by intentionally creating geometrical dissymmetry. Therefore, it performs as a low birefringence core that can transmit any state of polarization. Because of this unique design, the low birefringence PMF has several additional functions that the large birefringence PMFs could never have, such as the one mentioned above. However, because the preform-spinning technique[6] is only developed in the glass based fibers, the core diameter is still small as to require a highly accurate light coupling technique. Furthermore, because the position of core distributes differently in the fiber cross section depending on the fiber length, the spun fiber may have an extreme difficulty in ferruling and cabling procedure, which should require an extra effort of securing the light path. Despite such unsolved inconveniences, the application of the spun fiber is dramatically large in especially the sensor field such that uses gratings[7][32].

1.3 Characteristics of plastic optical fibers

Although it has nothing to do with the earlier topic of polarization-maintaining, background of POF also needs to be mentioned in this section.

The first POF was first manufactured by DuPont in the late sixties[33]. The expected market of the POF was short/medium length telecom wirings with an expectation to have an optimum balance of data speed and cost performance compared to the copper wire or the glass fibers. One of the strength that reduces the cost of a POF network is its ease in light coupling. Because of the elastic intrinsic of the plastic, fibers made in a large diameter ($\approx$ 1000 μm) is still bendable, whereas the

---

[6] It is how the IVG Fiber makes dissymmetrical core structure. ”Preform” is a state of fiber before heat drawing procedure.

[7] Gratings (optics): a diffraction based optical component

Table 1.1: Possible monomers for POF base material

abbreviation	**full name**	**refractive index**
MMA	methyl methacrylate	n=1.492
VPAc	vinyl-phenylacetate	n=1.567
VB	vinyl benzoate	n=1.576
PhMA	phenyl methacrylate	n=1.570
BzMA	benzyl methacrylate	n=1.562

largest glass fiber diameter is 62 μm. The large core diameter is a powerful factor in making cheep light connections because it do not require lens and therefore the system is highly robust.

The material most frequently used for POF is the thermoplastics poly-methyl methacrylate (PMMA). PMMA is an organic compound forming long chains with typical molecular weight around 10^5. Essential from the point of view of optical transparency of the material is the amorphous structure of the polymerized material. The refractive index of PMMA is 1.492 and the glass transition temperature T_g lies between 95 and 125 ℃. According to the reference [33], the possible monomers (and their refractive index n) for the POF is as shown in Table 1.1.

To the advantage of large core, POF is typically a multimode fiber (MMF). The wave propagation of MMF is explained as to the comparison to the SMF later in Section 2.3. The practical difference is their bandwidths. Because of the mode dispersion [34], MMF cannot transmit as large amount of information as the SMF.

To attack this bandwidth problem, refractive index modification was done in the MMF development history. The graded index (GI) profile was invented in order to enhance the bandwidth than the classical step index (SI) type[8].

---

[8] Refer Section 2.2 for the detail explanation of GI and SI refractive index profiles

1.4 Proposal of a multimode PMF using POF technology

Having discussed about the brief backgrounds on PMF and POF, one motivation of the innovation regarding this dissertation can be now stated.

The typical largely birefringent SM-PMFs have inconvenience in common such are: (1) the system requires polarization matching (procedure to match the polarization vibration to the optical axis[9] of the fiber), (2) the fiber can maintain only linear polarization state (no circular nor elliptical), and (3) an expensive lens system is required for the light couplings. These types of PMFs are used in telecom to enhance bandwidth by avoiding polarization-mode dispersion[10].

In this dissertation, a copolymer fiber with a low birefringence core was fabricated at the purpose develop the first multimode PMF ever reported. The first part of Chapter 3 describes the procedure to fabricate a POF in which the core birefringence is successfully low. The P(MMA/BzMA)POF transmits polarized light in a similar manner as the spun fiber, but the way of reducing the birefringence is different from that. As mentioned in the very beginning of this section, the copolymer employed in this study was originally developed as a birefringence-free transparent material that is immune from extrusion or drawing[35]. This pair of monomers, methyl methacrylate and benzyl methacrylate, are uniquely suited in the purpose of fabricating the POF because, (1) both are in the list of possible monomers to fabricate a POF (Table 1.1), (2) it makes GI profile (detail mechanism is described in section 3.2), and (3) enables birefringence reduction.

Some of the notable characteristics that the P(MMA/BzMA)POF may have as in comparison to the known PMFs are listed below.

1. Easy to couple light
2. Capable of maintaining any kinds of polarization states
3. Capable in transmitting phase information
4. No need of polarization matching

---

[9] Optical axis (in terms of fiber-optics): direction in which one of the LP_{01} component vibrates

[10] Polarization-mode dispersion: explained in section 2.4.3)

It is already noted that POFs are fabricated into large diameters compared to the glass fibers, where the P(MMA/BzMA)POF is not an exception. Hence, capability of easy light coupling is one characteristic of the P(MMA/BzMA)POF. In the same way as the spun fiber, the P(MMA/BzMA)POF uses the polarization-maintaining principle by reducing the core birefringence. Such design allows the fiber to maintaining any kinds of polarization states during the propagation, whereas the old design of large birefringence core maintains only linear polarization. Thus, the P(MMA/BzMA)POF is capable in transmitting phase information and also it do not require the polarization matching at the input.

Here, the definition of ”polarization-maintaining” needs to be clarified.

In the case of high birefringence PMFs such as PANDA and bow-tie, linear polarization that is matched to the stress axis is successfully maintained. This case, the meaning of ”polarization-maintaining” is to avoid the affection of the unneeded orthogonal mode by avoiding mode coupling or by intentionally absorbing the orthogonal component.

The polarization-maintaining phenomenon may have different physical meaning for the low birefringence large-core MMF. First, the likeliness of breakage of LP_{01} degeneracy[11] is different from the case of SMF. The detailed model when maintaining linear and non-circular polarization states are explained in Chapter 2 with discussion of LP and hybrid modes.

Second, a large-core MMF is considered not to exhibit a clear optical axis in a small fluctuation of structure or outer stress, which are of the magnitude that may cause breakage of HE_{11} degeneracy in a SMF. Polarization phenomena is considered to exhibit differently when the core is larger since it is defined as an electric dipole in a unit volume. In other words, when the volume is larger, the manner of polarization is not uniform along the core compared to the case when it is small. Especially in polymers, since they have larger molecular unit compared to the silicon-oxygen based amorphous of the glass, the local dipole exhibits in a coarser manner. When the core birefringence is reduced, there is even less chance to exhibit optical axis.

To experimentally clarify the above points, polarization-maintaining property of the P(MMA/BzMA)POF was characterized as follows. Chapter 4 describes the modal characterization of polarization-maintaining

---

[11] LP_{01} is a degeneracy of HE^{x}_{11} and HE^{y}_{11}. Section 2.3.3 tells more.

property since the copolymer fiber is a MMF. In Chapter 5, influence of photoelastic effect to the polarization-maintaining property was characterized using fiber macrobending.

1.5 Fiber optic pressure sensors

To the another famous application of the optical fiber besides telecom, fiber-optic (FO) sensors are becoming popular because of some benefits such as listed below[36].

1. Small and lightweight
2. Allow access into normally inaccessible areas (often embedded)
3. Passive (non-electrical)
4. Inexpensive
5. Rugged/reliable
6. Easy to install
7. Highly sensitive
8. Accurate over a wide dynamic range
9. Resistant to ionizing radiation
10. Capable of being multiplexed
11. Capable of distributed measurements

On the other hand, the expressed concerns about the FO sensors are fragility, ingress/egress difficulty, nonlinear output, complexity, reliability, and others. The bottom line is that FO sensors vary widely in their material and composition in which each offering different value propositions on sensitivity, dynamic range, size, shape, and etc[36].

FO sensors can be classified into two groups[36]. The first one is intrinsic sensor group. Intrinsic FO sensor has the fiber itself acts as the sensing medium, i.e., the propagating light never leaves the fiber and is altered in some way by an external phenomenon. The second one is the extrinsic sensor group in which the fiber merely acts as a light delivery and collection system, i.e., the propagating light that leaves the fiber, is altered in some way, and is collected by the same (or another) fiber.

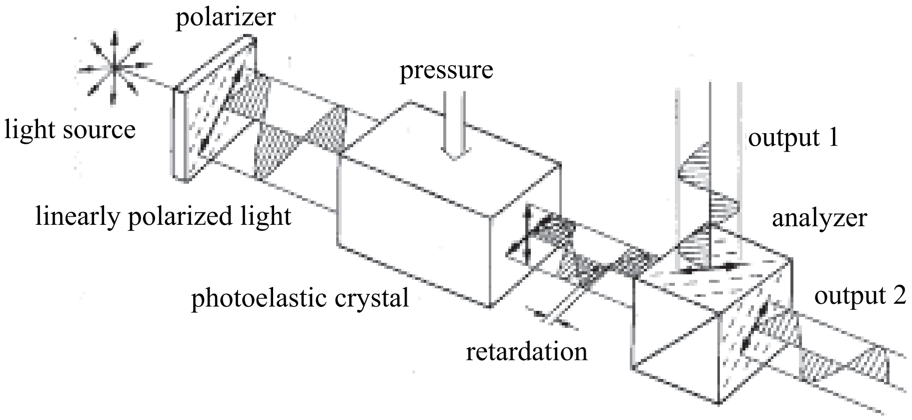

Figure 1.2: Schematic of the FO pressure sensor using photoelastic crystal[37]

The area of sensing subject of the FO sensor varies widely. They are used for measuring electro/magnetic field, temperature, chemical substance, liquid/gas level, pH level, spectroscopy, ionizing radiation, mechanical displacement, vibration frequency, acceleration, pressure, and etc.

Pressure sensing system in which uses the full advantage of FO sensor is becoming popular. Structure monitoring by the fibers-embedded structure is one example. Since a pressure sensing using the P(MMA/BzMA)POF is mentioned in the last part of this dissertation, related backgrounds on FO pressure sensor also need to be explained in this section. Some typical types of known FO pressure sensors and their characteristics are explained below.

1.5.1 FO sensor using photoelastic crystal

Photoelastic effect is a phenomena that a transparent material acts as an birefringent crystal when stress was applied to one direction. A FO pressure sensor using this phenomenon has been proposed and already in the market[37].

As shown in Figure 1.2, between the pair of fibers with attached rod lens, a polarizer, a photoelastic material, and an analyzer (another polarizer) are placed. Typically, PYREX (Corning) or fused silica in 6 mm thickness are used as the photoelastic crystal. In the commercialized model from Mitsubishi Electric, glass-based step-index multimode fiber (SI-MMF) is used with 0.82 μm-wavelength light emitting diode (LED) and Si pin-photo diode (PD) as the light source and detector, respectively.

The detection mechanism is as follows. Coupled light from the LED to the fiber collimates by the rod lens, then be linearly polarized by the first polarizer. While the polarized light propagates through the photoelastic medium, the applied pressure that is designed to orient 45 ° to the ray vibration turns to elliptical polarization state depending on the magnitude of the birefringence of the medium. The output light is analyzed by the analyzer, be collected by the second rod lens, and be carried through the second MMF to the detector.

The reported performance of this sensor is, dynamic range: 10^3 - 10^6 Pa; precision: ± 1%; temperature affection: < ± 2 % (at -20 to 80 ℃). Theoretically, the measurable minimum pressure is 1.4 Pa[38]. Precision has been improved by a numerical processing using the two powers obtained at the output (Figure 1.2).

Fluctuation of the LED output or misalignment of the ray path are known to be the noise factors. In the aspect of device structure, the sensor needs to be designed to have the pressure applied homogeneously to the photoelastic medium.

1.5.2 Refection-based FO sensor using diaphragm

The types shown in Figure 1.3 are FO pressure sensor using reflected light from the diaphragm.

The first example (Figure 1.3 (a)) consists of three fibers, where the two are used as the input and the one is for the detection. Differently modulated light signals are respectively transmitted through the two input fibers. The reflected light from both fibers are captured by the detection fiber and be analyzed separately after the signal detection. The relationship of two signals provides the pressure value. Sensitivity of $5P \times 10^{-6}$ μ m/mbar ($P[\mu$W] is the input power) is reported from this type[39].

The one shown in Figure 1.3 (b) is another sensor design using diaphragm. The end of fiber bundle that consists of input and output fibers is placed facing the stainless diaphragm with a small spacing in between (d = 0.12 mm). The applied stress on the probe end deforms the diaphragm and changes the amount of reflecting light that goes into the detection fiber. The famous application of

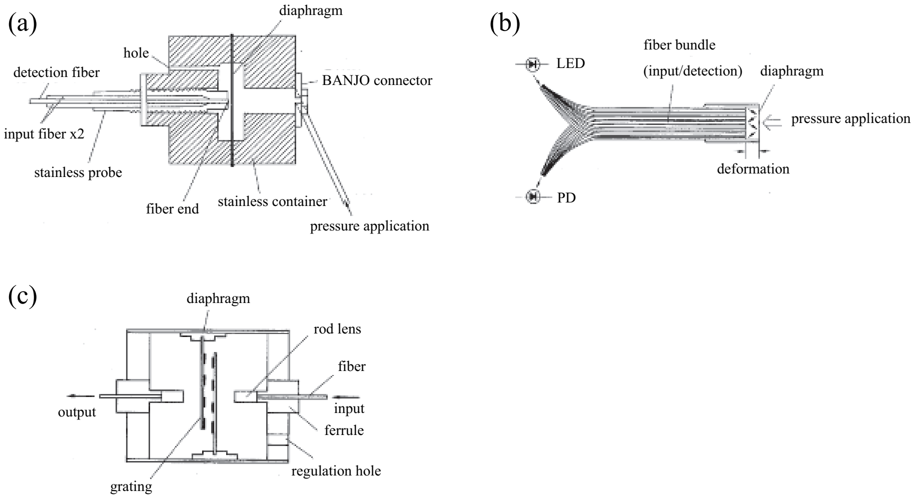

Figure 1.3: Schematic of the FO pressure sensor using diaphragm[37]

this sensor type is fluid level (e.g., blood pressure) measurement. A sensitivity less than 2.6 $\times 10^3$ Pa is reported from this type[37].

The type described in Figure 1.3 (c) that uses grating as a combination with the diaphragm is known to be capable in measuring pressure, vibration acceleration, and acoustic vibration. The grating bar that is placed perpendicularly to the ray path changes position as the pressure is applied to the diaphragm. As a result, the amount of light that passes through the grating pattern changes. In practical, minimum 50 dB (1μmPa) detection is reported by a hydrophone using 5 μm pitch grating[40].

1.5.3 Mach-Zehnder interferometry FO sensors

Phase of the light that is traveling down a SMF is sensitive to the photoelastic effect that is caused by stress or deformation such as bending. Such phase shift could be detected in a precise manner by configuring an interferometer.

The one illustrated in Figure 1.4 (a) is a fiber optic hydrophone using Mach-Zehnder interferometry. Respective beams that are split from a single output are coupled to working and reference

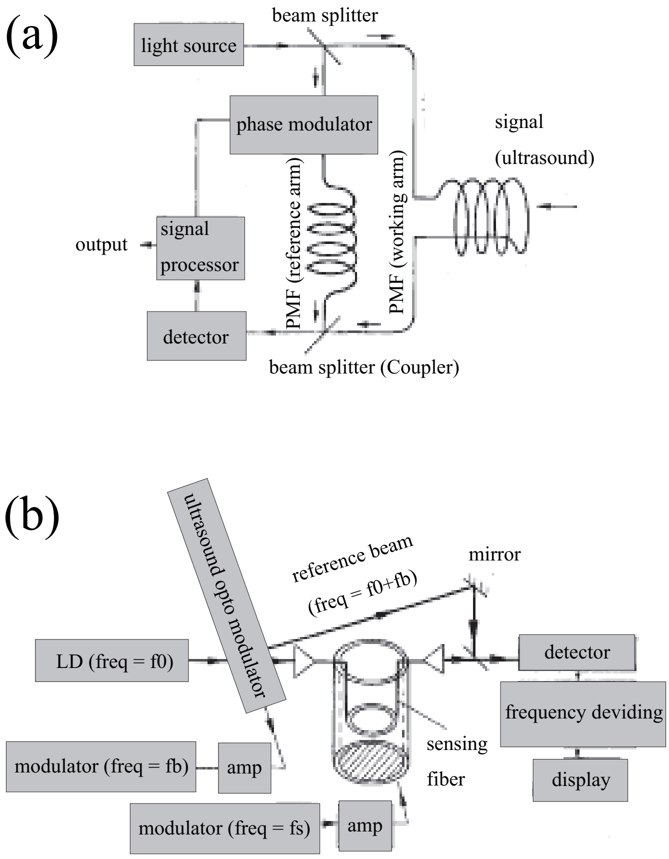

Figure 1.4: Schematic of the FO interferometric sensor[37]

fibers that are winded into loops. A phase shift generates when an acoustic vibration is applied to the working fiber. This phase shift is detected in a high precision by homodyne detection of the two path. The minimum acoustic vibration that could be detected using He-Ne laser with power regulated to provide 1 mW at the detection is 3.9 dB (1 μPa)[41]. Here, 100-m non-jacketed fused-silica SM-PMF is used.

Figure 1.4 (b) shows the FO hydrophone using heterodyne optical detection. PMF (core/cladding diameters = 4.5/80 μm, loss = 5 dB/km) is used only for the working arm. The minimum detectable

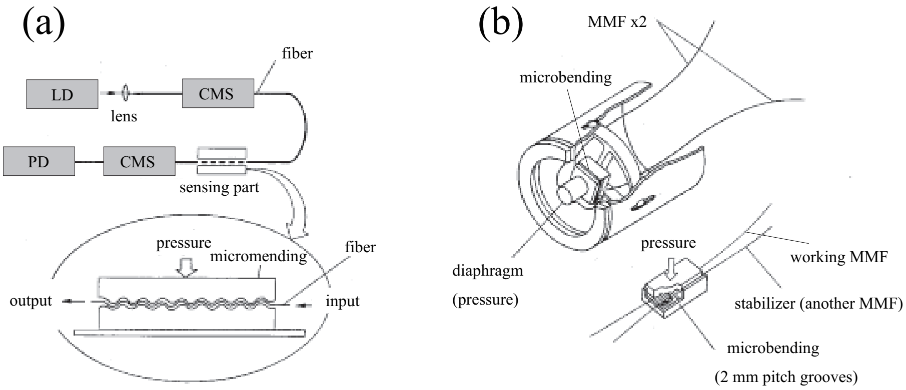

Figure 1.5: Schematic of the pressure sensor using fiber microbending[37]

acoustic pressure is 20 dB (1 μPa) at 100-1200 Hz frequency range when using a device with fiber length = 3 m, coil diameter = 7 cm, He-Ne laser of 1 μW power and 1 Hz bandwidth, and 11 MHz optical modulator[42].

1.5.4 *Microbending FO sensors*

A type of FO pressure sensor using microbending uses microbending loss for the pressure detection. Figure 1.5 (a) shows the brief mechanism. The amount of loss originated by pushing the periodic groove responds sensitively to the applied pressure.

Figure 1.5 (b) shows the actual design of a known model of pressure/acoustic sensor. Two MMFs are sandwiched between plates with ten metallic cylinders attached in 2 mm pitch. The position of the plate changes as the pressure is applied to the diaphragm, which practically is the other end of the plate, resulting the power change at the detection part representing the pressure change.

The minimum detectable pressure is 42 dB (1.3×10^{-4} Pa) using MMF of NA=0.2, He-Ne laser of 1 mW power, 1 Hz detection bandwidth, and 15 cm^2 detection area. Another model with 20 mm groove pitch, 10 time microbending, 1.3 cm^2 detection area had reported minimum sensitivity of 95 dB (1 μPa) for 1.1 kHz acoustic signal[43].

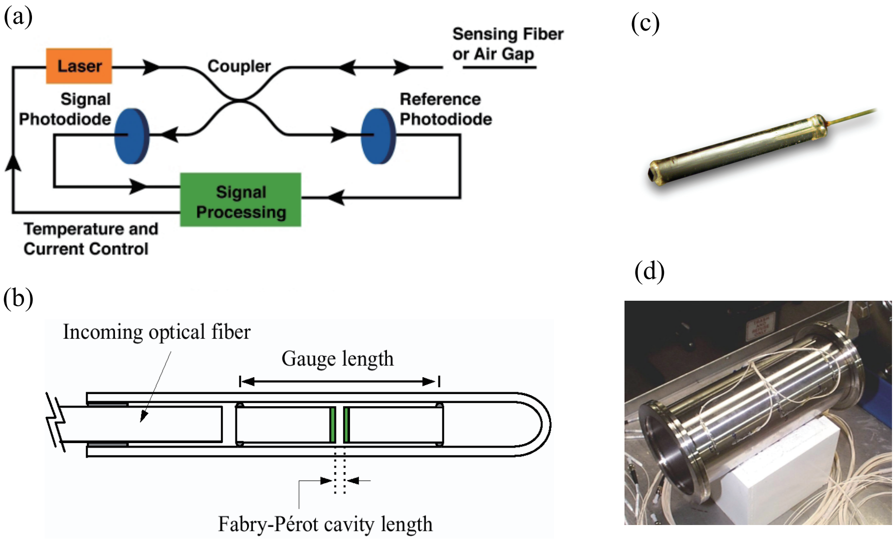

Figure 1.6: (a)Detection mechanism using Fabry-Perot structure[36], (b)Design of Fabry-Perot strain sensor from FISO Tech. Inc.[36], (c)Pressure sensor model FOP-MH from FISO Tech. Inc.[36], (d)Metal canister instrumented with Fabry-Perot strain gauges attached[36].

1.5.5 Fabry-Perot interferometry FO sensors

Fabry-Perot interferometry uses the length difference of two beams. As shown in Figure 1.6 (a), a design of FO pressure sensor which uses the Fabry-Perot interferometry based on the change in gap length has been reported. The pressure (or strain) is obtained by the interference of the reference path and reflected light at the gap. This structure could be also applied for sensing temperature by changing the gap design.

Figure 1.6 (b)(c) shows the design of the commercially available Fabry-Perot FO strain sensor produced by FISO Technologies Inc.. This model has advantage for size reduction as to be applied for biomedical applications[44]. Performance of; dynamic range: 020.7 MPa, resolution: 0.1% of full scale, and accuracy; 1% of full scale is reported from model FOP-MH (FISO Tech. Inc.)[44].

Fabry-Perot type is capable for monitoring deformation of a large structure/container by being embedded/instrumented shown in Figure 1.6(d). Although typical fiber type used for the Fabry-Perot FO sensor is SMF, some using MMF are also being reported recently[44].

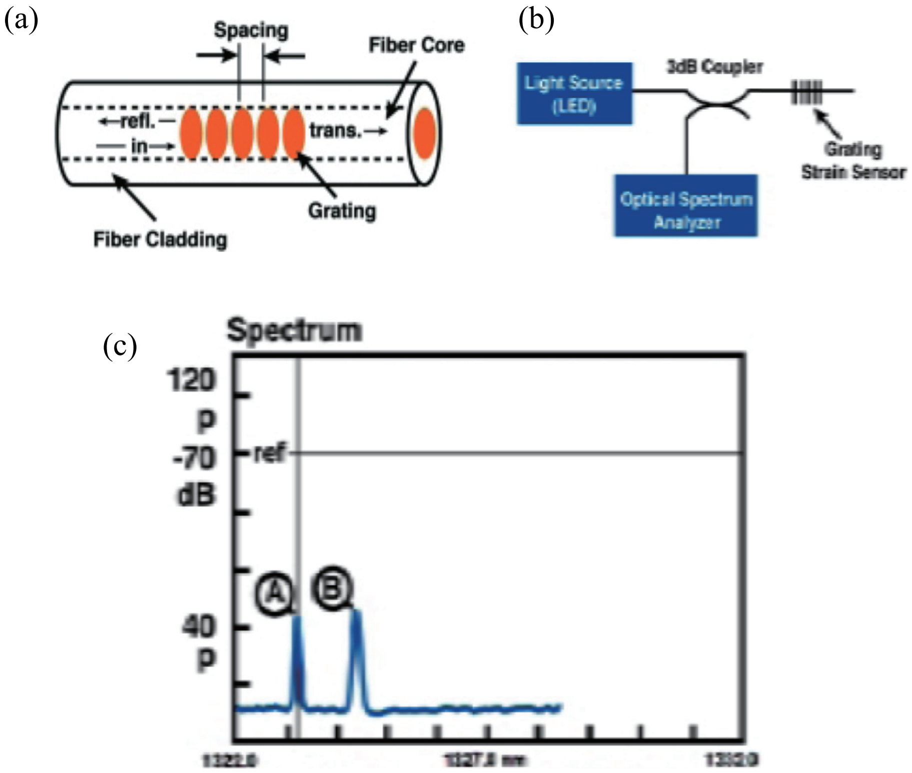

Figure 1.7: Schematic of gratings[36] (a) and instrumentation[45] (b) of the FBG sensor. (c) Typical wavelength shift (from point A to B) as a result of strain on FBG sensor[36].

1.5.6 Fiber Bragg grating (FBG) pressure sensor

As shown in Figure 1.7, corresponding wavelength component reflects back depending on the grating pitch. By having the grating to be changeable depending on the applied pressure, magnitude of the pressure and also its position can be detected from the spectrum and pulse broadening, respectively.

The fiber Bragg grating (FBG) sensor as such has advantage such as multipoint in-line measurement capability, high sensitivity, low-cost sensors, small/light weight, linear response, and others. On the other hand, there is a concern that FBG is sensitive to more than one parameter such as temperature in this case. Another concern is that it requires relatively expensive processing equipment.

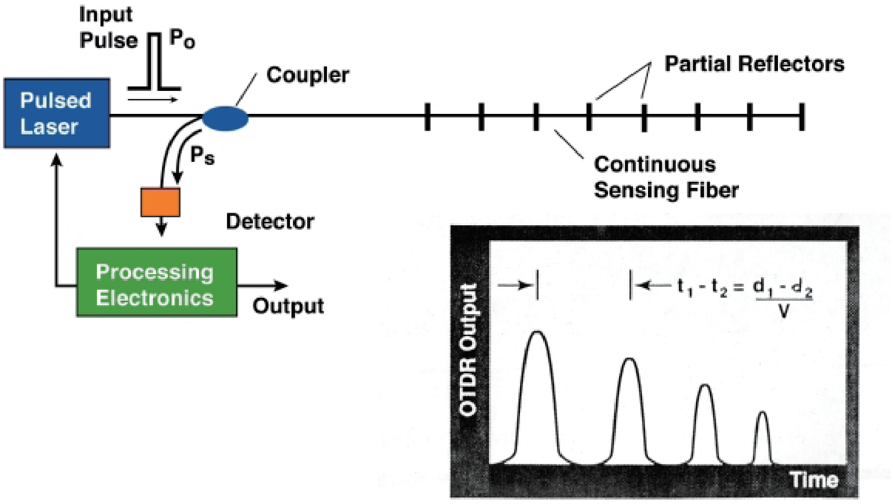

Figure 1.8: Schematic of OTDR strain detection[36]

1.5.7 *Optical time-domain reflectometer (OTDR) pressure sensor*

An optical time-domain reflectometer (OTDR) injects a series of optical pulses into the fiber. From the same end of the fiber (input side), it extracts light that is scattered and reflected back from points in the fiber where the refractive index changes (as shown in Figure 1.8). The strength of the return pulses is measured and integrated as a function of time, and is plotted as a function of fiber length.

Brillouin and Raman scatterings (stimulated) are the causes of back scattering that commonly be the subject of detection in the OTDR sensors. Brillouin scattering is the interaction between the photon and quasiparticles such as phonon and magnon that have lower frequency compared to the light. Changes in stress (acoustic mode) or temperature reflects back the input with sideband(s) with slight shift of frequency (wavelength). Raman scattering, on the other hand, occurs with the change in vibrational, rotational or electronic energy of a molecule. This phenomenon relates to the excitation in energy level that do not have the frequency exactly same as the incident (usually lower than) , which is commonly called as the inelastic scattering. Even though stimulated Brillouin and Raman scatterings are very similar in their origin, different dispersion relations for acoustic and optical phonons lead to some basic difference between the two. A fundamental difference is that Brillouin scattering in optical fiber occurs only in the backward direction whereas Raman scattering can occur in both directions[46].

In OTDR sensor, timing and broadening of the continuous pulses fed at the input tell when and where, respectively, did the deformation occurred (as shown in the time versus output graph in Figure 1.8). The Brillouin scattering OTDRs (BOTDRs) designed to monitor civil structures are reported with effective detection of strain in concrete and soil structures[47]. Strain measurement in a 10 km long sensing fiber with high accuracy is reported using the BOTDR[48]. Typically, a BOTDR can detect in a resolution of 1 m period as an average strain in that length. A Raman OTDR is typically used in a temperature monitoring of the civil structures.

1.5.8 summary

Table 1.2 summarizes the essential points of the various FO pressure sensors. First, it is noted that the MMFs tend to be used for extrinsic sensors, whereas PMF/SMF are used mainly for intrinsic sensors. Those extrinsic sensors using MMF tend to have issues with linearity of LED (or any other light source) and PD, which may require some circuit modifications for further enhancement. The intrinsic sensors that uses PMF/SMF tend to have problem with temperature affection and cost performance. However, they have strength for the capability in structure monitoring. They use pulses in order to know the position information in addition to the pressure magnitude. Embedded type sensors have benefits in general such are: embedded rather than attached, satisfactory sensitivity/dynamic range, high durability (in some cases), and compact size. On the other hand, they have concerns in common such are: difficulty in connectivity, difficulty in fabrication, strength degradation, and cost.

Table 1.2: Summarizing the essential points of the existing FO pressure (strain) sensors. (Abbreviations; DC: direct current, E: extrinsic, I: intrinsic, M: multimode, S: singlemode, PM: polarization-maintaining)

Type	**Modulation**	**Characteristic**	**Fiber (all glass-based)**	**Advantage**	**Concern**
Photoelastic crystal	DC/polarized	E, power detection	M	low temperature affection	requires accurate light coupling/linear LED
Diaphragm	DC/sinusoidal	E, power detection	M	sensitive	requires accurate light coupling
Mach-Zehnder	DC/polarized	I, interferometry	PM	sensitive	bulky, complex structure
Microbending	DC	I, power detection	M	sensitive	low consistency
Fabry-Perot	pulse/phase	E, interferometry, structure monitoring	PM (rarely M)	sensitive, small	temperature affection
FBG	pulse	I, Bragg reflection, embedded structure monitoring	S/M	multipoint-realtime detection, small	temperature affection, expensive
BOTDR	pulse	I, inelastic scattering, embedded structure monitoring	S/M	simple embedding, small	temperature affection, expensive

1.6 POF sensors

Various FO sensors based on POF have also been reported. This section summarizes designs and performances of the reported POF sensors. Advantages and disadvantages of the POF at sensor application are summarized at the end.

1.6.1 Extrinsic POF sensors

The most straightforward reason of using POF for as an extrinsic FO sensor is the ease in light coupling since POFs can be fabricated into core diameters around 1000 μm where the core of glass MMFs are 50 or 62 μm.

Reflection-based liquid level sensor using 1000 μm SIPOF is being reported[49]. Crack monitoring using two POFs with displacement in the axial distance that uses similar mechanism, a ruby florescence based temperature sensor using POF, are also being reported[50, 51].

1.6.2 Chemical POF sensors

The another characteristic of POF in the sensor point of view is the reactivity to moist and organic substances whereas the glass is highly immune to it. This sensor type typically uses the refractive index change or light leakage due to the absorption (or removal) of these substances to the POF. Thus, the sensor structure tend to be simple, which is mostly based on a simple power monitoring using DC input.

Muto's group in University of Yamanashi has developed moisture sensing system using 500 μm core SIPOF for applications such as multipoint gas sensing and health monitoring system[52, 53]. It should be noted here that the POF has a great advantage on the area of biomedical application because of its elasticity while the glass remains a concern of making wounds when broke. Some other types of POF moisture sensors with the similar principle have been reported with different designs[54]. An antibody biosensor using a microstructured POF made in TOPAS (Topas Cyclic olefin copolymers) is another example of chemical POF sensor, which uses the characteristic that the TOPAS surface can be treated to trap the antibodies[55].

1.6.3 POF pressure sensors

Two POF pressure sensors are being reported. One is POF-OTDR developed by BAM (Federal Institute for Materials Research and Testing, Berlin)[56, 57, 58, 59] and another is elongation sensor that uses two fibers with a gap in axial distance[60, 61, 50].

A POF-OTDR uses Fresnel reflection and Rayleigh scattering that are caused by the refractive index changes and microscopic inhomogeneities, respectively, as the informative backscattering light. As the spatial information is the main advantage of the OTDR, strain can be measured at different locations along a single POF over distances of some 100 m. A real-time strain/elongation monitoring was demonstrated using SIPOF, PMMA-based GIPOF, and PF(perfluorinated)-GIPOF[59]. OTDR of POF network that is woven in a textile structure has been also developed by the same group[56]. Although a comparison with the typical OTDR fabricated with glass-based fibers including the sensitivity, temperature resistance, and others is not available from their publications, some of the advantages (in addition to some famous benefits such as easy light couplings and system robustness) of the POF-OTDR could be suggested as follows. First, because POFs can be used in a bare state or with a thin-jacketing compared to the glass fibers, the outer pressure do not scatters away to the jacket, which makes the sensor more sensitive[12]. POF-OTDR may be suitable in structure monitoring of a human or animal body, or a deformable liquid container (such as silicone gel embedded at breast enlarging implant for women), which conflicts with the brittle intrinsic of the glass fibers. As a drawback in terms of sensitivity, in the case of using a large diameter POF, it makes the Fresnel reflection and Rayleigh scattering less observable because the stress is averaged out through the fiber volume. When using a thin POF such as 50 or 120 μm core PF-GIPOF of Chromis Fiberoptics, may the sensor provide higher sensitivity than the typical glass-based.

A stress monitoring method that uses the distance change between two POFs in series has been developed for detecting elongation, i.e., pressure in the waveguiding direction[50]. In the same way as the OTDR, the sensor mechanism itself was already existing with the usage of glass fibers[62]. POF was used at the purpose to enhance the old fatigue and damage detection system with glass

---

[12] Bare SMF are used in some sensors, but that means the sensor is highly fragile, which isn't good indeed:(

optical fibers which require expensive equipments (fiber-splicing kit) and expertise for installation that limit their widespread application. Since the sensor mechanism is intensity-based, it is claimed that it is simpler (thus inexpensive) than other pressure sensing systems such as Fabry-Perot or FBG, which is agreeable that the POF could further enhance such strength of the design. The transducer exploits the variation of light transmitted between two facing POFs with their axial distance. They have used 1000 μm SIPOF with NA=0.5 that provides a superior light collecting capability compared to a standard MMF. Perale *et. al.* uses a parallel series of this two-POF sensing set to monitor a large structure. The challenging factor of this sensor type is the temperature affection that the POF has, which is far serious compared to the glass-based fibers.

1.6.4 Summary

Types and characteristics of the known POF sensors are summarized in Table 1.3. POF extrinsic sensors are developed to enhance light coupling efficiency of those old models of glass fibers. Using the reactivity of plastic, POF chemical sensors have been originally developed. POF chemical sensors that uses the full strength of POF in medical use (safe from being stabbed) are also being reported. A POF OTDR has been developed to enhance the cost performance that the glass models had as a problem.

Table 1.3: Summarizing the essential points of the existing POF sensors.

Category	**Why POF?**	**Design originality**	**examples**
Extrinsic	Light coupling	copy from glass	Two-POF (Politecnico di Torino)
Chemical	chemical reactivity high moisture absorption	POF original	Moisture/gas sensor (U of Yamanashi, U of Manchester)
Biomedical	stab-safety (less brittle)	POF original	Moisture/gas sensor (U of Yamanashi)
Pressure	cheap	copy from glass	OTDR (BAM) Two-POF (Politecnico di Torino)

1.7 Proposal of a pressure sensor based on multimode PMF

In this dissertation, a pressure sensor using the P(MMA/BzMA)POF is proposed. The proposed sensor is an interferometric type that uses a polarized DC light and is an intrinsic sensor. Difference between the old types of FO pressure sensors are as described below.

First, by examining Table 1.2, the advantage of interferometric sensors (Mach-Zehnder and Fabry-Perot) are the high sensitivity with relatively low affection of fluctuation of light source and detector. In addition, Fabry-Perot type is showing capability for structure monitoring by using pulse modulation. The proposing sensor is also an interferometric type that all the above benefits are also expected.

As a draw back of the conventional interferometric sensors, they tend to have complex structure or high temperature affection that need to be treated adequately. In addition, those structures of known interferometric pressure sensors are considered to be fragile and sensitive that may be easily broken. Both Mach-Zehnder and Fabry-Perot types require more than one fiber for working and reference paths (Figures 1.4, 1.6). The another uniqueness of the proposing sensor is that it replaces these paths by ordinary and extraordinary modes that exist within one fiber. Thus, the proposing sensor requires only one fiber.

The structure is similar to the sensor using photoelastic crystal (Figure 1.2), but the function of crystal is replaced with the fiber itself. This design is possible only with the P(MMA/BzMA)POF, because of the relationship of two different types of birefringence that may exhibit in plastic (detail discussed in next chapter). Therefore, the proposing sensor is an interferometric sensor with the simplest design ever reported. From the aspect of intrinsic sensor, plastics are more elastic (opposite of brittle) than the glass [13] ; thus, employment of POF may result in enhancement of the sensor sensitivity.

The attempt to alternate glass MMF with POF has been showing a successful enhancement of the light coupling simplicity of extrinsic sensors (Table 1.3), whereas the POF OTDR may also have the this strength in comparison to the glass OTDRs. The proposing sensor also has this benefit of

---

[13] [Young's modules] PMMA: 2.3, glass: 50-90 (10^9 N/m^2,GPa)

light coupling and robustness, in addition to the capability in biomedical application.

The another novelty of this work is that the sensing principle is based on the birefringence change in multimode POF. To the best of author's knowledge, reports regarding birefringence in multimode POF is so far not existing. Although topics regarding POF FBGs that may care of birefringence are being reported[63, 64, 65], they all uses SM-POFs in which the properties are somewhat predictable (principles are same as the glass-based). The main interest in FBG researchers who use different material is the processing of the gratings, in which polymers are interesting because of the variety in processing method such as UV solidification using lithography techniques and so on.

In order to achieve such pressure sensor that has both benefits of interferometry and POF, a preliminary model was built using the P(MMA/BzMA)POF. Details of the fabrication procedure and tests on polarimetric sensitivity/dynamic range are described in Chapter 6.

1.8 Conclusions

This chapter summarized the motivation of the research. Known designs of PMF and FO pressure sensor that are developed in glass-based fibers were explained. Recent development of POF sensors and their characteristics were described. Based on these background information, uniqueness of P(MMA/BzMA) based PMF and the pressure sensor based on this fiber was explained.

Following is the overview of this dissertation. Chapter 2 explains the conceptual theories that the work had been based on, namely, about concepts of fiber modes, polarimetry, and birefringence generation model in polymers. Chapter 3 explains all the techniques used for measurements and sample preparations. Chapter 4 explains the basic fiber optic properties of the P(MMA/BzMA)POF in comparison to some other MMFs. Chapter 5 discusses the modal dependence of the polarization-maintaining property of the P(MMA/BzMA)POF. Chapter 6 discusses the phase retarding phenomenon induced by fiber macrobending. Chapter 7 discusses about the pressure sensor fabrication using the P(MMA/BzMA)POF. Chapter 8 concludes the essentials of the dissertation.

Chapter 2

CONCEPTUAL THEORIES

2.1 Preface

The first part of this section explains the waveguiding mechanism and the concept of mode of the optical fibers in which helps the reader to understand this dissertation. Waveguiding principle regarding polarization state and birefringence of optical fiber is explained as well. In the latter half, the way how the birefringence exhibits in general plastic material is explained.

2.2 Geometrical-optics of optical fibers

Waveguide in general can be classified into two groups, namely, such that have rectangular cross section and the ones that have circular cross section. The basic structure that those two have in common is that they are both structured with a core[1] surrounded by cladding[2]. Ray propagation in such structure can be understood straightforwardly by geometrical optics, in particular, the total reflection.

The geometrical-optics description[66], although approximate, is valid when the core radius a is much larger than the light wavelength λ. When two become comparable, it is necessary to use the wave-propagation theory of Section 2.3. In its simplest form an optical fiber consists of a cylindrical core surrounded by a cladding whose refractive index is lower than that of the core. Because of an abrupt index change at the core-cladding interface, such fibers are called step-index (SI) fibers. In a different type of fiber, known as graded-index (GI) fiber, the refractive index decreases gradually inside the core.

---

[1] Core: higher refractive index region

[2] Cladding: lower refractive index region

2.2.1 Step-index fibers[34]

Consider the geometry of Figure 2.1(a), where a ray making an angle θ_i with the fiber axis is incident at the core center. Because of refraction at the fiber-air interface, the ray bends toward the normal. The angle θ_r of the refracted ray is given by

$$n_0 \sin\theta_i = n_1 \sin\theta_r, \tag{2.1}$$

where n_1 and n_0 are the refractive indices of the fiber core and air, respectively. The refracted ray hits the core-cladding interface and is refracted again. However, refraction is possible only for an angle of incidence ϕ such that $\sin\phi < n_2/n_1$. For angles larger than a critical angle ϕ_c, defined by

$$\sin\phi_c = n_2/n_1, \tag{2.2}$$

where n_2 is the cladding index, the ray experiences total internal reflection at the core-cladding interface. Since such reflections occur throughout the fiber length, all rays with $\phi > \phi_c$ remain confined to the fiber core. This the basic mechanism behind light confinement in optical fibers.

One can use Eqs. (2.1, 2.2) to find the maximum angle that the incident ray should make with the fiber axis to remain confined inside the core. Noting that $\theta_r = \pi/2 - \phi_c$ for such a ray and substituting it in Eq. (2.1), we obtain

$$n_0 \sin\theta_i = n_1 \cos\phi_c = (n_1^2 - n_2^2)^{1/2}. \tag{2.3}$$

In analogy with lenses, $n_0 \sin\theta_i$ is known as the numerical aperture (NA) of the fiber. It represents the light-gathering capacity of an optical fiber. For $n_1 \simeq n_2$ the NA can be approximated by

$$\mathrm{NA} = n_1(2\Delta)^{1/2}, \qquad \Delta = (n_1 - n_2)/n_1, \tag{2.4}$$

where Δ is the normalized fractional index change at the core-cladding interface. Clearly, Δ should be made as large as possible in order to couple maximum light into the fiber.

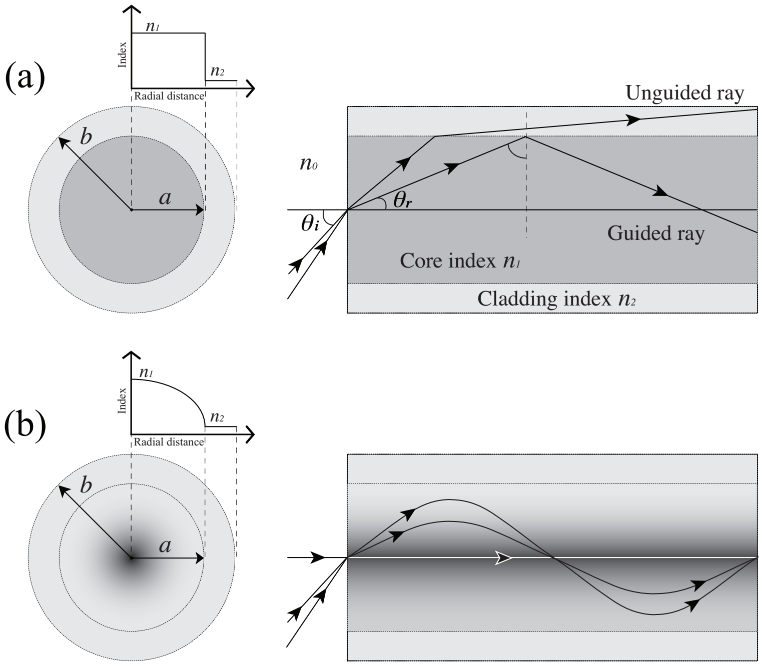

Figure 2.1: Ray trajectories in (a) SI and (b) GI fibers.

2.2.2 *Graded-index fibers[34]*

The refractive index of the core in GI fibers is not constant but decreases gradually from its maximum value n_1 at the core center to its minimum value n_2 at the core-cladding interface. Most GI fibers are designed to have a nearly quadratic decrease and are analyzed by using g-profile, in which the refractive index n as a function of radial position r is expressed by,

$$n(r) = \begin{cases} n_1[1 - \Delta(r/a)^g]; & r < a \\ n_1(1 - \Delta) = n_2; & r \geq a \end{cases} \tag{2.5}$$

where a is the core radius. The parameter g determines the index profile. A SI profile is approached in the limit of large g. A parabolic-index fiber corresponds to $g = 2$.

Figure 2.1 (b) shows schematic paths for three different rays. Similar to the case of SI fibers, the path is longer for more oblique rays. However, the ray velocity changes along the path because of variations in the refractive index. More specifically, the ray propagating along the fiber axis takes the shortest path but travels most slowly as the index is largest along this path. Oblique rays have a largest part of their path in a medium of lower refractive index, where they travel faster. It is therefore possible for all rays to arrive together at the fiber output by a suitable choice of the refractive-index profile.

2.2.3 Concept of mode[67]

As mentioned in the preceding section, in a primitive SI structure, light propagates by the sequence of total reflection. When core diameter is large enough compared to the wavelength of the light, any incident beam satisfying $\phi > \phi_c$ is permitted for propagation. However, when the core diameter becomes small as to be comparable with the wavelength, because of the effect of light interference, some discrete angle only be permitted for propagation. This is the idea of ”mode”.

Concept of mode is explained in a slab waveguide in a geometrical-optics point of view. Considering a TE waves[3] propagating along the waveguide (thickness: $2d$, refractive indices of core and cladding: n_1 and n_2) as shown in Figure 2.2. The black and red rays both have same wavefront as drawn in broken lines in the figure. The black ray reflects at point A and arrives B while the red ray leaves point C and arrives D as both rays are treated as the same plane wave. Hence, the change in phase while black ray propagates AB needs to be in the relation of $\times 2\pi m$ (m is an integer) to the phase change of the red ray propagating CD.

Such relation in phase is said to be satisfying the equation below.

$$kn_1 l_2 + 2\Phi - kn_1 l_1 = 2m\pi \tag{2.6}$$

l_1 and l_2 are distances between AB and CD, respectively. k is wave number ($2\pi/\lambda$). Φ is Goos-Hanchen shift[4]. Those are expressed as,

---

[3] TE: Transverse electric; this case, the oscillating direction of the electric-wave is perpendicular to this page

[4] Goos-Hanchen shift: phase shift generated at the total reflection of a TE mode

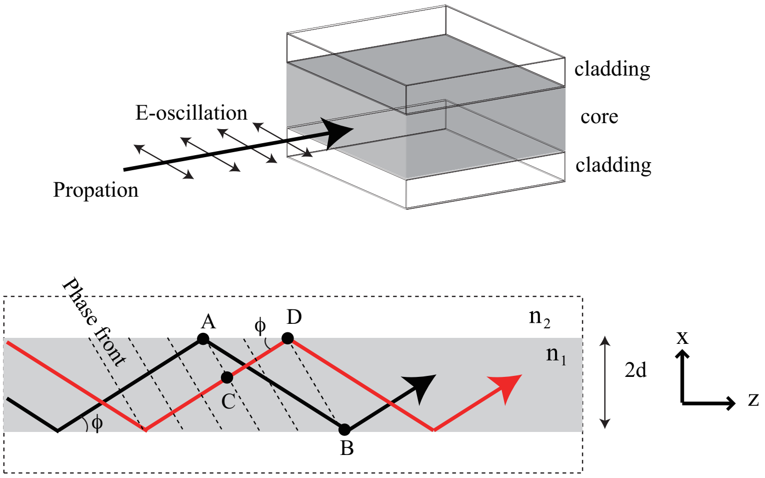

Figure 2.2: Explanation of mode in geometrical-optics point of view.

$$\Phi = -2\tan^{-1}\sqrt{\frac{2\Delta}{\sin^2\phi} - 1} \tag{2.7}$$

$$l_1 = 2d\left(\frac{1}{sin\phi} - 2\sin\phi\right) \tag{2.8}$$

$$l_2 = \frac{2d}{\sin\phi}, \tag{2.9}$$

and by substituting them in Eq. (2.6),

$$4kn_1 d\sin\phi + 2\Phi = 2m\pi \tag{2.10}$$

$$\tan\left(kn_1 d\sin\phi - \frac{m\phi}{2}\right) = \sqrt{\frac{2\Delta}{\sin^2\phi} - 1} \tag{2.11}$$

is obtained. By Eq. (2.4), one particular value of ϕ that corresponds to m can be obtained if the dimensional structure and wavelength are given, i.e., inputs with particular angles can only be propagated. Such devision of lightwave that satisfies the phase conditions are called mode (transverse[5]).

---

[5] Transverse mode: need to be distinguished with longitudinal mode that is often used in the area of lasers

Propagation constants that corresponds to z-axis and x-axis are expressed using the ϕ as follows.

$$\beta = kn_1 \cos\phi \tag{2.12}$$

$$\chi = kn_1 \sin\phi \tag{2.13}$$

The fundamental mode refers to mode that satisfies Eq. (2.4) with minimum angle (corresponds to $m = 0$). Higher order modes refers to modes satisfying Eq. (2.4) with condition of $m \geq 1$.

2.3 Wave-propagation theory of optical fibers

2.3.1 Maxwell's Equations in optical fiber geometry[34]

Like all electromagnetic (EM) phenomena, propagation of optical fields in fibers is governed by Maxwell's equations. For a nonconducting medium without free charges, these equations take the form[68]

$$\nabla \times \mathbf{E} = \partial \mathbf{B}/\partial t, \tag{2.14}$$

$$\nabla \times \mathbf{H} = \partial \mathbf{D}/\partial t, \tag{2.15}$$

$$\nabla \cdot \mathbf{D} = 0, \tag{2.16}$$

$$\nabla \cdot \mathbf{B} = 0, \tag{2.17}$$

where **E** and **H** are the electric and magnetic field vectors, respectively, and **D** and **B** are the corresponding flux densities. The flux densities are related to the field vectors by the constitutive relations[68]

$$\mathbf{D} = \epsilon_0 \mathbf{E} + \mathbf{P}, \tag{2.18}$$

$$\mathbf{B} = \mu_0 \mathbf{H} + \mathbf{M}, \tag{2.19}$$

where ϵ_0 is the vacuum permittivity, μ_0 is the vacuum permeability, and **P** and **M** are the induced electric and magnetic polarizations, respectively. For both glass-based and plastic-based optical fibers, $\mathbf{M} = 0$ because of the nonmagnetic nature of these materials.

Evaluation of the electric polarization **P** requires a microscopic quantum-mechanical approach, but nonlinear effects in optical fiber is ignored in this discussion of fiber modes. **P** is then related to **E** by the relation

$$\mathbf{P} = \epsilon_0 \int_{-\infty}^{\infty} \chi(\mathbf{r}, t - t')\mathbf{E}(\mathbf{r}, t')dt'. \tag{2.20}$$

Linear susceptibility χ is a second-rank tensor, but we reduces to a scalar for instance by assuming an isotropic medium such as silica glass. Optical fibers become slightly birefringent because of unintentional variations in the core shape or in local strain; such birefringent effects are considered in Section 2.4.1. Equation (2.20) assumes a spatially local response.

Equations (2.14)-(2.20) provide a general formalism for studying wave propagation in optical fibers. In practice it is convenient to use a single field variable **E**. By taking the curl of Eq. (2.14) and using Eqs. (2.15),(2.18), and (2.19), we obtain the wave equation

$$\nabla \times \nabla \times \mathbf{E} = -\frac{1}{c^2}\frac{\partial^2 \mathbf{E}}{\partial t^2} - \mu_0 \frac{\partial^2 \mathbf{P}}{\partial t^2} \tag{2.21}$$

where the speed of light in vacuum is defined as usual by $c = (\mu_0 \epsilon_0)^{-1/2}$. By introducing the Fourier transform of $\mathbf{E}(\mathbf{r}, t)$ through the relation

$$\tilde{\mathbf{E}}(\mathbf{r}, \omega) = \int_{-\infty}^{\infty} \mathrm{E}(\mathbf{r}, t)\exp(i\omega t)dt, \tag{2.22}$$

as well as a similar relation for $\mathrm{P}(\mathbf{r}, t)$, and by using Eq. (2.20), Eq. (2.21) can be written in the frequency domain as

$$\nabla \times \nabla \times \tilde{\mathbf{E}} = -\epsilon(\mathbf{r}, \omega)(\omega^2/c^2)\tilde{\mathbf{E}}, \tag{2.23}$$

where the frequency-dependent dielectric constant is defined as

$$\epsilon(\mathbf{r},\omega) = 1 + \tilde{\chi}(\mathbf{r},\omega), \tag{2.24}$$

and $\tilde{\chi}(\mathbf{r},\omega)$ is the Fourier transform of $\chi(\mathbf{r},t)$. In general, $\epsilon(\mathbf{r},t)$ is complex. Its real and imaginary parts are related to the refractive index n and the absorption coefficient α by the definition

$$\epsilon = (n + i\alpha c/2\omega)^2. \tag{2.25}$$

By using Eqs. (2.23) and (2.25), n and α are related to $\tilde{\chi}$ as

$$n = (1 + \mathrm{Re}\tilde{\chi})^{1/2}, \tag{2.26}$$

$$\alpha = (\omega/nc)\mathrm{Im}\tilde{\chi}, \tag{2.27}$$

where Re and Im stand for the real and imaginary parts, respectively. Both n and α are frequency dependent.

Two further simplifications can be made before solving Eq. (2.23). First, ϵ can be taken to be real and replaced by n^2 because of low optical losses in silica fibers. Second, since $n(\mathbf{r},\omega)$ is independent of the spatial coordinate $\mathbf{r}$ in both the core and the cladding of a SI fiber, one can use the identity

$$\nabla \times \nabla \times \tilde{\mathbf{E}} \equiv \nabla(\nabla \cdot \tilde{\mathbf{E}}) - \nabla^2\tilde{\mathbf{E}} = -\nabla^2\tilde{\mathbf{E}}, \tag{2.28}$$

where we used Eq. (2.16) and the relation $\tilde{\mathbf{D}} = \epsilon\tilde{\mathbf{E}}$ to set $\nabla \cdot \tilde{\mathbf{E}} = 0$. This simplification is made even for GI fibers. Equation (2.28) then holds approximately as long as the index changes occur over a length scale much longer than the wavelength. By using Eq. (2.28) in Eq. (2.23), we obtain

$$\nabla^2\tilde{\mathbf{E}} + n^2(\omega)k_0^2\tilde{\mathbf{E}} = 0, \tag{2.29}$$

where the free-space wave number k_0 is defined as

$$k_0 = \omega/c = 2\pi/\lambda, \tag{2.30}$$

and λ is the vacuum wavelength of the optical field oscillating at the frequency ω. Equation (2.29) is solved next to obtain the optical modes of SI fibers.

2.3.2 Fiber modes[34]

The concept of the mode is a general concept in optics occurring also, for example in the theory of lasers. An optical mode refers to a specific solution of the wave equation Eq. (2.29) that satisfies the appropriate boundary conditions and has the property that its spatial distribution does not change with propagation. The fiber modes can be classified as guided modes, leaky modes, and radiation modes[69]. As one might expect, signal transmission in fiber-optic communication systems takes place through the guided modes only. The following discussion focuses exclusively on the guided modes of a SI fiber.

To take advantage of the cylindrical symmetry, Eq. (2.29) is written in the cylindrical coordinates ρ, ϕ, z as

$$\frac{\partial^2 E_z}{\partial \rho^2} + \frac{1}{\rho}\frac{\partial E_z}{\partial \rho^2} + \frac{1}{\rho}\frac{\partial^2 E_z}{\partial \phi^2} + \frac{\partial^2 E_z}{\partial z^2} + n^2 k_0^2 E_z = 0, \tag{2.31}$$

where for a SI fiber of core radius a, the refractive index n is of the form

$$n = \begin{cases} n_1; & \rho \leq a \\ n_2; & \rho > a \end{cases} \tag{2.32}$$

For simplicity of notation, the tilde over $\tilde{\mathbf{E}}$ has been dropped and the frequency dependence of all variables is implicitly understood. Equation (2.31) is written for the axial component E_z of the E(electric)-field vector. Similar equations can be written for the over five components of $\mathbf{E}$ and $\mathbf{H}$. However, it is not necessary to solve all six equations since only two components out of six are independent. It is customary to choose E_z and H_z as the independent components and obtain $E_\rho, E_\phi, H_\rho, H_\phi$ in terms of them. Equation (2.31) is easily solved by using the method of separation of variables and writing E_z as

$$E_z(\rho, \phi, z) = F(\rho)\Phi(\phi)Z(z). \tag{2.33}$$

By using Eq. (2.33) in Eq (2.31), we obtain the three ordinary differential equation:

$$\frac{d^2Z}{dz^2} + \beta^2 Z = 0, \tag{2.34}$$

$$\frac{d^2\Phi}{d\phi^2} + m^2\Phi = 0, \tag{2.35}$$

$$\frac{d^2F}{d\rho^2} + \frac{1}{\rho}\frac{dF}{d\rho} + (n^2k_0^2 - \beta^2 - \frac{m^2}{\rho^2})F = 0. \tag{2.36}$$

$$\tag{2.37}$$

Equation (2.34) has a solution of the form $Z = \exp(i\beta z)$, where β has the physical significance of the propagation constant. Similarly, Eq. (2.35) has a solution $\Phi = \exp(im\phi)$, but the constant m is restricted to take only integer values since the field must be periodic in ϕ with a period of 2π.

Equation (2.36) is the well-known differential equation satisfied by the Bessel functions[70]. Its general solution in the core and cladding regions can be written as

$$F(\rho) = \begin{cases} AJ_m(p\rho) + A'Y_m(p\rho); & \rho \le a \\ CK_m(q\rho) + C'I_m(q\rho); & \rho > a \end{cases} \tag{2.38}$$

where A, A', C and C' are constants and J_m, Y_m, K_m and I_m are different kinds of Bessel functions[70]. The parameters p and q are defined by

$$p^2 = n_1^2k_0^2 - \beta^2, \tag{2.39}$$

$$q^2 = \beta^2 - n_2^2k_0^2. \tag{2.40}$$

Considerable simplification occurs when we use the boundary condition that the optical field for a guided mode should be finite at $\rho = 0$ and decay to zero at $\rho = \infty$. Since $Y_m(p\rho)$ has a singularity at $\rho = 0$, $F(0)$ can remain finite only if $A' = 0$. Similarly $F(\rho)$ vanishes at infinity only if $C' = 0$. The general solution of Eq. (2.31) is thus of the form

$$E(z) = \begin{cases} AJ_m(p\rho)\exp(im\phi)\exp(i\beta z); & \rho \leq a, \\ CK_m(q\rho)\exp(im\phi)\exp(i\beta z); & \rho > a. \end{cases} \tag{2.41}$$

The same method can be used to obtain H_z which also satisfies Eq. (2.31). Indeed, the solution is the same but with different constants B and D, that is,

$$H(z) = \begin{cases} BJ_m(p\rho)\exp(im\phi)\exp(i\beta z); & \rho \leq a, \\ DK_m(q\rho)\exp(im\phi)\exp(i\beta z); & \rho > a. \end{cases} \tag{2.42}$$

The other four components E_ρ, E_ϕ, H_ρ and H_ϕ can be expressed in terms of E_z and H_z by using Maxwell's equations. In the core region, we obtain

$$E_\rho = \frac{i}{p^2}(\beta\frac{\partial E_z}{\partial\rho} + \mu_0\frac{\omega}{\rho}\frac{\partial H_z}{\partial\phi}), \tag{2.43}$$

$$E_\phi = \frac{i}{p^2}(\frac{\beta}{\rho}\frac{\partial E_z}{\partial\phi} - \mu_0\omega\frac{\partial H_z}{\partial\rho}), \tag{2.44}$$

$$H_\rho = \frac{i}{p^2}(\beta\frac{\partial H_z}{\partial\rho} - \epsilon_0 n^2\frac{\omega}{\rho}\frac{\partial E_z}{\partial\phi}), \tag{2.45}$$

$$H_\phi = \frac{i}{p^2}(\frac{\beta}{\phi}\frac{\partial H_z}{\partial\phi} + \epsilon_0 n^2\omega\frac{\partial E_z}{\partial\phi}). \tag{2.46}$$

These equations can be used in the cladding region after replacing p^2 by $-q^2$.

Equations (2.41) to (2.46) express the EM field in the core and cladding regions of an optical fiber in terms of four constants A, B, C and D. These constants are determined by applying the boundary condition that the tangential components of $\tilde{\mathbf{E}}$ and $\tilde{\mathbf{H}}$ be continuous across the core-cladding interface. By requiring the continuity of E_z, H_z, E_ϕ, and H_ϕ at $\rho = a$, we obtain a set of four homogeneous equations satisfied by A, B, C, and D[71]. These equations have a nontrivial solution only if the determinant of the coefficient matrix vanishes. After considerable algebraic details, this condition leads us to the following eigenvalue equation [71, 72, 73]:

$$[\frac{J'_m(pa)}{pJ_m(pa)} + \frac{K'_m(qa)}{qK_m(qa)}][\frac{J'_m(pa)}{pJ_m(pa)} + \frac{n_2^2}{n_1^2}\frac{K'_m(qa)}{qK_m(qa)}] \tag{2.47}$$

$$= \frac{m^2}{a^2}(\frac{1}{p^2} + \frac{1}{q^2})(\frac{1}{p^2} + \frac{n_2^2}{n_1^2}\frac{1}{q^2}), \tag{2.48}$$

where a prime indicates differentiation with respect to the argument.

For a given set of the parameters K_0, a, n_1 and n_2, the eigenvalues equation (2.48) can be solved numerically to determine the propagation constant β. In general, it may have multiple solutions for each integer value of m. It is customary to enumerate these solutions in descending numerical order and denote them by β_{mn} for a given m ($n = 1, 2, ...$). Each value β_{mn} corresponds to one possible mode of propagation of the optical field whose spatial distribution is obtained from Eqs. (2.41)-(2.46). Since the field distribution does not change with propagation except for a phase factor and satisfies all boundary conditions, it is an optical mode of the fiber. In general, both E_z and H_z are nonzero (except for $m = 0$), in contrast with the planer waveguides, for which one of them are denoted by HE_{mn} or EH_{mn}, depending on whether H_z or E_z dominates. In the special case $m = 0$, HE_{0n} or EH_{0n} are also denoted by TE_{0n} or TM_{0n}[6], respectively, since they correspond to transverse-electric ($E_z = 0$) and transverse-magnetic ($H_z = 0$) modes of propagation.

A mode is uniquely determined by its propagation constant β. It is useful to introduce a quantity $\overline{n} = \beta/k_0$, called the mode index or effective index and having the physical significance that each fiber mode propagates with an effective refractive index $\overline{n}$ whose value lies in the range $n_1 > \overline{n} > n_2$. This can be understood by noting that the optical field of guided modes decays exponentially inside the cladding layer since[70]

$$K_m(q\rho) = (\pi/2q\rho)^{1/2}\exp(-q\rho) \qquad \text{for} \qquad q\rho \gg 1. \tag{2.49}$$

---

[6] TE: transverse electric, TM: transverse magnetic

When $\overline{n} \leq n_2, q^2 \leq 0$ from Eq. (2.40), $p = k_0(n_1^2 - n_2^2)^{1/2}$ when $q = 0$. A parameter that plays an important role in determining the cuttof condition is defined as

$$V = k_0 a(n_1^2 - n_2^2)^{1/2} \approx (2\pi/\lambda) a n_1 \sqrt{2\Delta}. \tag{2.50}$$

It is called the normalized frequency ($V \propto \omega$) or simply the V parameter. It is also useful to introduce a normalized propagation constant b as

$$b = \frac{\beta/k_0 - n_2}{n_1 - n_2} = \frac{\overline{n} - n_2}{n_1 - n_2}. \tag{2.51}$$

A fiber with a large value of V supports many modes. Below a certain value of V, all modes except the HE$_{11}$ modes reach cutoff. Such fibers support a single mode and are called SMFs.

2.3.3 *Weakly guiding approximation[34, 67, 74]*

Before moving on to the discussion of SMF, species of mode and mode degeneration need to be explained. Using Eq. (2.48), TE and TM modes can be written as

$$\frac{J_m'(pa)}{pJ_m(pa)} + \frac{K_m'(qa)}{qK_m(qa)} = 0 \quad \text{:TE mode} \tag{2.52}$$

$$\frac{J_m'(pa)}{pJ_m(pa)} + \frac{n_2^2}{n_1^2}\frac{K_m'(qa)}{qK_m(qa)} = 0 \quad \text{:TM mode} \tag{2.53}$$

On the other hand, at the condition of,

$$\triangle = \frac{n_1^2 - n_2^2}{2n_1^2} \approx \frac{n_1 - n_2}{n_1} \ll 1, \tag{2.54}$$

$\beta \simeq k_0 n_1$ works. With this approximation, Eq. (2.48) can be rewritten as below.

$$\frac{J_m'(pa)}{pJ_m(pa)} + \frac{K_m'(qa)}{qK_m(qa)} \tag{2.55}$$

$$= \frac{m}{a}\left(\frac{1}{p^2} + \frac{1}{q^2}\right). \tag{2.56}$$

Then, TE and TM modes in Eq. (2.53) become identical. In addition, plus (corresponds to EH) and minus (corresponds to HE) of Eq. (2.56) can be rewritten as below.

$$-\frac{J_1'(pa)}{pJ_0(pa)} = \frac{K_1'(qa)}{qK_0(qa)} \quad \text{:TE,TM modes} \tag{2.57}$$

$$-\frac{J_{n+1}'(pa)}{pJ_n(pa)} = \frac{K_{n+1}'(qa)}{qK_n(qa)} \quad \text{:EH mode} \tag{2.58}$$

$$\frac{paJ_{n-2}'(pa)}{pJ_{n-1}(pa)} = \frac{qaK_{n-2}'(qa)}{qK_{n-1}(qa)} \quad \text{:HE mode} \tag{2.59}$$

By replacing the notation in the way below,

$$m = \begin{cases} 1; & \text{(for TM and TE modes)} \\ n+1; & \text{(for EH modes)} \\ n-1; & \text{(for HE modes),} \end{cases} \tag{2.60}$$

an overall expression can be obtained as below.

$$\frac{paJ_{m-1}'(pa)}{pJ_m(pa)} = \frac{qaK_{m-1}'(qa)}{K_m(qa)} \quad \text{:HE mode} \tag{2.61}$$

Therefore, TM, HE, EH modes can be mutually degenerated. This mode group after degeneration is called LP (Linearly polarized) modes[75].

Examples of degenerated mode groups are listed in Table 2.1. Some examples of the distribution of E-field of each modes are shown in Figure 2.3. Figure 2.4 shows the relationship of the strict classification of modes and the degenerated LP modes.

Table 2.1: Degenerated modes

LP mode	original mode	degeneration
LP_{01}	$HE_{11} \times 2$	$\times 2$
LP_{11}	TE_{01}, TM_{01}, $HE_{21} \times 2$	$\times 4$
LP_{21}	$EH_{11} \times 2$, $HE_{31} \times 2$	$\times 4$
LP_{02}	$HE_{12} \times 2$	$\times 2$
LP_{13}	TE_{03}, TM_{03}, $HE_{23} \times 2$	$\times 4$

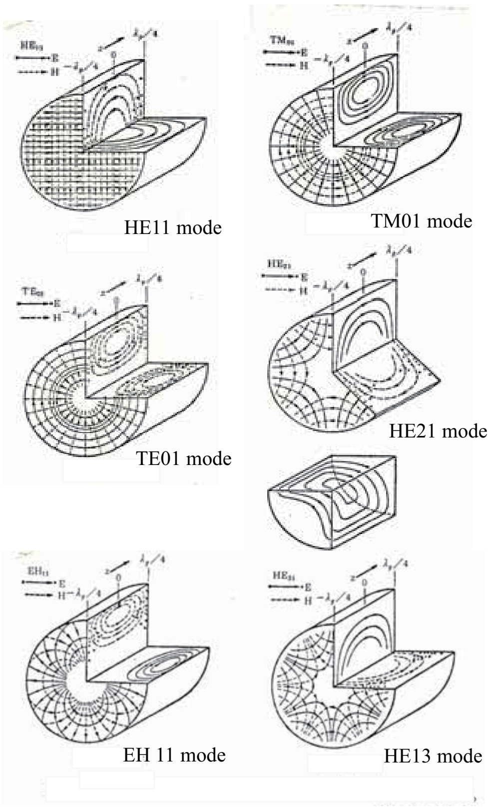

Figure 2.3: E-field distribution of mode[74]

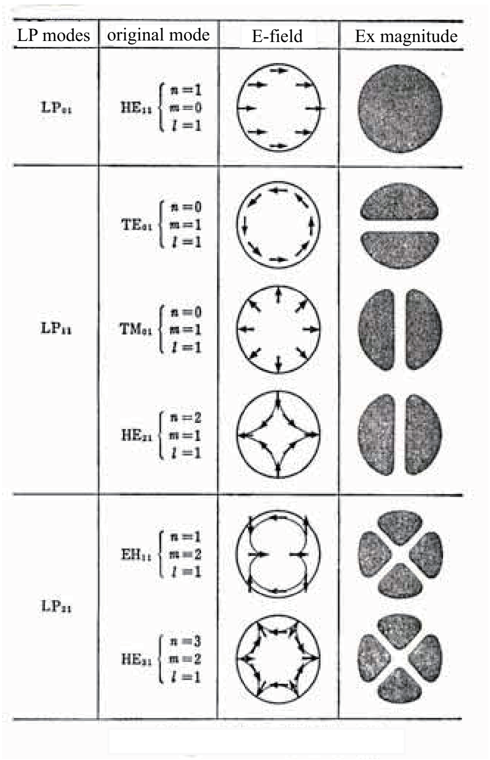

Figure 2.4: Categories of mode fields[74]

2.3.4 Singlemode condition[34]

The singlemode condition is determined by the value of V at which the TE_{01} and TM_{01} modes reach cutoff. The eigenvalues equations for these two modes can be obtained by setting $m = 0$ in Eq. (2.48) and are given by

$$pJ_0(pa)K_0'(qa) + qJ_0'(pa)K_0(qa) = 0, \tag{2.62}$$

$$pn_2^2J_0(pa)K_0'(qa) + qn_2^2J_0'(pa)K_0(qa) = 0. \tag{2.63}$$

A mode reaches cutoff when $q = 0$. Since $pa = V$ when $q = 0$, the cutoff condition for both modes is simply given by $J_0(V) = 0$. The smallest value of V for which $J_0 = 0$ is 2.405. A fiber designed such that $V < 2.405$ supports only the fundamental HE_{11} mode. This is the singlemode condition.

We can use Eq. (2.50) to estimate the core radius of SMFs used in lightwave systems. For the operating wavelength range 1.3-1.6 μm, the fiber is generally designed to become singlemode for $\lambda > 1.2\ \mu m$. By taking $\lambda = 1.2\ \mu m$, $n_1 = 1.45$, and $\Delta = 5 \times 10^{-3}$, Eq. (2.50) shows that $V < 2.405$ for a core radius $a < 3 \times 10^{-3}$. Indeed, most telecommunication fibers are designed with $a \approx 4\mu m$.

The mode index $\bar{n}$ at the operating wavelength can be obtained by using Eq. (2.51), according to which

$$\bar{n} = n_2 + b(n_1 = n_2) \approx n_2(1 + b\Delta) \tag{2.64}$$

as a function of V for the HE_{11} mode. An analytic approximation for b [76] is,

$$b(V) \approx (1.1428 - 0.9960/V)^2 \tag{2.65}$$

and is accurate to within 0.2% for V in the range 1.5-2.5.

The field distribution of the fundamental mode is obtained by using Eqs. (2.41)-(2.48). The axial components of E_z and H_z are quite small for $\Delta \ll 1$. Hence, the HE_{11} mode is approximately linearly polarized for weakly guiding fibers. Hence, it is also denoted as LP_{01}, following an alternative terminology in which all fiber modes are assumed to be linearly polarized[75]. One of the transverse components can be taken as zero for a LP mode. If we set $E_y = 0$, the E_x component of the E-field for the HE_{11} mode is given by

$$E(x) = E_0 \begin{cases} (J_0(p\rho)/J_0(pa))\exp(i\beta z); & \rho \leq a, \\ (K_0(q\rho)/K_0(qa))\exp(i\beta z); & \rho > a \end{cases} \tag{2.66}$$

where E_0 is a constant related to the power carried by the mode [76]. The dominant component of the corresponding magnetic field is given by $H_y = n_2(\epsilon_0/\mu_0)^{1/2}E_x$. This mode is linearly polarized along the x axis. The same fiber supports another mode linearly polarized along the y axis. In this sense a SMF actually supports two orthogonally polarized modes that are degenerate and have the same mode index.

2.4 Stress-induced polarization-maintaining fiber

2.4.1 Fiber birefringence[34]

The degenerate nature of the orthogonally polarized modes holds only for an ideal SMF with a perfectly cylindrical core of uniform diameter. Real fibers exhibit considerable variation in the shape of their core along the fiber length. They may also experience nonuniform stress such that the cylindrical symmetry of the fiber is broken. Degeneracy between the orthogonally polarized fiber modes is removed because of these factors, and the fiber acquires birefringence. The degree of modal birefringence is defined by

$$B_m = |\overline{n}_x - \overline{n}_y|, \tag{2.67}$$

where $\overline{n}_x$ and $\overline{n}_y$ are the modes indices for the orthogonally polarized fiber modes.

2.4.2 Beat length[34]

Birefringence leads to a periodic power exchange between the two polarization components. The period, referred to as the beat length, is given by

$$L_B = \lambda / B_m. \tag{2.68}$$

Typically, $B_m \sim 10^{-7}$, and $L_B \sim 10m$ for $\lambda \sim 1\mu m$. From a physical viewpoint, linear polarized light remains linearly polarized only when it is polarized along one of the principal axes. Otherwise, its state of polarization changes along the fiber length from linear to elliptical, and then back to linear, in a periodic manner over the length L_B. Figure 2.5 shows schematically such a periodic change in the state of polarization for a fiber of constant birefringence B. The fast axis in this figure corresponds to the axis along which the mode index is smaller. The other axis is called the slow axis.

2.4.3 Polarization-mode dispersion[34]

In conventional SMF, birefringence is not constant along the fiber but changes randomly, both in magnitude and direction, because of variations in the core shape (elliptical rather than circular) and the anisotropic stress acting on the core. As a result, light launched into the fiber with linear polarization quickly reaches a state of arbitrary polarization. Moreover, different frequency components of a pulse acquire different polarization states, resulting in pulse broadening. This phenomenon is called polarization-mode dispersion and becomes a limiting factor for optical communication systems operating at high bit rates. It is possible to make fibers for which random fluctuations in the core shape and size are not the governing factor in determining the state of polarization. Such fibers are called polarization-maintaining fibers (PMFs)[7]. A large amount of birefringence is introduced intentionally in these fibers through design modifications so that small random birefringence fluctuations do not affect the light polarization significantly. Typically, $B_m \sim 10^{-4}$ for such fibers.

---

[7] PMF here refers to those of typical glass-based SMF. It has to be noted that a different definition needs to be applied for the PMF of MMF.

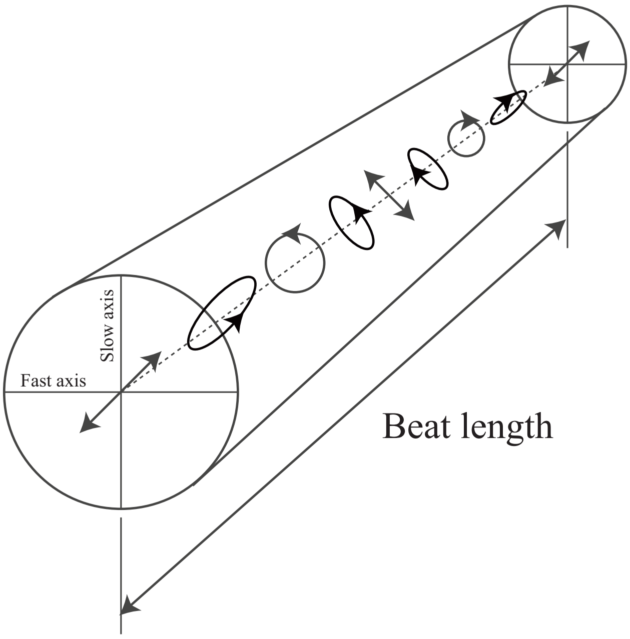

Figure 2.5: State of polarization in a birefringent fiber over one beat length[34]. Input beam is linearly polarized at 45° with respect to the slow and fast axes.

2.5 Low birefringence spun polarization-maintaining fiber[29, 30, 31]

Low birefringence spun PMF is produced by spinning fiber preform during drawing. That way, all preform non-uniformities are spread out around all directions. As a result, all polarization errors (retardations) accumulated by the propagating signal cancel each other out. The spun PMF is different from the stress-induced PMFs because of the following reasons. Highly birefringent fibers, such as Panda or Bow-tie maintain only linear polarization, while low birefringence spun fiber maintains both linear and circular polarization states. Also, because of the spun fiber's uniformity, there is no need to align the fiber when coupling light in our out. It is also convenient for the fiber splicing, because proper fiber orientation is not critical to polarimetric accuracy when using low birefringent fiber.

The high local (internal) birefringence is created in spun fiber by applying internal stress to the cladding or employing elliptical core. This high birefringence negates other pressure or bend-induced polarization effects, but since its axis is rotated uniformly it introduces virtually no error into output signal. The difference between spun fiber and twisted fiber is that the spun fiber preform is rotated during drawing, so the fiber cools down without residual torsional stress. Twisting the fiber after drawing results in similar polarization-maintaining qualities, and both types of fiber can be used to produce fiber optic components, such as chiral fiber polarizers.

2.6 Beam propagation in nonrestrictive space[77]

A model for expressing light propagation in homogeneous medium without a core-cladding restriction is explained here. Lightwave in such condition is often expressed with planer or spherical wave, but such case is not realistic for highly coherent lightwave such as the output from laser diodes (LD). Such lightwaves that transmit along a particular axis is called beams.

Imaginary part of the E-field of an axis-symmetrical beam is expressed using cylindrical coordinate system (r, ψ, z).

$$\mathbf{E} = \mathbf{E_c} U(r,z) \exp(jwt - jkz) \tag{2.69}$$

Equation of $U(r,z)$ is obtained by substituting the above in Eq. (2.23).

$$\frac{1}{r}\frac{d}{dr} r \frac{d}{dr} U(r,z) - 2jk\frac{d}{dz} U(r,z) = 0, \tag{2.70}$$

$$\text{where} \qquad |d^2U/k^2dz^2| << |dU/kdz| \tag{2.71}$$

To solve this using separation of variables, imaginary terms are expressed in $p(z)$ and $q(z)$.

$$U(r,z) = \exp\left(-j[p(z) + \frac{kr^2}{2q(z)}]\right) \tag{2.72}$$

By substituting this in Eq. (2.70), equations of $p(z)$ and $q(z)$ are obtained.

$$\frac{dp(z)}{dz} + \frac{j}{q(z)} = 0, \tag{2.73}$$

$$\frac{dq(z)}{dz} - 1 = 0 \tag{2.74}$$

Solutions of the above is,

$$p(z) = -j \ln 1 + \frac{z}{q_0} + p_0 \tag{2.75}$$

$$q(z) = z + q_0 \tag{2.76}$$

Solutions of Eq. (2.70) is expressed by four equations shown below by having $p_0 = 0$ and $q_0 = j\pi\omega_0^2/\lambda$ substituted in Eq. (2.72).

$$U(r,z) = (\frac{\omega_0}{\omega}) \exp(-(\frac{r}{\omega})^2) \exp(j\phi) \exp(-j(\frac{k}{2R})r^2) \tag{2.77}$$

$$\omega(z) = \omega_0 \sqrt{1 + (\frac{\lambda_z}{\pi\omega_0^2})^2} \tag{2.78}$$

$$R(z) = z(1 + (\frac{\pi\omega_0^2}{\lambda_z})^2) \tag{2.79}$$

$$\phi(z) = \tan^{-1}(\frac{\lambda_z}{\pi\omega_0^2}) \tag{2.80}$$

The lightwave corresponding to the first solution (Eq. (2.77)) is called Gaussian beam. The power distribution of z-cross section is described by Gaussian functions, such as $\exp[-2(r/\omega)^2]$. The beam diameter is defined by $2\omega(z)$, which is the region that has intensity higher than $1/e^2$ of the center.

As shown in Figure 2.6, the beam takes the minimum diameter[8] of $2\omega_0$ at $z = 0$. After this point the beam diameter expands with angle of,

$$2\theta = 2\tan^{-1}(\frac{\lambda}{\pi\omega_0}) \sim \frac{2\lambda}{\pi\omega_0}. \tag{2.81}$$

---

[8] called the beam waist

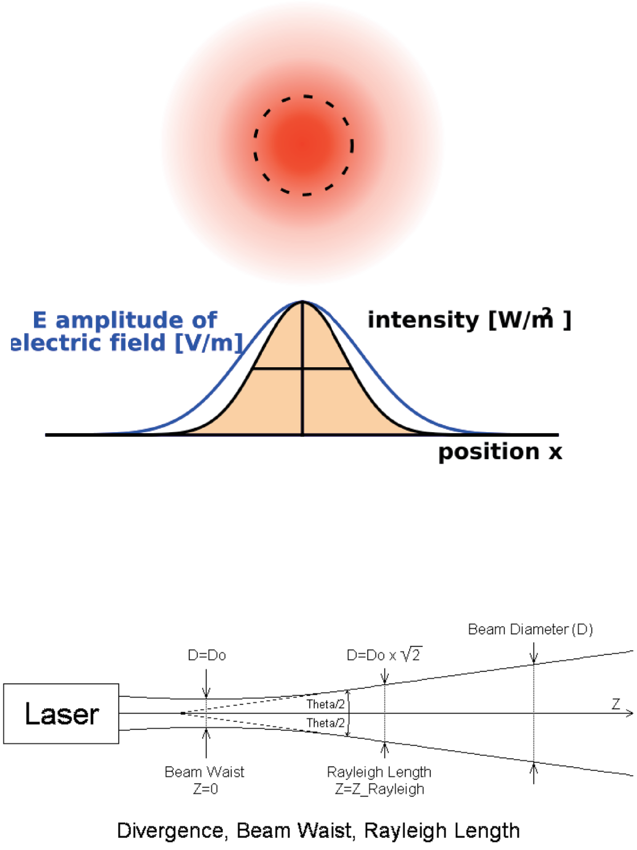

Figure 2.6: Gaussian beam[78, 79]

It is noted that the ω_0/ω term in Eq. (2.77) is expressing the conservation of power regardless to the change in beam diameter. In addition, $\exp(-j(k/2R)r^2)$ is expressing a bend of wavefront, whereas such bend is expressed by curvature radius of $R(z)$. The wavefront is therefore planar at the beam waist $(z = 0)$, $R(0) = \infty$. It starts to bend after this point, where at the farther point $(R(z) \sim z)$, the wavefront start to picture a spherical wave with the point of origin at the beam waist. Such change in beam diameter and wavefront surface is a matter of diffraction, which never occurs in a waveguide-style propagation.

2.7 Polarization-maintaining model of a low-birefringence large-core MMF

Based on the theoretical background regarding fiber modes in the earlier sections, hypotheses of physical model of polarization-maintaining phenomenon in a low-birefringence large-core[9] (LBLC) MMF that is investigated in this dissertation is discussed here.

Effect of low birefringence

The difference in physical meaning of LP mode degeneracy breakage between SMF and MMF needs to be clarified. In SMF, disturbance of polarization state refers to the mode coupling between HE_{11}^{x} and HE_{11}^{y} modes. This occurs only when there is a structural irregularity that breaks the LP_{01} mode (identical to HE_{11}) degeneracy. At the same time, the fiber is said to have an optical axis. The breakage of degeneracy is said to be rarely occurring in a low birefringence medium, because of the absence of optical axis.

Effect of large core

Mode coupling in a MMF typically refers to interactions between HE, EH, TM, and TE modes, instead of indicating the breakage of degeneracy. In addition, an irregularity in a same magnitude affects a large core MMF in a less significant manner than the case of SMF, because of the difference in total volume. Hence, it may be harder to induce an optical axis with an outer irregularity in a similar magnitude. Still, however, it is natural to consider some chances of LP breakage in a MMF. Even in such case, the tremendous amount of modes that a 500 μm core MMF supports would always have some mode level that the beam could couple into without changing the original polarization state. When a linear polarization was coupled to a LBLC MMF, dominant portion of the energy propagates along the HE_{11} mode. Here, a structural irregularity cannot split the whole HE_{11} components to two orthogonal modes unless the irregularity is so large and consistent throughout the core that the whole core exhibits an optical axis. Hence, dominant portion arrives the other end without suffering a huge trouble. In the case of large-core MMF with certain amount of birefringence, the breakage of LP_{11} degeneracy could be avoided to some extent in the volume aspect (same as the low birefringence case described above), however, the intrinsic birefringence causes

---

[9] Large core here refers to over 500 μm in diameter.

the breakage of LP_{11} in a significant manner. It therefore cannot maintain the initial polarization state.

Effect of multimode

The way in which the linear polarization state is maintained in the LBLC MMF is explained by the HE_{11} mode. The hypothesis of how a circularly polarized beam propagates the LBLC MMF is as follows. The beam propagates among numbers of modes that spatially matches the polarization state. Thus, it never stays in a single hybrid mode. Because the fiber supports huge variation of modes, modes that correspond to any particular components pretty much exist.

2.8 Birefringence in chain polymers

Conceptual explanation of birefringence in chain polymers was done based on empirical evidences in former studies[80]. Because it is squashed into a chain-like geometry, molecule groups exists in a random orientation in a chain polymer. Thus, no matter what anisotropy do the mer (periodic molecular unit in a polymer) got, a polymer primarily do not exhibit birefringence. Two different causes that make a polymer birefringent, namely, orientational birefringence and photoelastic birefringence are explained in this section.

2.8.1 Optical anisotropy[66, 81, 82]

An important characteristic of materials (crystals, ceramics, polymers, and their composites) is that many of their properties depend on the ”direction,” that is materials are generally anisotropic. The dielectric constant, ϵ_r depends on electronic polarization which involves the displacement of electrons with respect to positive atomic nuclei. Electronic polarization depends on the crystal direction inasmuch as it is easier to displace electrons along certain directions. This means that the refractive index n of a material depends on the direction of the E-field in the propagating light beam. Consequently, the velocity of light in a crystal depends on the direction of propagation and on the state of its polarization, i.e., the direction of the E-field. Most noncrystalline materials such as polymers, glasses or liquids, and all cubic crystals are optically isotropic, that is the refractive index is the same in all directions. For all classes of materials excluding the above (such as non-cubic crystals and

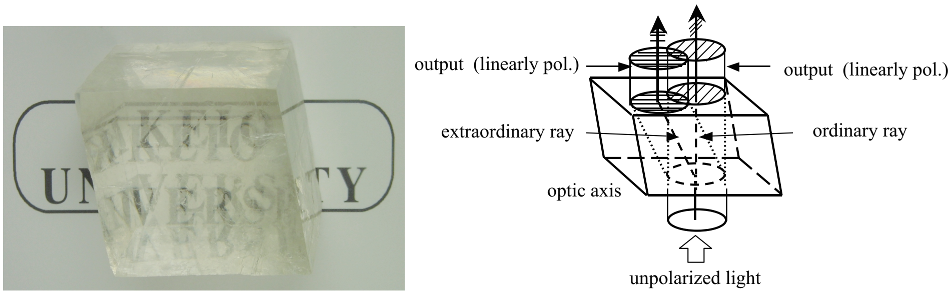

Figure 2.7: Word print viewed through a calcite crystal.[83]

draw-processed polymers/glasses), the refractive index depends on the propagation direction and the state of polarization. The result of optical anisotropy is that, except along certain special directions, any unpolarized light ray entering such a crystal breaks into two different rays with different polarizations and phase velocities. When we view and image through a calcite crystal just incase, and optically anisotropic, we see two images, each constituted by light of different polarization passing through the crystal as depicted in Figure 2.7. Optically anisotropic materials are called birefringent because an incident light beam may be doubly refracted.

Experiments and theories on ”most anisotropic crystals”, *i.e.* those with the highest degree of anisotropy, show that we can describe light propagation in terms of three refractive indices, called principal refractive indices, n_1, n_2 and n_3, along three mutually orthogonal directions in the crystal, say x_1, x_2 and x_3 called principal axes. These indices correspond to the polarization state of the wave along these axes.

Crystals that have three distinct principal indices also have two optic axes and are called biaxial crystals. On the other hand, uniaxial crystals have two of their principal indices the same ($n_1 = n_2$) and only have one optic axis. Polymer birefringence occurring while it is deformed is treated in the same way as this uniaxial crystals.

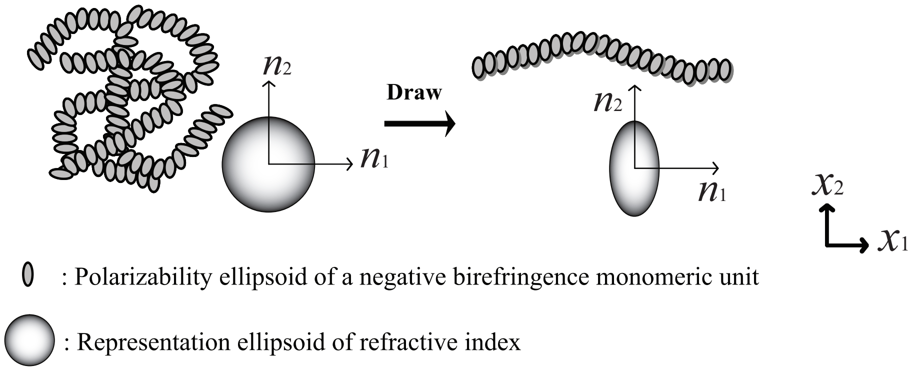

Figure 2.8: Schematic explanation of orientational birefringence in homopolymer made of negative birefringence monomeric units. Polymer chains are illustrated as the polarizability ellipsoids of monomeric units. The principal axes of the polarizability ellipsoid correspond to the polarizability in those directions. The representation ellipsoid of the polymer refractive index is the averaged property of each polarizability ellipsoid. The principal axes (n_1 and n_2) of the representation ellipsoid correspond to the refractive indices in those directions. The directionality of the negative polarizability ellipsoids is isotropically averaged by polymer chain packing, which exhibits no birefringence ($n_1 = n_2$). When drawn in x_1 direction, the polymer chain is oriented in the direction of the polarizability ellipsoids, which induces negative birefringence ($n_1 < n_2$).

2.8.2 Orientational birefringence[84, 83, 85]

Orientational birefringence is caused by the polymer chain orientation while being extruded at a temperature above its glass transition temperature. The principle of the orientational birefringence is as explained in Figure 2.8.

We first define the directional representation of how the electrons in the monomeric molecule vibrates, as in which we call the polarizability ellipsoid (Figure 2.9).

In the geometry of the polarizability ellipsoid, the principle axes have a strong relation to the polymer chain orientation, because of our common sense that we can assume that the bonding direction is statistically in the right-angle relationship to any side chains attached to the functional carbon. A polymer exhibits no birefringence when its chains are randomly oriented even if each monomer unit has an anisotropic polarizability. This is because small-scale anisotropies do not predominate in one particular direction; thus, the macroscopic refractive index remains isotropic.

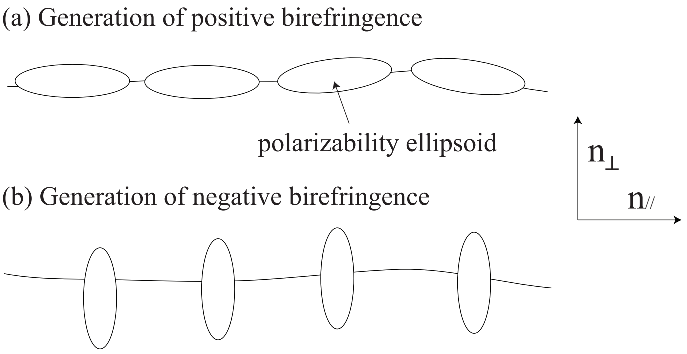

Figure 2.9: Schematic representation of (a) positive and (b) negative birefringent polymer and the definition of vertical and horizontal refractive indices. $n_{//}$ - $n_\perp$ respectively are the refractive indices at the cases when the polarized light enters the substance in the angle matched to the axis parallel and perpendicular to the polymer chain orientation.

However, the polymer becomes birefringent when its chains are oriented, because the anisotropies no longer cancel each other out. Using the notation in Figure 2.9, the orientational birefringence is defined as:

$$\Delta n \text{ (orientational)} = n_{//} - n_\perp, \tag{2.82}$$

where the sign of the orientational birefringence is defined as

$$\Delta n \text{ (orientational)} \begin{cases} > 0 \quad \text{(positive);} & n_{//} > n_\perp \\ < 0 \quad \text{(negative);} & n_{//} < n_\perp. \end{cases} \tag{2.83}$$

In addition to the dependency of orientational birefringence to the monomer species, the magnitude of the observable birefringence is linearly dependent to the chain orientation, as in detail,

Table 2.2: Classification of polymers in orientational birefringence signs[85, 83].

Positive	Negative
Poly(benzyl methacrylate) (PBzMA)	Poly(methyl methacrylate) (PMMA)
Poly(phenylene oxide) PPO	Polystyrene (PSt)
Polycarbonate (PC)	Polysulfone (PS)
Poly(vinyl chloride) (PVC)	Poly(methyl acrylate) (PMA)

$$\Delta n \text{ (orientational)} = f \cdot \Delta n^0, \tag{2.84}$$

$$\Delta n^0 = \frac{2\pi}{9} \cdot \frac{\overline{n}^2 + 2)^2}{\overline{n}} \cdot \frac{\rho}{M} \cdot N_A \Delta\alpha \tag{2.85}$$

$$\Delta\alpha = \alpha_x - \frac{\alpha_y + \alpha_z}{2}, \tag{2.86}$$

$$\tag{2.87}$$

where each notations represent, Δn^0: intrinsic birefringence, $\overline{n}$: average refractive index for all directions, ρ: density of the substance, N_A: Avogadro number, M: molecular weight at unit volume, and α: average polarizability for all direction. Δn^0 is the value when f is 1, meaning the potential birefringence value when the chains are perfectly oriented. In the case expressed in Eq. (2.87), the polymer is assumed to be oriented into the x-direction. Such case of having $f = 1$ is known to be very difficult to be demonstrated in the experiment. Although the value Δn^0 may give us a good estimation of the material's birefringence property, too many factors such as polymeric conformation, tacticity, rotation of the functioning group, or the stablest structure at the drawn state, need to be taken into account when deciding the $\Delta\alpha$. Therefore, experimental approach is more focused and considered to be practical in the former development in this field[83].

The signs of the orientational birefringence adopted from Dr. Iwata's doctoral dissertation[85] is shown in Table 2.2. The sign of each molecule is known to be highly related to the structure[84], but this dissertation may not go too deep in this point. The sign plays an important role when designing the copolymer system for a birefringence-control purpose. The monomers involved in this study is also listed in the table.

2.8.3 Photoelastic birefringence[83, 85, 86]

Photoelastic birefringence is caused either by the outer stress applied while the polymer is solidified at a temperature below glass transition temperature, or by a nonuniform shrinkage while being quenched. Molecule groups that consists the polymer chain tilts in a similar direction by the structural distortion induced by the stress. This tilt appears as a macroscopic matching of mer-scale polarizability, which as a result causes birefringence. When the deformation is caused by an outer stress, the plastic is no longer birefringent when the stress is removed. Figure 2.10 describes this phenomena visually.

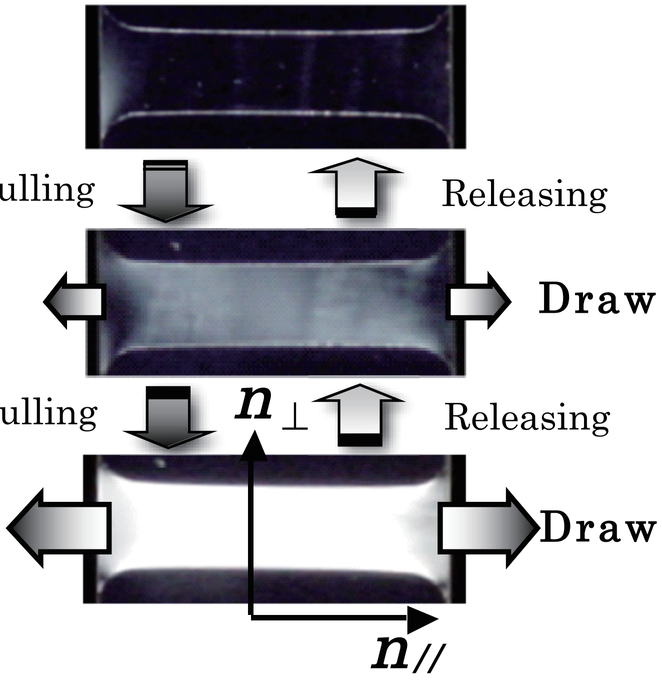

Figure 2.10: Photoelastically birefringent film sandwiched in a crossed Nicol.[83]

Table 2.3: Classification of polymers in photoelastic coefficient signs[85].

Positive	Negative
BzMA (Benzyl methacrylate)*	MMA (Methyl methacrylate)*
CHMA (Cyclohexyl methacrylate)	α-MSt (α-Methyl styrene)
PhMA (Phenyl methacrylate)	
St (Styrene)	

Birefringence in such case is expressed as:

$$\Delta n \text{ (photoelastic)} = c \cdot \Delta\sigma, \tag{2.88}$$

$$\Delta\sigma = \sigma_1 - \sigma_2, \tag{2.89}$$

where $\sigma_1, \sigma_2, \Delta\sigma$ and c are principal stresses ($\sigma_1 > \sigma_2$), principal stress difference, and photoelastic coefficient. We define the sign of the principal stress as plus for expansion and minus for compression. c is dependent to each polymer specie, whereas polymers of $c < 0$ and $c > 0$ are defined to have negative and positive photoelastic birefringence, respectively.

Table 2.3 shows the sign of the photoelastic coefficients ”c” of different polymers. It is noted by comparing some polymers listed also in Table 2.2 that there seem to be no correlation between the signs of the two types of birefringence. Therefore, the recent study is suggesting that the generation mechanism of the orientational and photoelastic birefringence are quite independent.

2.9 Birefringence reduction using copolymerization[84, 85, 86]

Copolymerization of methyl methacrylate (MMA) and benzyl methacrylate (BzMA) was formerly reported from our group as an effective method for reducing the birefringence in a polymeric material[84]. The reduction of orientational birefringence by the copolymerization is described in Figure 2.11. By copolymerizing two monomers that each has mutually opposite polarizability-

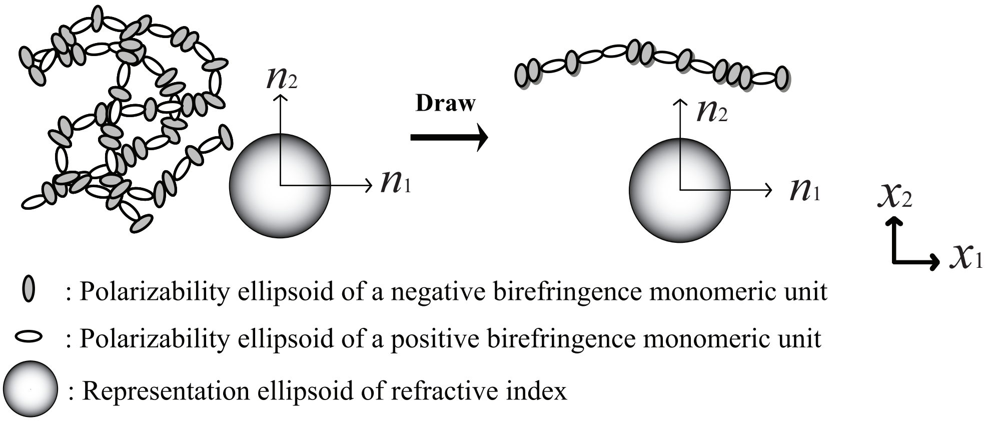

Figure 2.11: Schematic explanation of reduction of orientational birefringence using copolymer made of negative and positive birefringence monomeric units. Polymer chains are illustrated as the polarizability ellipsoids of monomeric units. No birefringence is exhibited even after drawing, because positive and negative polarizability ellipsoids mutually compensate their anisotropy ($n_1 = n_2$).

ellipsoid, refractive index isotropy is maintained regardless of the polymer chain orientation. Reduced birefringence in such copolymer was previously demonstrated in films of 40 to 70 μm thickness[35]. Plastic optical fiber (POF) in which its core fabricated using poly-(MMA/BzMA) (P(MMA/BzMA)) copolymer is presented here to explore how the polarization-maintaining property of the birefringence-reduced copolymer exhibits in meter order waveguiding.

2.10 Polarimetry

This section explains the phase optics of polarizer, birefringent medium(s), and analyzer system. Although Stokes parameter is the most typical way for describing the polarization state, experimental analysis that are done in this research is so simple in which do not require such matrix notation. A basic polarimetry based on Malus's law is therefore used for phase analysis throughout the dissertation.

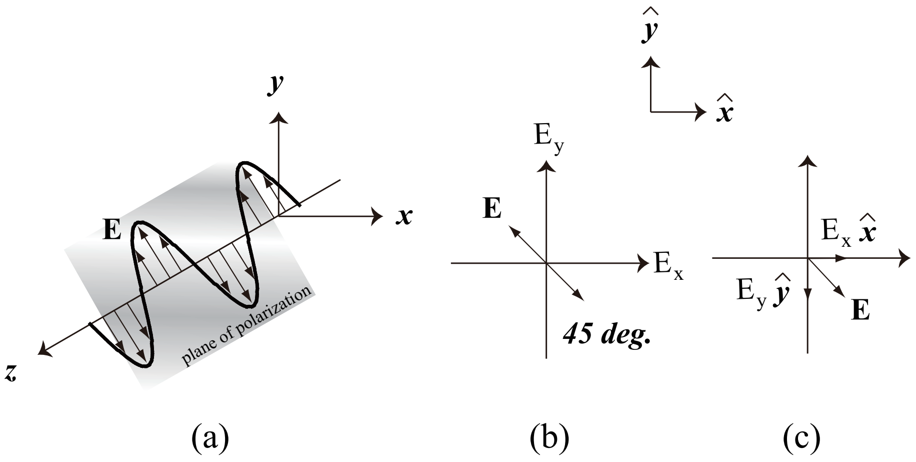

Figure 2.12: (a) A linearly polarized wave having its E-field oscillations defined along a line perpendicular to the direction of propagation *z*. The field vector **E** and *z* defined a plane of polarization. (b) The E-field oscillations in the plane of polarization. (c) A linearly polarized light at any instant being represented by the superposition of the two fields E_x and E_y with the right magnitude and phase.

2.10.1 State of polarization[81]

A propagating EM wave has its electric and magnetic field at right angles to the direction of propagation. If we place a *z*-axis along the direction of propagation, then the E-field can be in any direction in the plane perpendicular to the *z*-axis. The term polarization of an EM wave describes the behavior of the E-field vector in the EM wave as it propagates through a medium. If the oscillations of the E-field at all times are contained within a well-defined line then the EM wave is said to be linearly polarized (Figure 2.12(a)). The field vibrations and the direction of propagation (*z*) defined a planed of polarization so that linear polarization implies a wave that is plane-polarized. By contrast, if a beam of light has waves with the E-field in each in a random direction but perpendicular to *z*, then this light beam is unpolarized A light beam can be linearly polarized by passing the beam through a polarizer, a device that only passes E-field oscillations lying on a well defined plane at right angles to the propagating direction.

Suppose that we arbitrarily place the *x* and *y* axes and describe the E-field in terms of its components E_x and E_y along x and y. To find the E-field in the wave at any space and time location, we add E_x and E_y vectorially. Both E_x and E_y can individually be described by a wave equation which must have the same angular frequency ω and wavenumber k. However, we must include a phase difference ϕ between the two below:

$$E_x = E_{x0}\cos(\omega t - kz), \tag{2.90}$$

$$E_y = E_{y0}\cos(\omega t - kz + \phi). \tag{2.91}$$

In Eq. 2.91, ϕ is the phase difference between E_x and E_y. ϕ can arise if one of the components is delayed, which is more familiar to be called as retardation in this dissertation.

The linearly polarized wave in Figure 2.12(a) has the **E** oscillations at -45° to x-axis as shown in (b). We can generate this field by choosing $E_{x0} = E_{y0}$ and $\phi = \pm\pi$ in Eq. (2.91). If $\hat{\mathbf{x}}$ and $\hat{\mathbf{y}}$ are the unit vectors along x and y, using $\phi - \pi$ in Eq. (2.91), the field in the wave is:

$$\mathbf{E} = \hat{\mathbf{x}}\mathbf{E_x} + \hat{\mathbf{y}}\mathbf{E_y} \tag{2.92}$$

$$= \hat{\mathbf{x}}E_{x0}\cos(\omega t - kz) - \hat{\mathbf{y}}E_{y0}\cos(\omega t - kz) \tag{2.93}$$

$$= \mathbf{E_0}\cos(\omega t - kz) \tag{2.94}$$

$$\text{where} \qquad \mathbf{E_0} = \hat{\mathbf{x}}E_{x0} - \hat{\mathbf{y}}E_{y0} \tag{2.95}$$

There could be many choices for the behavior of the E-field besides the simple linear polarization as in Figure 2.12. For example, if the magnitude of the field vector **E** remains constant but its tip at a given location on z traces out a circle by rotating in a clockwise sense with time as observed, then the wave is said to be right circularly polarized as shown in Figure 2.13. If the rotation of the tip of **E** is counterclockwise, the wave is said to be left circularly polarized. From Eq. (2.91), it should be apparent that a right circularly polarized wave has $E_{x0} = E_{y0} = A$ (amplitude), and $\phi = \pi/2$. This means that:

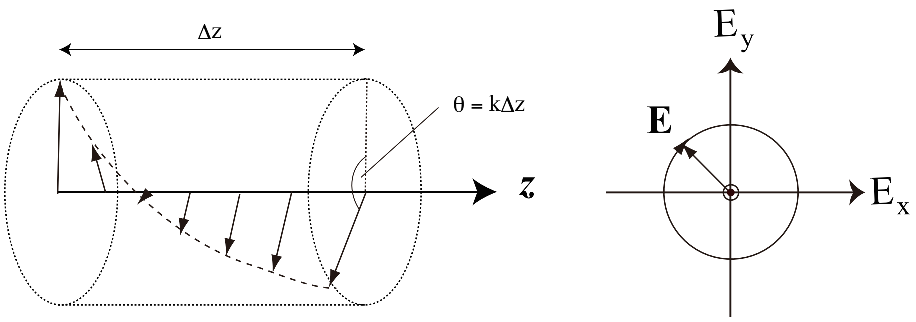

Figure 2.13: A right circularly polarized light. The field vector **E** is always at right angles to *z*, rotates clockwise around *z* with time, and traces out a full circle over one wavelength of distance propagated.

$$E_x = A\cos(\omega t - kz), \tag{2.96}$$

$$E_y = -A\sin(\omega t - kz + \phi), \tag{2.97}$$

where the circle shown in Figure 2.13 is expressed as $E_x^2 + E_y^2 = A^2$.

The snapshot of the circularly polarized light in Figure 2.13 shows that over a distance Δz, the field **E** rotates though an angle $\theta = k\Delta z$. Linear and circular polarization concepts are summarized in Figure 2.14 where for simplicity $E_{y0} = 1$ has been taken and the corresponding E_{x0} and ϕ are shown.

An elliptically polarized light has the tip of the **E**-vector trace out an ellipse as the wave propagates through a given location in space. As in circular polarization, light can be right and left elliptically polarized depending on clockwise or counterclockwise rotation of the **E**-vector. Figure 2.14 illustrates how an elliptically polarized light can result for any ϕ not zero or equal to any multiple of π, and when E_{x0} and E_{y0} are not equal in magnitude. Elliptic light can also be obtained when $E_{x0} = E_{y0}$ and the phase differences is $\pm\pi/4$ or $\pm 3\pi/4$ etc.

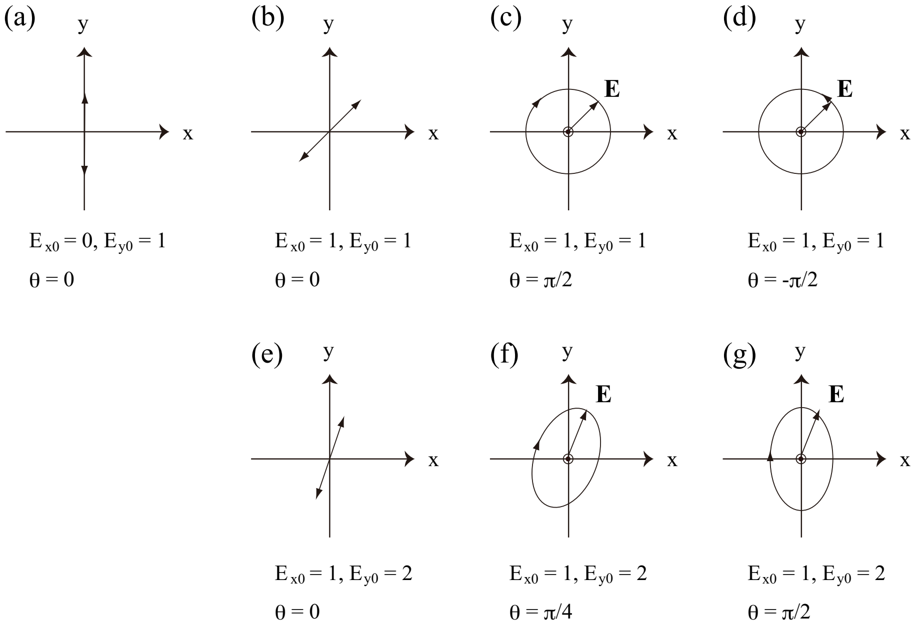

Figure 2.14: Types of polarization. (a), (b), (e): linear; (c): right circular; (d): left circular; (f): right elliptical with tilted major axis; and (g): right elliptical with straight major axis.

2.10.2 Malus's Law[66, 81]

There are various optical devices that operate on the polarization state of a wave passing through it and thereby modify the polarization state. A polarizer will only permit E-field component along one particular direction, called the transmission axis, to pass through the device as illustrated in Figure 2.15. The emerging beam from the polarizer (I_1) has its field oscillations along the transmission axis and hence it is linearly polarized.

Suppose that the linearly polarized light from the polarizer is now incident on a second identical polarizer (mediums 1 and 2 do not exist). Then by rotating the transmission axis of this second polarizer (TA2) we can analyze the polarization state of the incident beam; hence the second polarizer is called an analyzer. If the TA2 is at an angle θ to the E-field of the incident beam I_1 ($= I_2 = I_3$) then only the component $E\cos\theta$ of the field will be allowed to pass through the analyzer is proportional to the square of the E-field which means that the detected intensity varies as $(E\cos\theta)^2$. Since all the

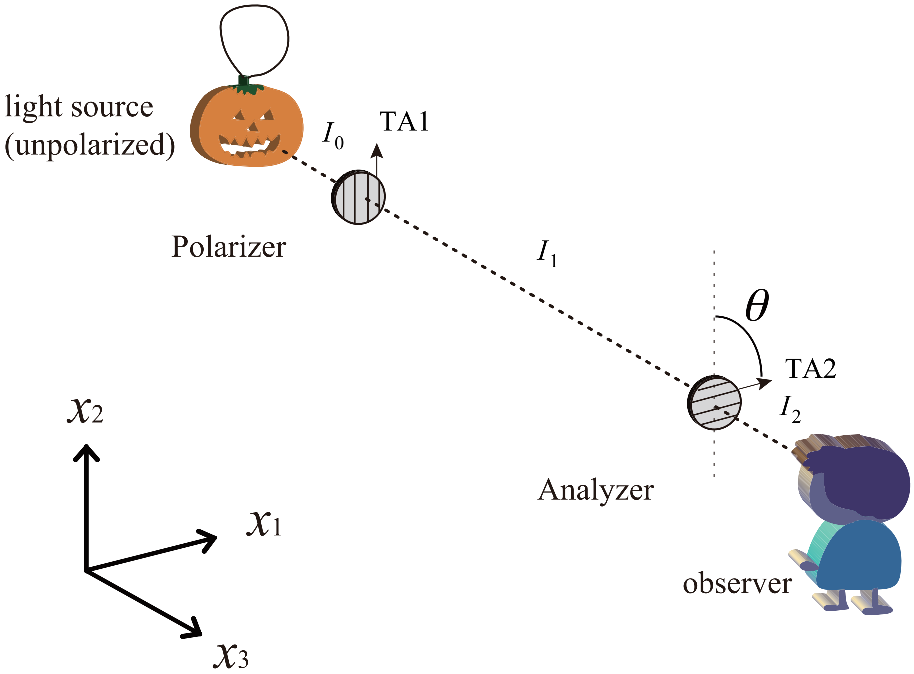

Figure 2.15: Randomly polarized light I_0 is incident on polarizer with a transmission axis TA1. Light emerging from polarizer is linearly polarized with **E** along TA1, and becomes incident on analyzer with a transmission axis TA2.

E-field will pass when $\theta = 0$, (**E** parallel to TA2), this is the maximum irradiance condition (parallel Nicol). The intensity of a beam, measured in Wm^2, is proportional to the square of the amplitude. Thus the intensity I_0 of the incident beam is proportional to A_0^2 and the intensity I of the transmitted beam is proportional to A_0^2 ($= (A_0 \cos\theta)^2$). The irradiance I at any other angle θ is then given by Malus's Law. Summarizing in equations,

$$A = A_0 \cos\theta \tag{2.98}$$

$$A^2 = (A_0 cos\theta)^2 \tag{2.99}$$

$$= A_0^2 \cos^2\theta \tag{2.100}$$

$$I(\theta) = I(0)\cos^2\theta. \tag{2.101}$$

Malus's law therefore relates the intensity of a linearly polarized light passing through a polarizer to the angle between the transmission axis and the E-field vector.

2.10.3 Light propagation in an uniaxial anisotropic medium[81, 66]

We may now consider the case when medium 1 is inserted between polarizer and analyzer in Figure 2.15. For our discussions of optical anisotropy, we will consider uniaxial materials such are drawn polymer and non-drawn polymer. All experiments and theories lead to the following basic principles.

Any EM wave entering an anisotropic crystal splits into two orthogonal linearly polarized waves which travel with different phase velocities, that is they experience different refractive indices. These two orthogonally polarized waves in uniaxial crystals are called ordinary (*o*) and extraordinary (*e*) waves. The *o*-wave has the same phase velocity in all directions and behaves like an ordinary wave in which the field is perpendicular to the phase propagation direction. These two waves propagate with the same velocity only along a special direction called the optical axis. The *o*-wave is always perpendicularly polarized to the optical axis and obeys the usual Snell's law.

The two images observed in Figure 2.7 are due to *o*-waves and *e*-waves being refracted differently so that when they emerge from the crystal they have been separated. Each ray constitutes an image but the field directions are orthogonal. If we were to view an object along the optical axis of the crystal, we would not see two images because the two rays would experience the same refractive index.

As mentioned above, we can represent the optical properties of a material in terms of three refractive indices along three orthogonal axes, the principal axes of the material, shown as x_1, x_2, and x_3 in Figure 2.16 (a). These are special axes along which the polarization vector and the E-field are parallel. In other way to express: the electric displacement $\mathbf{D}$ ($\mathbf{D} = \epsilon_0\mathbf{E} + \mathbf{P}$) and the $\mathbf{E}$ vectors are parallel. The refractive indices along these x_1, x_2, and x_3 axes are the principal indices n_1, n_2, and n_3 respectively for e-field oscillation along these directions. For example, for a wave with a polarization parallel to the x_1 axis, the refractive index is n_1.

The refractive index associated with a particular EM wave in a crystal can be determined by

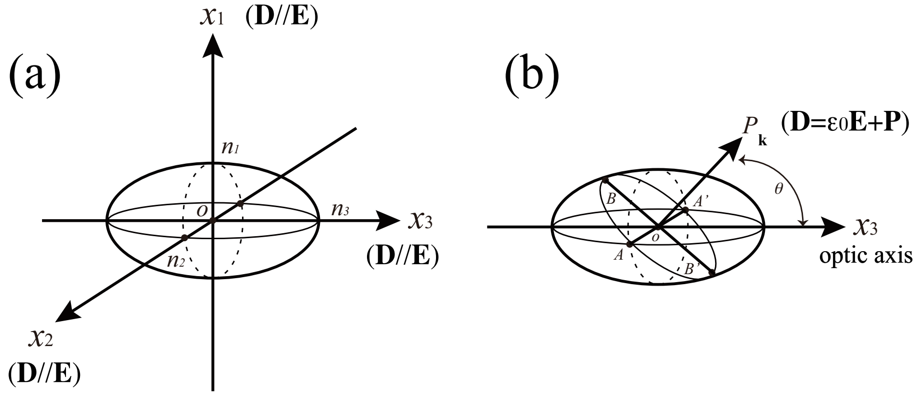

Figure 2.16: (a): Optical indicatrix (Fresnel's ellipsoid); (b): An EM wave propagating along *OP* at an angle θ to optical axis.

using Fresnel's refractive index ellipsoid, called the optical indicatrix, which is a refractive index surface placed in the center of the principal axes, as shown in Figure 2.16(a), where the x_1, x_2, and x_3 axis intercepts are n_1, n_2, and n_3. If all three indices were the same, $n_1 = n_2 = n_3 = n_0$ we would have a spherical surface and all e-field polarization directions would experience the same refractive index n_0. Such a spherical surface would represent an optically isotropic crystal. For positive uniaxial materials, $n_1 = n_2 < n_3$ which is the example in Figure 2.16(a).

Suppose that we wish to find the refractive indices experienced by a wave traveling with an arbitrary wave vector **k**, which represents the direction of phase propagation. This phase propagation direction is shown as *OP* in Figure 2.16(b) and is at an angle θ to the x_3-axis. We place a plane perpendicular to *OP* and passing through the center *O* of the indicatrix. This plane intersects the ellipsoid surface in a curve *ABA'B'* which is an ellipse. The major (*BOB'*) and minor (*AOA'*) axes of this ellipse determine the field oscillation directions and the refractive indices associated with the wave. Put differently, the original wave is now represented by two orthogonally polarized EM wave.

The line *AOA'*, the minor axis, corresponds to the polarization of the ordinary wave. Its semi-axis *OA'* is the refractive index $n_o = n_2$ of this *o*-wave. The electric displacement and the e-field are in the same direction and parallel to *AOA'*. If we were to change the direction of *OP* we would always find the same minor axis, i.e., n_0 is either n_1 or n_2 whatever the orientation of *OP*. This means that the *o*-wave always experiences the same refractive index in all directions.

The line *BOB'* in Figure 2.16(b), the major axis, corresponds to the electric displacement field (**D**) oscillations in the extraordinary wave and its semi-axis *OB'* is the refractive index $n_e(\theta)$ of this *e*-wave. This refractive index is smaller than n_3 but greater than n_2 (=n_o). The *e*-wave therefore travels more slowly than the *o*-wave in this particular direction and in this material. If we change the direction of *OP*, we find that the length of the major axis changes with the *OP* direction. Thus, $n_e(\theta)$ depends on the wave direction θ. As apparent, $n_e = n_o$ when *OP* is along the x_3-axis; when the wave is traveling along the optical axis have the same phase velocity whatever their polarization. When the *e*-wave is traveling along the x_1 (or x_2)-axis, $n_e(\theta) = n_3 = n_e$ and the *e*-wave has its slowest phase velocity as shown in Figure 2.16(b).

Along any *OP* direction that is at an angle θ to the optical axis, the *e*-wave has a refractive index $n_e(\theta)$ given by:

$$\frac{1}{n_e(\theta)^2} = \frac{\cos^2\theta}{n_o^2} + \frac{\sin^2\theta}{n_e^2}. \tag{2.102}$$

Clearly, for $\theta = 0, n_e(0) = n_o$ and for $\theta = 1/\pi, n_e(1/\pi) = n_e$.

The major axis *BOB* in Figure 2.16(b) determines the *e*-wave polarization by defining the direction of the displacement vector **D** and not **E**. Although **D** is perpendicular to **k**, this is not true for **E**. The e-field of the *e*-wave is orthogonal to that of the *o*-wave, and it is in the plane determined by **k** and the optical axis, as discussed below. **E** is orthogonal to **k** when the *e*-wave propagates along one of the principal axes.

Figure 2.17 illustrates the cross sections of the indicatrix at various propagation directions. In the cases of different beam angles expressed in θ, ϕ, and φ referring to the optical axis x_3, the case creating a 2-dimensional ellipse with the highest aspect ratio, $n_o = a, n_e = b$, creates the maximum retardation between the *o*- and the *e*-waves, because of their velocity difference. Clearly, the cases (b) and (c) are identical for out case treating an uniaxial material.

We now consider a case with such uniaxial material rested between the polarizer-analyzer system with its optical axis perpendicular to the beam path as illustrated in Figure 2.18. As mentioned in

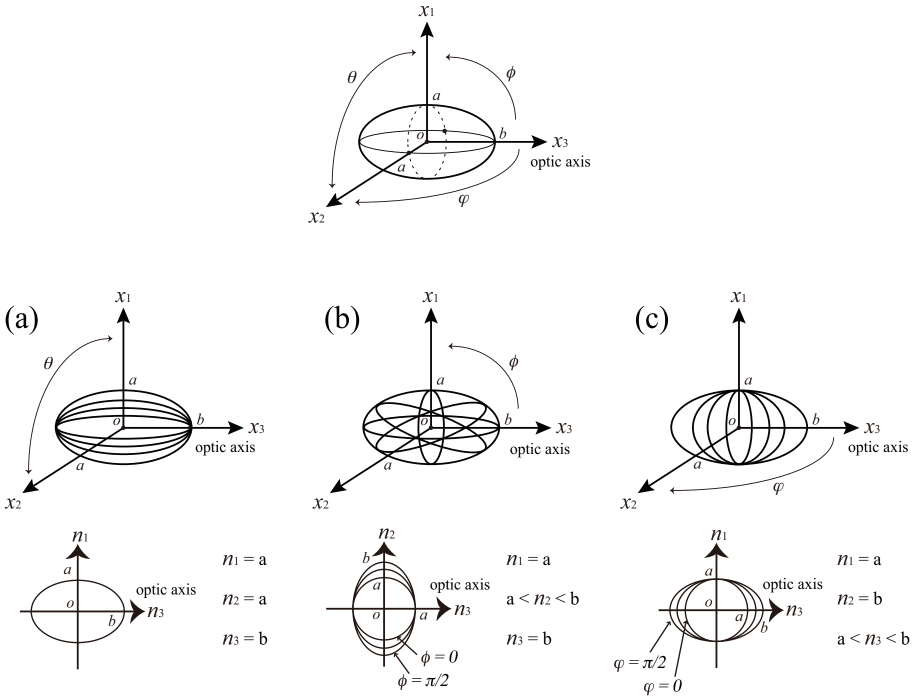

Figure 2.17: Cross sections of the indicatrix. Clearly, (b) and (c) are identical for this case treating an uniaxial material.

the earlier section, a polarizer-analyzer configuration at $\theta = \pi/2$ blocks the light from the source to reach the observer. This happens because the polarization component of the beam is mostly perpendicular to TA2. Therefore, even in this configuration, some portion of the beam could reach the observer by creating a polarization component that is not perpendicular to TA2.

When the optical axis of medium 1 is either in parallel or crossed configuration to TA1 ($\varphi = 0$ or $\pi/2$), I_1 propagates in the respective speed that it is allowed there corresponding to n_o or n_e. That case, polarization state of I_2 is identical to I_1. However in the case of $\varphi \neq 0$ or $\pi/2$, which as drawn in Figure 2.18, I_1 splits to respective components corresponding to *o*- and *e*-axes. In medium 1, two polarizations propagate in respective speeds permitted on each of n_o andn_e. In this diagram, n_e is larger than n_o, so that means it travels slower.

Beam that comes out from material 1 (I_2) again propagates through the air. Because air is an

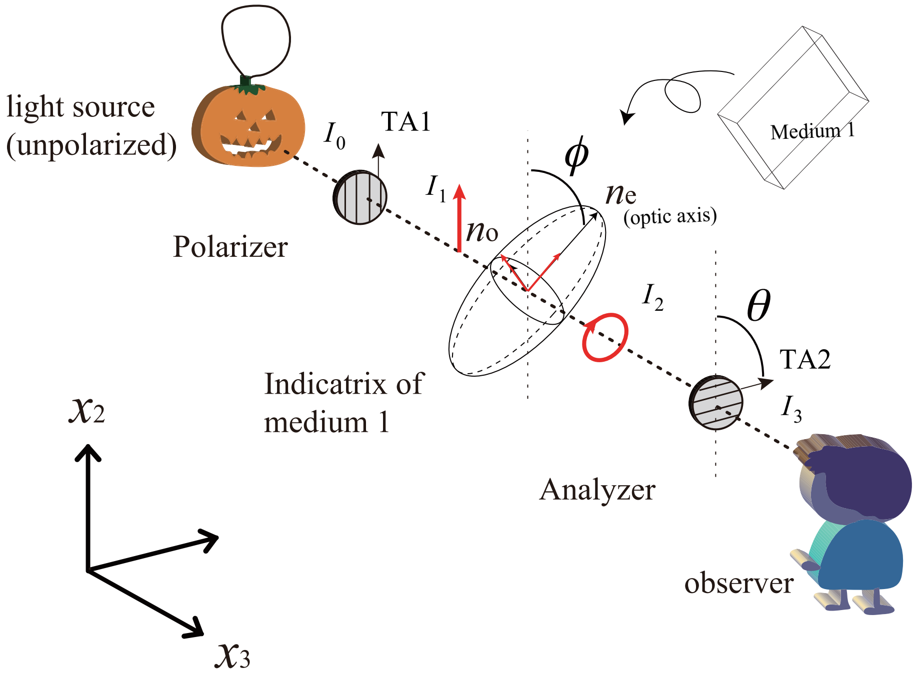

Figure 2.18: Uniaxial substance sandwiched between the polarizer-analyzer system.

isotropic medium, the two polarizations that once were split in medium 1 interfere back. Taking the retardation ϕ into account, the beam combination is expressed using Eq. (2.91) as below.

$$E_x = E_o \cos(\omega t - kz), \tag{2.103}$$

$$E_y = E_e \cos(\omega t - kz + \phi), \tag{2.104}$$

where $\phi \neq 0$. This is the expression of circular/elliptical polarization that rotates clockwise. That's why it is drawn as you see there in the figure. The angle $\varphi = \pi/4$ gives an equal split of components to the respective axis, so the intensity that the observer observes at the crossed Nicol ($\theta = \pi/2$) configuration gives the information about φ, the retardation.

By applying Malus's law, power at the observer's point can be predicted by calculation in the case having an uniaxial material in between. This is demonstrated in the next section.

2.10.4 Iridescence[87]

A brief mechanism of iridescence is explained here, because it explains why the tint-plate view of the polarized optical microscope can be viewed by colors (Section 3.4.1).

Iridescence is an optical phenomenon in which hue changes with the angle from which a surface is viewed. Iridescence is caused by multiple reflections from multi-layered, semi-transparent surfaces in which phase shift and interference of the reflections modulates the incident light (by amplifying or attenuating some frequencies more than others). This process is the functional analog of selective wavelength attenuation.

2.11 Conclusions

Physical models of fiber modes were explained in both aspects of geometrical optics and wave-propagation theory. Numerical expression of Gaussian beam was explained as the model of beam propagation phenomenon in homogeneous medium. Based on these backgrounds, hypotheses of polarization-maintaining phenomenon of LBLC MMF (core diameter around 500 μm) was discussed, in which they are summarized as follows.

(1) Intrinsic irregularity of structure has less affection to the breakage of LP degeneracy because the core birefringence is low.

(2) Outer disturbance such as bending has less affection to the breakage of LP degeneracy because those affects only locally compared to the SMFs.

(3) There is huge amounts of LP modes in a similar energy level that the light can go into without changing the original polarization state.

In the latter part, some basics on two birefringence types that could exhibit in plastic was explained. Lastly, polarimetry of one-axis optical medium and iridescence were explained.

Chapter 3

EXPERIMENTAL METHODS

3.1 Preface

Fabrication and measurement procedures of the P(MMA/BzMA)POF (poly-methyl methacrylate/benzyl methacrylate copolymer plastic optical fiber) are explained in this chapter. Materials, polymerization conditions, and heat drawing condition employed for the fiber fabrication are described in the first section. The second section explains the equipment and procedure used to measure refractive index profile of the fiber core. The third section describes measurement regarding polarized optical microscopy used to measure the birefringence distribution of a fiber. Finally, the last section explains about the variation of extinction ratio (ER) measurements used to characterize the polarization-maintaining property of the fiber. Near field pattern (NFP) measurement used to characterize the mode path is explained as well.

3.2 P(MMA/BzMA)POF preparation

P(MMA/BzMA)POF was fabricated as described in Figure 3.1. Materials used to fabricate the fiber are listed in Figure 3.2 with the structures. Methyl methacrylate (MMA; Mitsubishi Gas Chemical Company) was polymerized into a tubular geometry with a closed end (inner/outer diameter: 14.7/22.0 mm, length: 600 mm) as shown in Figure 3.1(a). MMA solution was prepared by adding polymerization initiator, t-butyl peroxy-2-ethylhexanoate (Perbutyl-O, Wako Pure Chemical Industries, Ltd.), and chain transfer agent, 1-butanethiol (NOF Corporation), at the composition of 0.5 wt% (percent in weight) and 0.278 wt%, respectively of the whole solution weight. The solution was placed in a glass container (inner diameter: 22.0 mm, length 600 m) and heated at 70℃ water bath for 100 minutes until the solution polymerizes to waxy state. Later, the glass container was span at 2000-3000 rpm for 3 hours under 70℃ oven until the content hardens at the container's inner wall. After a 24 hour-heat treatment at 90℃, poly-methyl methacrylate (PMMA) tube was removed from the glass container. This PMMA tube is later used as the fiber cladding.

A solution of MMA and benzyl methacrylate (BzMA; Wako Pure Chemical Industries, Ltd.) was prepared as the core material of the fiber (Figure 3.1(b)). Core solutions with three different MMA/BzMA ratio was prepared, namely, 77:23, 82:18, and 87:13. Here, 82:18 is the optimum composition for eliminating orientational birefringence using this monomer pair[84]. For the core solution, di-t-butyl peroxide (Perbutyl-D, Wako Pure Chemical Industries, Ltd.) and 1-dodecanethiol (NOF Corporation) were respectively used as polymerization initiator and chain transfer agent. Each were added at the composition of 0.0159 wt% and 0.278 wt%, respectively. The solution was placed in the center cavity of the PMMA tube prepared in advance, then polymerized at under 120℃ in 0.6 MPa nitrogen atmosphere for 48 hours.

The core refractive index was profiled during the process of polymerization. As shown in Figure 3.1(b), when monomer is placed adjacent to polymer, gel effect[88] occurs, which is known to accelerate the polymerization. The gel effect is caused by monomer diffusing into polymer at their interface, so the monomer solution polymerizes from the inner wall of the PMMA tube to the center. Since MMA has a smaller molecular volume than BzMA (Figure 3.2), it is more diffusive and contributes more to the gel effect. A large number of BzMA monomers are displaced into the center while MMA mainly polymerizes from the interface. This results in the final polymer containing a higher number of BzMA monomeric units in the center. Since poly-benzyl methacrylate (PBzMA) has a higher refractive index than the PMMA; thus, the polymerized rod has a graded refractive index.

Achieved preform was heat-drawn in a furnace with a maximum internal temperature of 210℃ (Figure 3.1(c)). While entering the furnace, the preform was simultaneously pulled in the longitudinal direction by the bottom take-up roll. The entering and pulling velocities respectively were 3.66 mm/min and 1.4 m/min. These velocities were chosen to have a draw ratio (pulling velocity/entering velocity) of 382.5 and the fiber draw tension to be in the range of 2.5-3.0 N. Test fiber was obtained from the region with 750/1125 μm (or 667/1000 μm) at the core/fiber diameter with ± 10 μm fluctuation.

(a) PMMA cladding

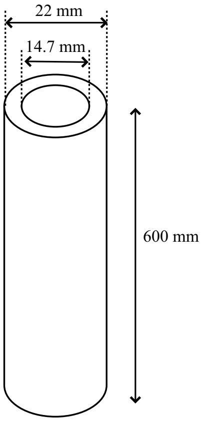

Conversion at water bath at 70 deg. (100 minutes)

Spun at 2000-3000 rpm at 70 deg. (3 hours)

Heat treatment at 90 deg. (24 hours)

Initiator: t-butyl peroxy-2-ethylhexanoate (Perbutyl-O; 0.5 wt%)

Chain transfer agent: 1-butanethiol (n-BM, 0.278 wt%)

(b) P(MMA/BzMA) core

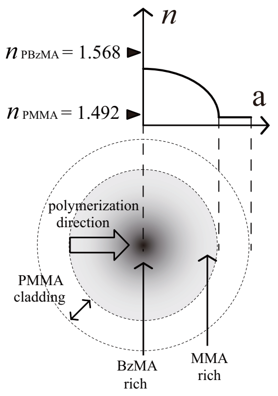

Conversion at 0.6 MPa nitrogen atmosphere at 120 deg. (48 hours)

Initiator: di-t-butyl peroxide (Perbutyl-D; 0.0159 wt%)

Chain transfer agent: 1-dodecanethiol (n-LM; 0.278 wt%)

(c) Preform drawing

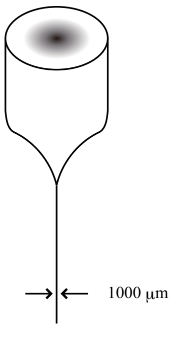

Furnace maximum temp.: 210 deg

Draw ratio: 382.5

Draw tension: 2.5-3.0 N

Figure 3.1: Schematic of P(MMA/BzMA)POF fabrication procedure: polymerization of (a) PMMA cladding, (b) P(MMA/BzMA) core, and (c) heat drawing of preform. (b) also describes the interfacial gel polymerization using the gel effect of the PMMA cladding and the core solution.

MMA $CH_2=C(CH_3)COOCH_3$

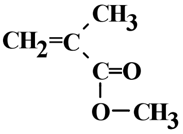

Molecular weight: 100.12

Density: 0.936 (@25 deg)

Reractive index: 1.414 (polymer 1.492)

BzMA $CH_2=C(CH_3)CO_2CH_2C_6H_5$

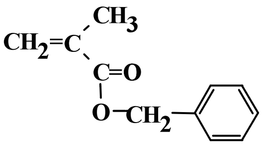

Molecular weight: 176.21

Density: 1.04 (@25 deg)

Reractive index: 1.512 (polymer 1.568)

Perbutyl-O $C_{12}H_{24}O_3$

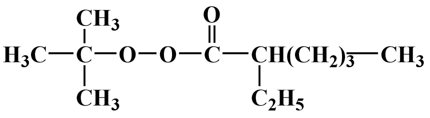

$$H_3C-C(CH_3)_2-O-O-C(=O)-CH(C_2H_5)(CH_2)_3-CH_3$$

Molecular weight: 216.32

Density: 0.913 (@0 deg)

1 hour half life temperature: 92.1 deg.

Perbutyl-D $C_8H_{18}O_2$

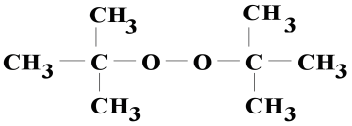

$$CH_3-C(CH_3)_2-O-O-C(CH_3)_2-CH_3$$

Molecular weight: 146.23

Density: 0.796 (@20 deg)

1 hour half life temperature: 144.1 deg.

n-BM $CH_3(CH_2)_3SH$

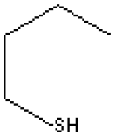

Molecular weight: 90.2

Density: 0.83

n-LM $CH_3(CH_2)_{11}SH$

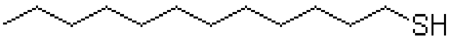

Molecular weight: 202.401

Density: 0.845

Figure 3.2: Structures of the materials used for P(MMA/BzMA)POF fabrication.

3.3 Measurement of refractive index profile

Refractive index profile of P(MMA/BzMA)POF core was measured by transverse interferometric technique developed by Ohtsuka and Koike[89] using an interference microscope (Interphako; Carl Zeiss) at sodium D line (589 nm).

Standard plot of P(MMA/BzMA) composition versus refractive index (at D line) was obtained by measuring refractive indices of copolymers in different compositions using prism coupler (Model 2010; Metricon Corp.). The standard plot was obtained at the purpose to correspond the fiber index profiles to the published optimum values for eliminating orientational and photoelastic birefringence[84]. Figure 3.3 shows the standard plot and the elimination compositions.

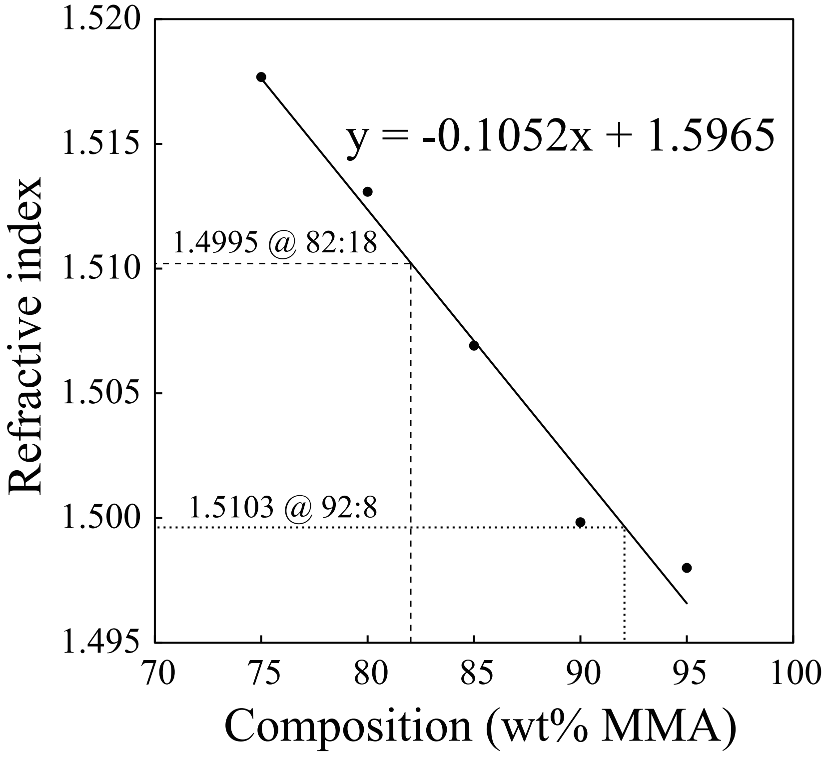

Figure 3.3: Standard plot of P(MMA/BzMA) composition versus refractive index. Elimination compositions (orientational: 82/18, photoelastic: 92:8) are shown with the broken lines.

3.4 *Birefringence measurement using polarized optical microscopy*

Birefringence in an optical fiber was measured using polarized optical microscopy. Figure 3.4 shows the basic construction of the polarized optical microscope (BX51, Olympus Corporation)[83]. Fiber slices in vertical and horizontal directions were prepared as described in Figure 3.5.

3.4.1 *Measurement using a sensitive tint plate[90]*

The distribution manner of the birefringence was observed by viewing the fiber slices by the polarized optical microscope with a sensitive tint plate (U-TP530, Olympus). Amount of birefringence that corresponds to each color was estimated from interference color chart provided by Olympus. Although the chart provides birefringence value in a brief estimate, accuracy is lower than the measurement using Berek compensator (explained in the next section). Sensitive tint plate is useful for understanding the birefringence distribution from the image. The plate was set at the position shown

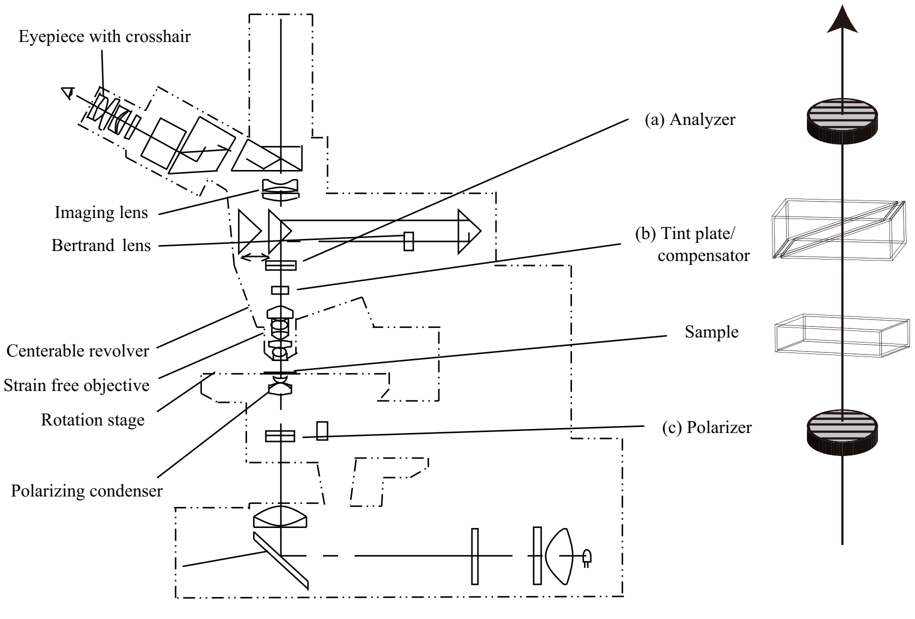

Figure 3.4: Construction of the polarized optical microscope[83].

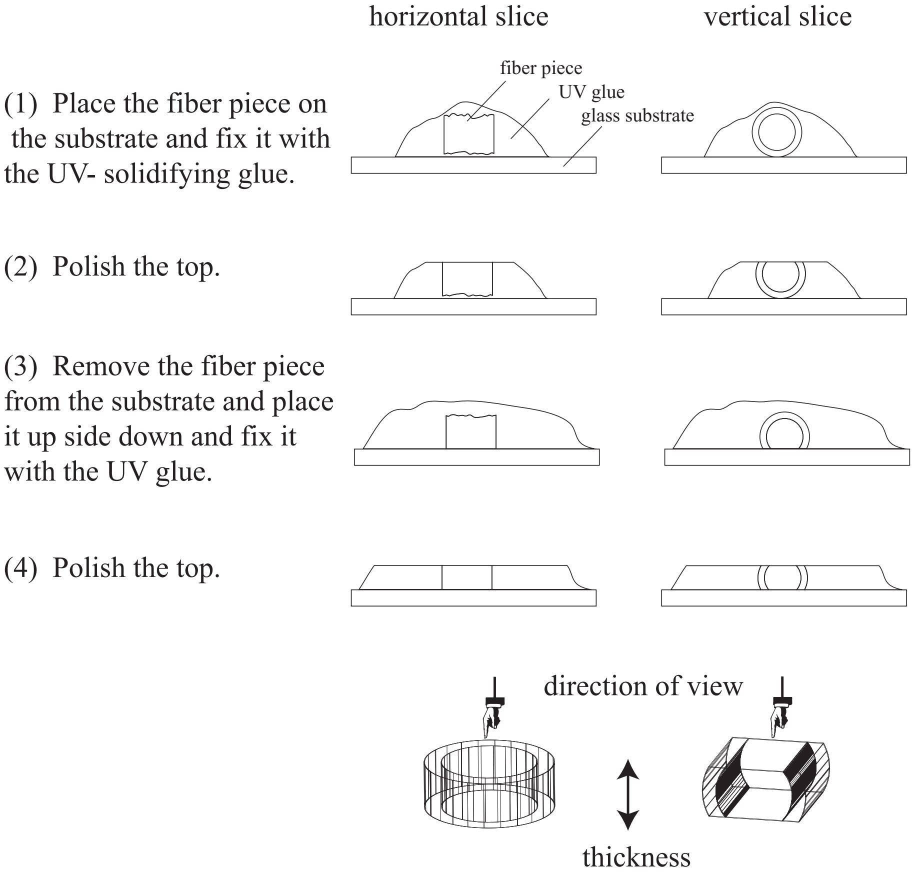

Figure 3.5: Steps to fabricate fiber slices (in horizontal and vertical) for a purpose of viewing the birefringence using the polarized optical microscope.

in Figure 3.4(b) with its optical axis tilted in 45° to the ray oscillatory. Analyzer (a) and polarizer (c) were set in the crossed-Nicol configuration.

A sensitive tint plate can be used to introduce color contrast in polarized light images, and consists of a slice of birefringent material, usually gypsum, mica or quartz. The slice is cut or cleaved parallel to the optical axis of the crystal, to such a thickness that the *o*-rays and *e*-rays[1] for green light (l = 540 nm) are out of phase by exactly one wavelength. The analyzer therefore

---

[1] ordinary and extraordinary rays: refer Section 2.10.3.

extinguishes green light, but permits other wavelengths to pass through to some extent. When using white light this causes the field of view to appear red (white light minus green light). Isotropic, non-birefringent materials also appear red. The physics of this color exhibition is a matter of iridescence that is explained in the earlier chapter.

The sensitive tint plate increases the observed birefringence by one wavelength. The path difference between the *o*-rays and *e*-rays emerging from an anisotropic crystal adds or subtracts from this single wavelength path difference. Individual regions in the optical fiber appear to exhibit differences in color, depending on their composition and chain orientation.

3.4.2 Measurement using a Berek compensator[91]

Quantitative value of birefringence at each local point of the fiber was measured using Berek compensator with the polarized optical microscope. Plate was set at the position shown in Figure 3.4(b) with its optical axis tilted in 45° to the ray oscillatory. Analyzer (a) and polarizer (c) were set in the crossed-Nicol configuration.

An optical compensator is a device that allows one to control the retardation of a wave passing through it with a wider range freedom than the tint plate. In a wave plane retarder such as the tint plate, the relative phase change ϕ between the *o*- and *e*-waves depends on the plate thickness and cannot be changed. In compensators, ϕ is adjustable.

The Berek compensator is an optical device that is capable of quantitatively determining the wavelength retardation of a crystal, fiber, mineral, plastic film or other birefringent material. Provided the thickness of the material can be measured, a Berek compensator can be utilized to ascertain the birefringence value. The compensator operates by measuring the rotation angle of a calcite or magnesium fluoride optical plate cut perpendicular to the optical microscope axis.

In a Berek compensator adjusted for zero retardation, the single birefringent uniaxial crystalline plate is oriented with the *e*-optical axis perpendicular to the surface of the crystal and parallel to the microscope optical axis. Polarized light passing through the specimen encounters the compensator at normal incidence (0°) and propagates through the compensator with a velocity that is independent upon the direction of polarization. In other words, the Berek compensator acts as an ordinary isotropic material when the birefringent plate is perpendicular to the microscope optical axis, and thus, has no effect on polarized light passing through.

As the compensator plate tilt adjustment dial is rotated (Figure 3.6) with respect to the direction of incident polarized light (and microscope optical axis), the incident plane coincides with the refractive index plane of the *e*-axis and alters the velocity of light passing through the crystal. In general, the polarized wavefront is retarded by a measurable quantity that is dependent upon the

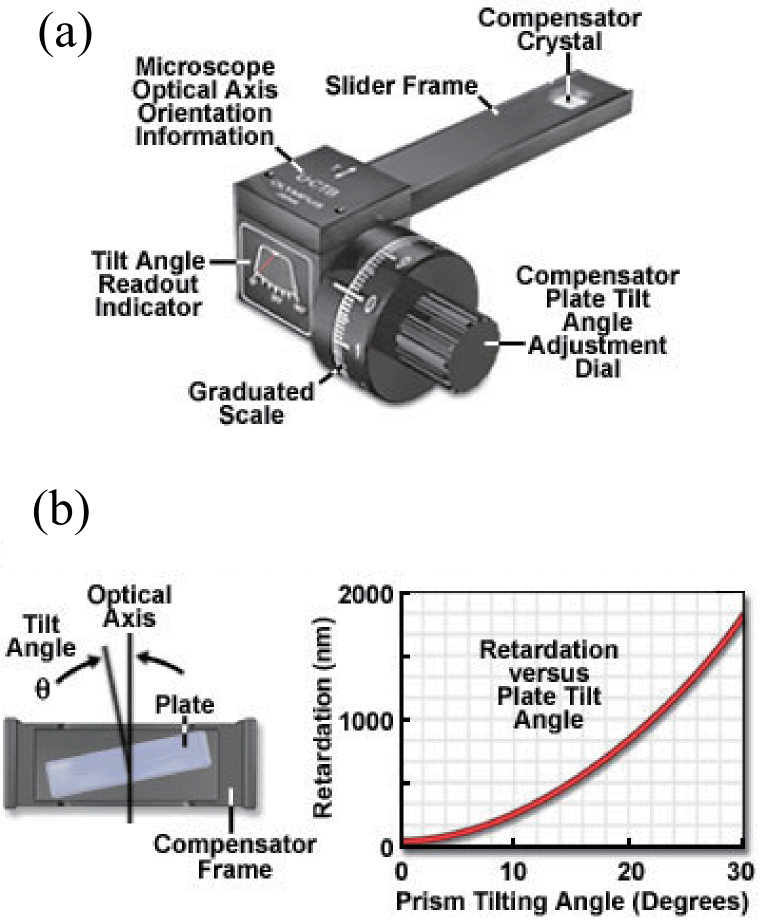

Figure 3.6: (a): Berek compensator anatomy[91]; (b): Plate angle and retardation[91].

angle of tilt and the wavelength of illumination. Simultaneously, light polarized perpendicular to the incident plane continues to propagate through the compensator plate along the *o*-axis and with a velocity that remains independent upon the tilt angle. As a net result, polarized light exiting the specimen and passing through a tilted Berek compensator is retarded by an additional amount by the compensator and accumulates a relative phase shift (dependent upon the tilt angle), which can be measured with the device. The degree of optical path difference introduced by a Berek compensator is determined by the thickness of the birefringent plate, the wavelength of illumination, the refractive index difference between the *o*- and *e*- axes of the compensator crystal, and the tilt angle. Most manufacturers compound all of these quantities into a constant that is utilized to calibrate the retardation vernier scale. Olympus is not an exception.

Max Berek developed this style of polarization compensator in 1913 as a variable waveplate that can impose a quarter or half-wave retardation at any wavelength between 200 and 2800 nm (5 wavelengths), dramatically reducing the number of compensation plates necessary for quantitative polarized light microscopy. Subsequent design improvements enable the measurement of retardation values between a range of zero and 11,000 nm (20 wavelengths) for measurements of very high retardation values. As discussed above, the original Berek compensator consisted of a single cut plate of uniaxial birefringent material (calcite or magnesium fluoride) having an *e*-optical axis perpendicular to the long dimension of the plate frame (Figure 3.6). The birefringent plate is tilted about the horizontal axis by means of a calibrated micrometer drum to enable precise measurements of retardation.

As illustrated in Figures 3.6(a)(b), the Berek compensator is equipped with a tilting calcite plate housed in a rectangular frame and controlled by a rotating drum knob affixed to a vernier scale. The compensator is positioned in the microscope intermediate tube at a 45° angle with respect to the polarization directions of the polarizer and analyzer, and the retardation is varied by turning the compensator knob. Rotating the vernier dial on the compensator inclines the birefringent plate relative to the microscope optical axis (see Figure 3.6(b)). As the plate is tilted, the retardation value is increased.

In practice, a birefringent specimen is placed on the microscope stage and rotated until it attains the extinction position (where the features of interest become dark). Next, the stage is rotated +45° and clamped into place. The compensator drum knob is set to a position of 30° (turning the knob in a single direction to avoid backlash) and inserted into the microscope intermediate tube. Finally, the compensator knob is rotated to confirm that the black fringe intersects the center of the field of view. If the fringe does not intersect the center, the stage is rotated by 90° and re-clamped. An interference filter having a transmission bandwidth between 540 and 570 nanometers will improve the accuracy of measurements, but also produces multiple black fringes in addition to the one that is visible in the absence of the filter. A reference table gives the optical path differences for the tilt angle in which compensation is achieved.

In detail, birefringence value is obtained by dividing retardation by the sample thickness, whereas the retardation is calculated from the compensator angle between two interference patterns that are observed at the focal point.

3.5 Extinction ratio measurement

The first part of this section explains the ER measurements with variations of launching conditions that were used for a fair comparison of polarization-maintaining property among multimode fibers (MMFs) with different core diameters. Next, methods developed for generating phase shift by the photoelastic effect are explained. Retarder devices used for determining the amount of phase shift are explained as well.

3.5.1 Extinction ratio of an optical fiber

Figure 3.7 shows the simplest ER measurement setup. ER is a parameter representing how the fiber maintains polarization state while the propagation. A He-Ne laser of 633.3-nm output (Melles Griot) was used as the light source. Wavelength was chosen because of its affinity with transmission window of the PMMA based POFs. Output light from the optical fiber passes through an analyzer. The light from the analyzer was detected by a power meter. The system structure is identical to Figure 2.15 in the earlier section that discusses Malus's law.

The difference is that the analyzer rotates over 180° with power detected at certain angle intervals

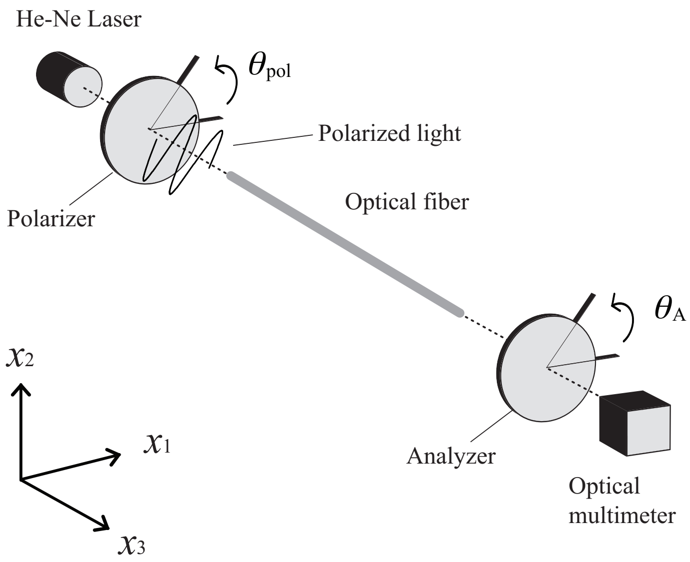

Figure 3.7: Extinction ratio measurement of an optical fiber. θ_{pol} is the angle of the light vibration referring to the x_1-x_2 plane. θ_{A} is the angles of the analyzer. Output light from the test fiber is measured by the power meter for a total 180° rotation of θ_{A}.

(in this research, 10° interval is often used). During the full rotation, the polarizer and the analyzer experiences both parallel and crossed Nicol configurations, once at least. Power curve drawn at the full rotation should take a sinusoidal form that includes maximum (I_{max}) and minimum (I_{min}) intensities that respectively corresponds to the parallel and crossed Nicol configurations. With these values, ER is calculated as below.

$$\mathrm{ER\ (dB)} = -10log\left(\frac{I_{\mathrm{min}}}{I_{\mathrm{max}}}\right) \tag{3.1}$$

The higher ER means that it has a large contrast between I_{max} and I_{min}, which means that the fiber has a high polarization-maintaining property. On the other hand, low ER means that I_{max} and I_{min} are almost same, which means that the fiber disturbed the polarization regularity in a high magnitude.

θ_{pol} shown in Figure 3.7 is the angle of the light vibration referring to the x_1-x_2 plane in which the x_3 axis is the light propagation direction. This angle matters when dealing with photoelastic effect that will be discussed in a moment.

3.5.2 Launching conditions

Schematic diagrams of two launching conditions that are used in this research are shown in Figure 3.8.

3.5.2.1 Pinhole launching

Figure 3.8(a) shows the nearly all-mode excitation measurement apparatus using a pinhole. Light from the laser was aligned to pass through a polarizer, a half-wave plate (HWP)[2], and a pinhole (spot diameter: 400 μm) before coupling to the test fiber. The pinhole was in physical contact to the fiber end and positioned at the core center in order to launch dominant modes while avoiding the cladding modes. HWP was used to control θ_{pol}. Phase optics in HWP is explained in the latter section that treat retarders.

3.5.2.2 Point launching

For differential mode excitation, point-launching setup shown in Figure 3.8(b) was used. Light from the He-Ne laser was coupled to a custom-made setup (OZ Optics Ltd.) that was assembled in a sequence of a laser-to-fiber coupler, a singlemode fiber (SMF), a polarizer, and a polarization-maintaining fiber (PMF). SMF and PMF were typical glass-based types with core diameter less than 10 μm. Polarized light from the PMF was butt-coupled to the test fiber. Position of the PMF end was controlled by a two-axes manipulator (Suruga Seiki Co.,Ltd.) in order to launch various offset-points at the core, namely, 0, 25, 50, 75, and 100% of the core radius. θ_{pol} was controlled by rotating the end of the PMF.

---

[2] HWP: a kind of retarder plate that is capable in changing oscillation plane of the incident linear polarization by creating half-wavelength (π) retardation. Refer Section 3.5.4.1 for more detail.

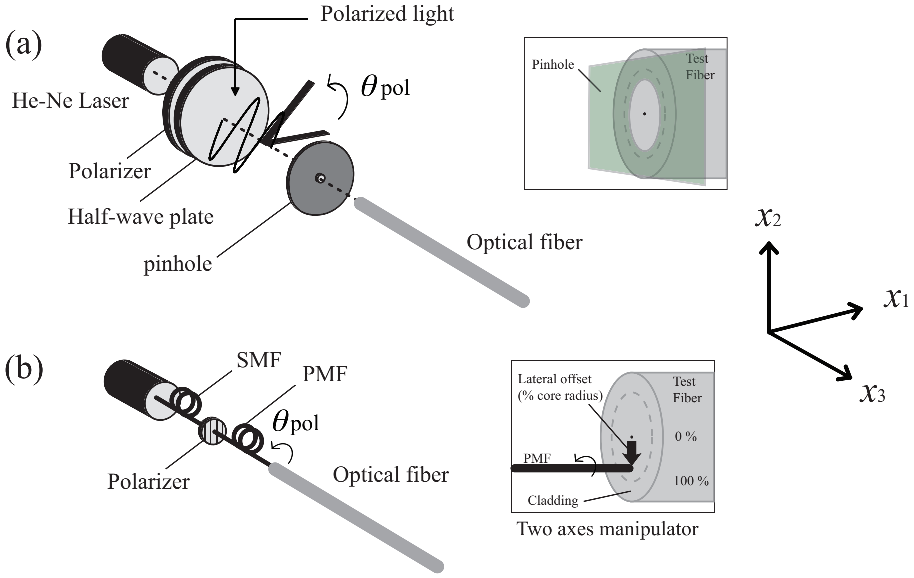

Figure 3.8: Variations of launching condition. (a) pinhole (diameter = 400 μm) launching, and (b) point launching using glass based PMF.

3.5.3 *Methods to induce phase change in the optical fiber*

Photoelastic effect was induced by applying plane symmetrical stress to the optical fiber. In particular, macrobending along a plane and single-directional stress are used. Schematic diagrams of each setups are shown in Figure 3.9. Magnitude of stress, considerable phase shifting factor, was varied by changing the loop diameter/number and amount of weight respectively for each of (b) and (c) in Figure 3.9.

Acrylic cylinder with polished surface was used as the macrobending rod. Bending rod was rested in the $x_1 - x_3$ plane with the cylinder circumference intersecting the straitened fiber's path as shown in Figure 3.9(b). Fiber was winded along the $x_1 - x_3$ plane without making some space in the x_2 direction. Rods of 10, 5, 4 cm diameter were prepared for testing. Using 1-m test fiber, numbers of loops created along each rods are one (for 10-cm rod), two (for 5-cm rod), and three (for 4-cm rod).

For the $-x_2$ stress, acrylic boards with polished surface was used for both top and bottom plates.

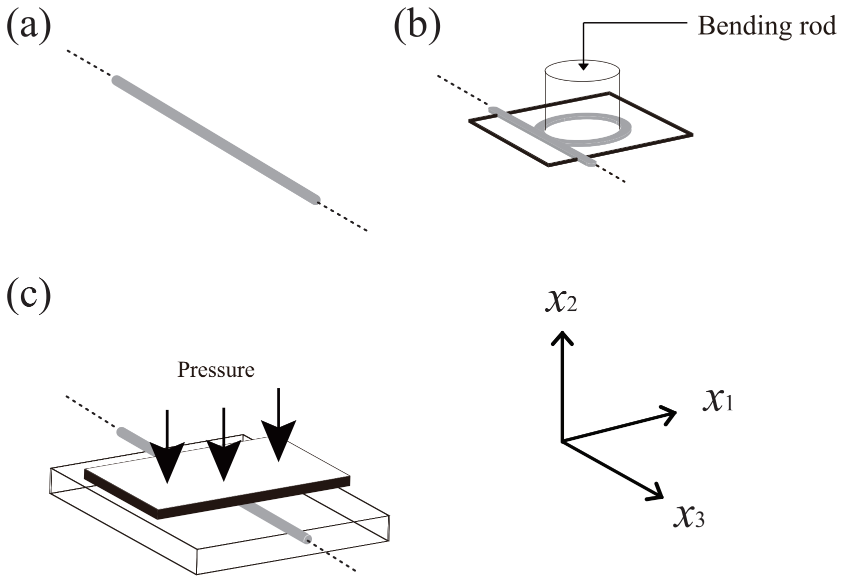

Figure 3.9: Ways used to induce stress-induced birefringence in an optical fiber. (a) Straight (default/no birefringence). (b) Macrobending. (c) -x_2 pressure.

Dimension of plates and some other specific conditions are mentioned in Chapter 7.

3.5.4 Retarders used at the output

This section explains how and which retarder plates were used for analyzing the phase of the output light. As shown in Figure 3.10, retarder plate was inserted between the fiber end and the analyzer.

3.5.4.1 Retarding plates: half-, quarter-wave plates[81]

Consider a positive uniaxial crystal such as quartz ($n_e > n_o$)[3] plate that has the optical axis (taken along x_3) parallel to the plate faces as in Figure 3.11(a). Suppose that a linearly polarized wave is incident at normal incidence on a plate face. If the field **E** is parallel to the optical axis (shown as $E_{//}$), then this wave will travel through the crystal as an *e*-wave with a velocity c/n_e slower than the *o*-wave since $n_e > n_o$. Thus, optical axis is the ”slow axis” for waves polarized parallel to it. If

---

[3] $n_e > n_o$: Refractive index corresponding to *e*-ray path is greater than that of ordinary.

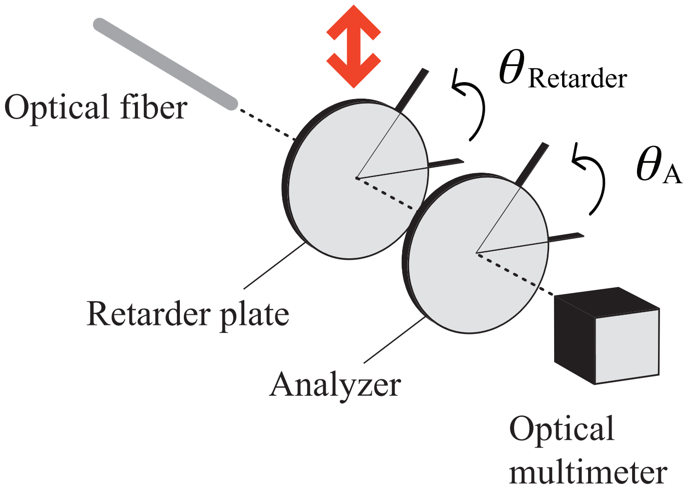

Figure 3.10: Retarder plate in the ER measurement setup.

E is right angles to the optical axis (shown as $E_\perp$), then this wave will travel with a velocity c/n_o, which will be the fastest velocity in the crystal. Thus the axis perpendicular to the optical axis (x_1) will be the ”fast axis” for polarization along this direction. When a ray enters a crystal at normal incidence to the optical axis and plate surface, the *o*- and *e*-waves travel along the same direction as shown in the figure. We can resolve a linear polarization at an angle α to x_3 into $E_{//}$ and $E_\perp$. When the light comes out at the opposite face, these two components would have been phase shifted by ϕ. Depending on the initial angle α of **E** and the length of the crystal, which determines the total phase shift ϕ through the plate, the emerging beam can have its initial linear polarization rotated, or changed into an elliptically or circularly polarized light as summarized in Figure 3.11(b)(c).

If L is the thickness of the plate then the *o*-wave experiences a phase change $k_{o-\text{wave}}L\lambda$ through the plate where $k_{o-\text{wave}}$ is the wavevector of the *o*-wave: $k_{o-\text{wave}} = (2\pi/\lambda)n_o)$, where λ is the free-space wavelength. Similarly, the *e*-wave experiences a phase change $2\pi/\lambda)n_eL$ through the plate. Thus, the phase difference ϕ between the orthogonal components $E_\perp$ and $E_{//}$ of the emerging beam is:

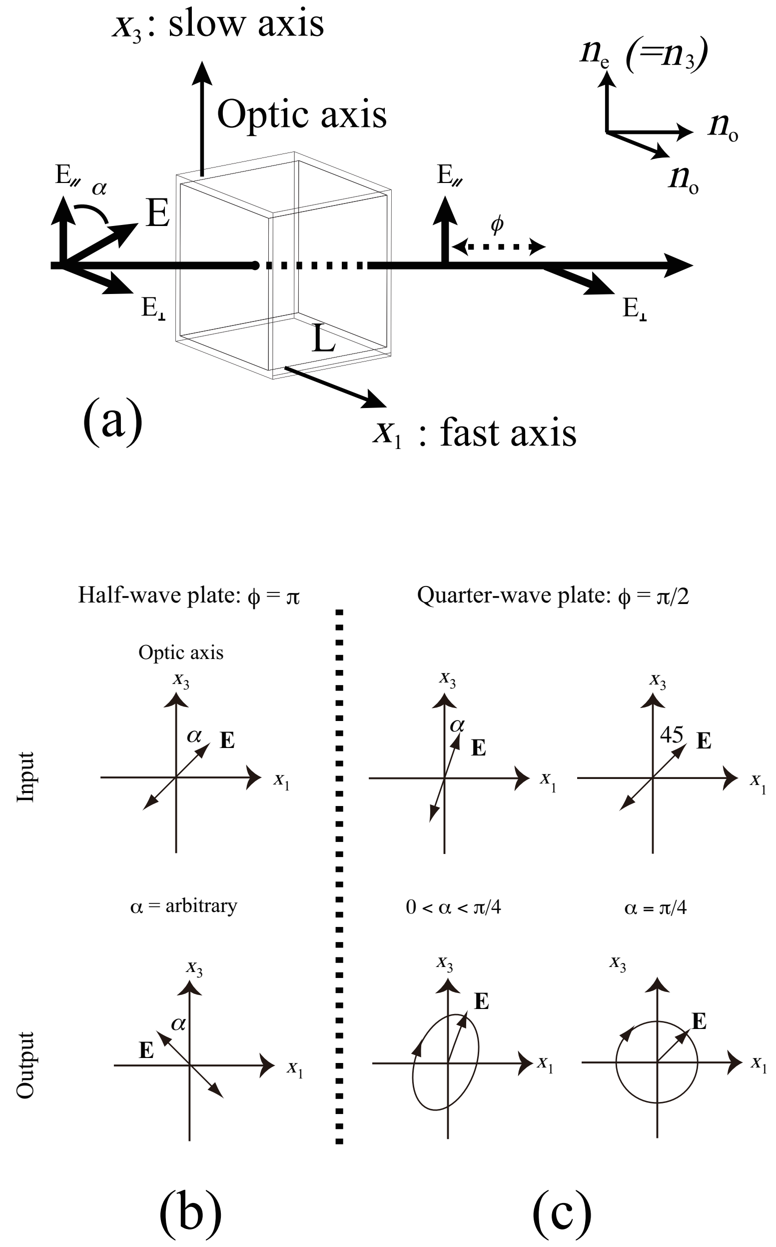

Figure 3.11: (a) A retarder plate. The optical axis is parallel to the plate face. The *o*- and *e*-waves travel in the same direction but at different speeds. Input and output polarizations of light through (b) a HWP and through (b) a QWP.

$$\phi = \frac{2\pi}{\lambda}(n_e - n_o)L. \tag{3.2}$$

The phase difference ϕ expressed in terms of full wavelengths is called the retardation of the plate. (*e.g.* a phase difference ϕ of 180° is a half-wavelength retardation.)

The polarization of the through beam depends on the crystal type, $(n_e - n_o)$, and the plate thickness L. We know that depending on the phase difference ϕ between the orthogonal components of the field, the EM wave can be linearly, circularly or elliptical polarized as in Figure 2.14.

A HWP has a thickness L such that the phase difference ϕ is π, corresponding to $\lambda/2$ of retardation. The result is that, $E_{//}$ is delayed by $\pi/2$ with respect to $E_{\perp}$. If we add the emerging $E_{\perp}$ and $E_{//}$ with this phase shift ϕ, **E** would be at an angle $-\alpha$ to the optical axis and still linearly polarized. **E** has been rotated counterclockwise through 2α.

A quarter-wave plate (QWP) retarder has a thickness L such that the phase difference ϕ is $\pi/2$, corresponding to $\lambda/4$ of retardation. If we add the emerging $E_{\perp}$ and $E_{//}$ with shift ϕ, the emerging light will be elliptically polarized if $0 < \alpha < \pi/4$ and circularly polarized if $\alpha = \pi/4$.

3.5.4.2 Soleil-Babinet Compensator[81]

Soleil-Babinet compensator is an optical device that is used for controlling and analyzing the polarization state of light. Consider the optical structure depicted in Figure 3.12 which has two quartz wedges touching over their large faces from a ”block” of adjustable height d. Sliding one wedge over the other wedge alters the ”thickness” d of this block. The two-wedge block is placed on a parallel plate quartz slab with a fixed thickness D. The slab has its optical axis parallel to its surface face. The optical axes in the wedges are parallel but perpendicular to the optical axis of the slab as indicated in the figure.

Suppose that a linearly polarized light is incident on this compensator at normal incidence. We can represent this light by field oscillations parallel and perpendicular to the optical axis of the two-wedge block; these fields are E_1 and E_2 respectively. The polarization E_1 travels through the wedges (d) experiencing a refractive index n_e (E_1 is along the optical axis) and travels through the plate (D)

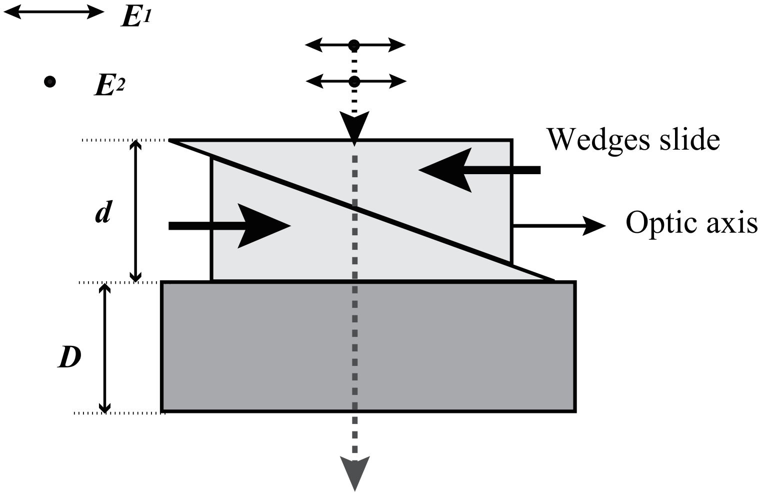

Figure 3.12: Soleil-Babinet compensator.

experiencing an index n_o (E_1 perpendicular to the optical axis). Its phase change is:

$$\phi_1 = \frac{2\pi}{\lambda}(n_e d + n_o D). \tag{3.3}$$

But the E_2 polarization wave first experiences n_o through the wedges (d) and then n_e through the plate (D) so that its phase change is,

$$\phi_2 = \frac{2\pi}{\lambda}(n_o d + n_e D). \tag{3.4}$$

The phase difference $\phi(=\phi_2 - \phi_1)$ between the two polarizations is:

$$\phi_2 = \frac{2\pi}{\lambda}(n_e - n_o)(D - d). \tag{3.5}$$

It is apparent that as we can change d continuously by sliding the wedges (by using a micrometer screw), we can continuously alter the phase difference ϕ from 0 to 2π. We can therefore produce a quarter-wave or half-wave retardations by simply adjusting this compensator. It should be emphasized that this control occurs over the surface region that corresponds to both the wedges and in practice this is a narrow region.

3.5.5 Calculation of the output intensity

Output intensity at a system consisting of polarizer, phase retarding medium (fiber), and analyzer can be calculated by the procedure shown below. The basic principal is same as the Mauls's law (Section 2.10.2). Here, all kinds of optical losses and temperature affection are ignored.

As shown in Figure 3.13, linearly polarized light obtained from the polarizer is named E_{inc}.

$$E_{inc} = A\cos(\rho) \tag{3.6}$$

A and ρ are amplitude and phase of this E-wave. When this light propagates through a fiber with optical axes in x_1 and x_2 directions[4], projection components of E_{inc} to the respective directions[5] are expressed as follows.

$$\text{OA1:} \qquad E_1 = E_{inc}\cos\theta_{pol} = A\cos\theta_{pol}\cos(\rho) \tag{3.7}$$

$$\text{OA2:} \qquad E_2 = E_{inc}\sin\theta_{pol} = A\sin\theta_{pol}\cos(\rho+\phi) \tag{3.8}$$

ϕ is the phase difference between the *o*- and *e*-paths at the time when these components are interfering back at the fiber end. The new polarization state is expressed by Eq. (3.8) and it is not necessarily linear as the purple wave shown in the figure. After passing through the analyzer, these components are again filtered out.

$$E_1^A = E_1\cos\theta_A = A\cos\theta_{pol}\cos\theta_A\cos(\rho) \tag{3.9}$$

$$E_2^A = E_{inc}\sin\theta_A = A\sin\theta_{pol}\sin\theta_A\cos(\rho+\phi) \tag{3.10}$$

---

[4] Directions of optical axes are apparent, because all the conditions shown in Figure 3.9 are $x_1 - x_3$ plane symmetrical.

[5] correspond to the *o*- and *e*-waves

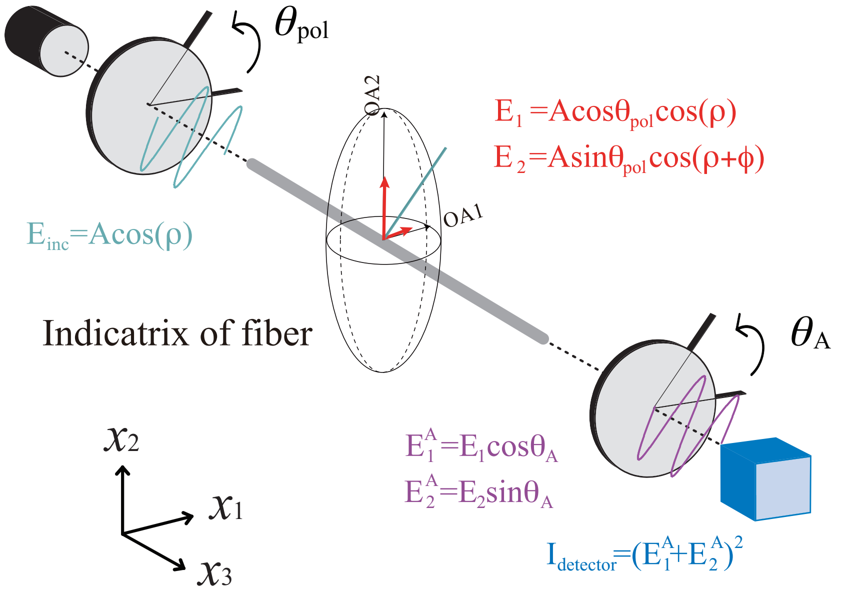

Figure 3.13: Schematic explanation of vectors of the transmitting components.

Intensity measured at the power meter is square of the E-field. By having $\rho = 0$,

$$I_{detector} = (E_1^A + E_2^A)^2 \tag{3.11}$$

$$= (A\cos\theta_{pol}\cos\theta_A + A\sin\theta_{pol}\sin\theta_A\cos\phi)^2 \tag{3.12}$$

$$\begin{aligned} &= (A\cos\theta_{pol}\cos\theta_A)^2 + (A\sin\theta_{pol}\sin\theta_A\cos\phi)^2 \\ &\quad +2A^2\cos\theta_{\mathrm{pol}}\sin\theta_{\mathrm{pol}}\cos\theta_{\mathrm{A}}\sin\theta_{\mathrm{A}}\cos\phi \end{aligned} \tag{3.13}$$

Eq. (3.13) expresses the intensity magnitude in the range of $-A/2$ to $A/2$. For convenience, above equation is rewritten to have a range of 0 to A.

$$\begin{aligned} I &= (A\cos\theta_{\mathrm{pol}}\cos\theta_{\mathrm{A}})^2 + (A\sin\theta_{\mathrm{pol}}\sin\theta_{\mathrm{A}})^2 \\ &\quad +2A^2\cos\theta_{\mathrm{pol}}\sin\theta_{\mathrm{pol}}\cos\theta_{\mathrm{A}}\sin\theta_{\mathrm{A}}\cos\phi \end{aligned} \tag{3.14}$$

Where ϕ is a function of retardation R and wavelength λ as given in Eq. (3.15).

$$R = \frac{\lambda\phi}{2\pi} \tag{3.15}$$

In Eqs. (3.14, 3.15), corresponding values for each variables are: $A = 1$, $\theta_{\mathrm{pol}}(°)$=decidable, and $\lambda(nm) = 633$. Therefore, the only variable that gives the retardation R (nm) is ϕ.

3.6 Near field pattern

NFP was taken by replacing the optical multimeter by a NFP camera (Hamamatsu Photonics K.K.). The measurement was done for both parallel and crossed Nicol configuration by setting θ_A in the direction of x_1 and x_3, respectively. Image from the camera was converted to one-dimensional numerical data using Lepas-11 control software (Hamamatsu Photonics K.K.).

NFP camera was set on the position shown in Figure 3.14. Fiber end was positioned at the focal point of the lens used. Intensity profile was obtained by the contrast between output and dark images.

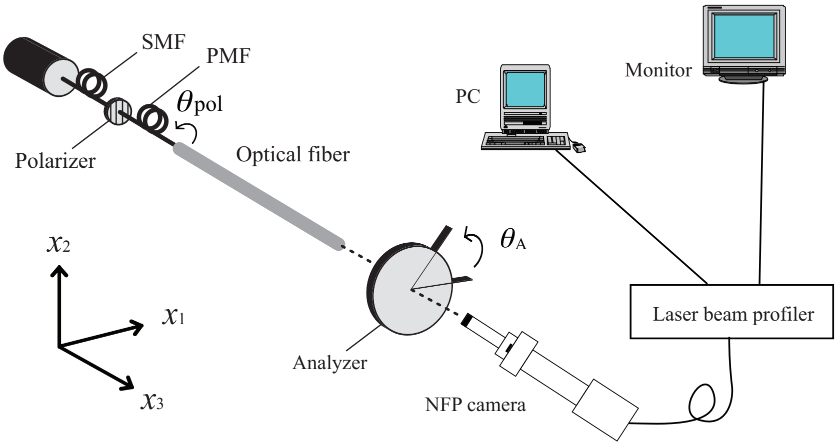

Figure 3.14: C5948 NFP optical system combined with polarizers (HAMAMATSU).

3.7 Conclusions

Fabrication and measurement procedures of the P(MMA/BzMA) POF were explained in this chapter. Materials, polymerization conditions, and heat drawing condition employed for the fiber fabrication were described in the first part of the chapter. Equipments and procedures used to measure refractive index and birefringence profile of the fiber core were explained. Variation of measurements used to characterize the polarization maintaining and phase retarding property of a MMF was explained at the end of the chapter.

Chapter 4

BASIC PROPERTIES OF THE P(MMA/BZMA)POF

4.1 Preface

The first half of this chapter discusses about the optimization of P(MMA/BzMA) (poly-methyl methacrylate/benzyl methacrylate copolymer) composition in the birefringence point of view, in which provides the most favorable property as a polarization-maintaining fiber. The latter half discusses about the basic transmission characteristics of the obtained P(MMA/BzMA) plastic optical fiber (POF), such as loss, bandwidth, and others.

4.2 Optimization of copolymer composition

Three P(MMA/BzMA)POFs were fabricated using the method as described in Section 3.2 with different copolymer compositions. Preforms were drawn to diameter of core/fiber = 667/1000 μm. Compositions of the test fibers are listed in Table 4.1.

Refractive index profiles of Fibers 1-3 are shown in Figure 4.1. Refractive indices of elimination compositions for orientational (82:18) and photoelastic (92:8) birefringence are obtained by the standard plot shown in Figure 3.3 (Section 3.3) and marked respectively in Figure 4.1 with broken

Table 4.1: Core composition of the test P(MMA/BzMA)POFs (before polymerization).

Fiber name	MMA/BzMA composition (wt%)
Fiber 1	77:23
Fiber 2	82:18
Fiber 3	87:13

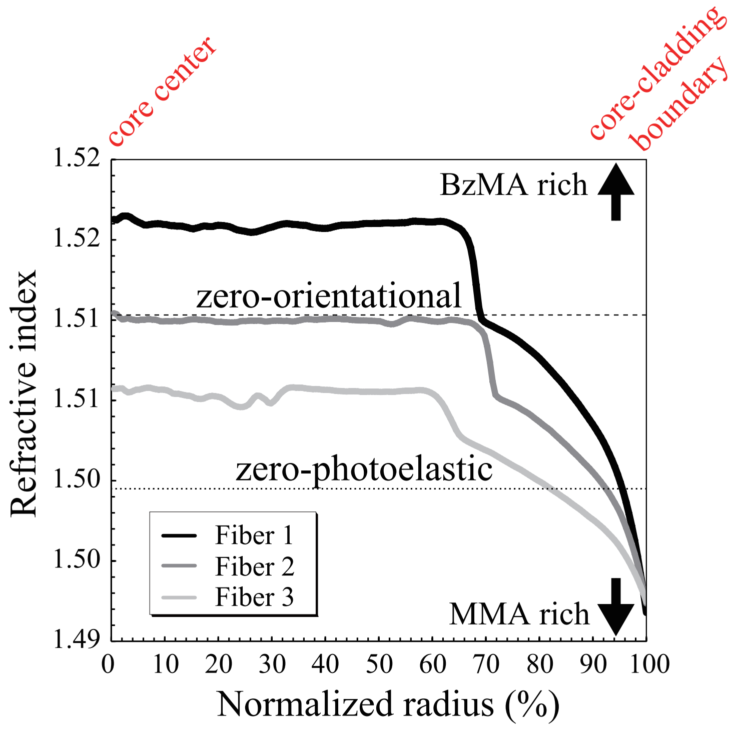

Figure 4.1: Measured refractive index profile of P(MMA/BzMA)POF core (solid line). The left and right axes are the refractive index and the corresponding P(MMA/BzMA) composition, respectively. P(MMA/BzMA) compositions for zero-orientational birefringence (82:18 wt%) and zero-photoelastic birefringence (92:8 wt%) are shown in broken lines. 0% and 1% of the normalized radius correspond to the guide center and core-cladding boundary, respectively. The fiber is considered to have an effective elimination of the orientational birefringence.

lines.

As a result, Fiber 2 has its dominant core region (from center to ≈70% of the core radius) matched well on the refractive index of zero-orientational birefringence.

Distribution of vertical birefringence of Fibers 1-3 are shown in Figure 4.2 in logarithmic scale. Although Fiber 1's refractive index profile was not necessarily matching well on the zero-orientational line in Figure 4.1, it had shown the distribution with lowest birefringence in Figure 4.2. In general, test fiber that contains more MMA had got higher birefringence.

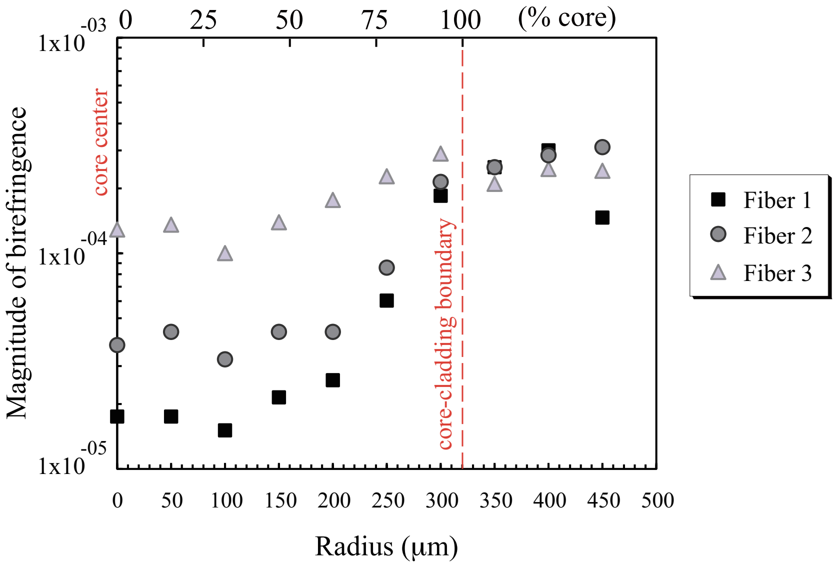

Figure 4.2: Distribution of vertical birefringence in test fiber cores.

4.3 Birefringence comparison between various types of MMFs

Figure 4.3 shows the polarized light microscopy images (using tint plate) of P(MMA/BzMA=82/18)POF, graded-index (GI)POF (molecule-doped)[8], and step-index (SI)POF (Mitsubishi Rayon, ESKA). Here, birefringence is larger as the color shifts from purple, blue, white, yellow, to orange.

The horizontal slices shown in Figure 4.3(a)(c)(e) have no birefringence throughout the cross section, while the vertical slices in Figure 4.3(b)(d)(f) exhibit significant amount of birefringence. This suggests that the polymer chains are aligned in the vertical direction either by the extrusion or the heat-drawing procedures.

Vertical views of P(MMA/BzMA)POF and GIPOF (Figure 4.3(b) and (d)) have gradual color change in the radius direction unlike the homogeneous distribution seen in the SIPOF (Figure 4.3(f)). In each photomicrograph, core diameter is marked in a solid line. Orientational birefringence in the P(MMA/BzMA)POF is observed significantly in its core edge to the cladding (Figure 4.3(b)). This result suggests that the heat-drawn fibers (P(MMA/BzMA)POF and GIPOF) are considered to have higher degree of polymer chain orientation in their core edge to the cladding than in their core center.

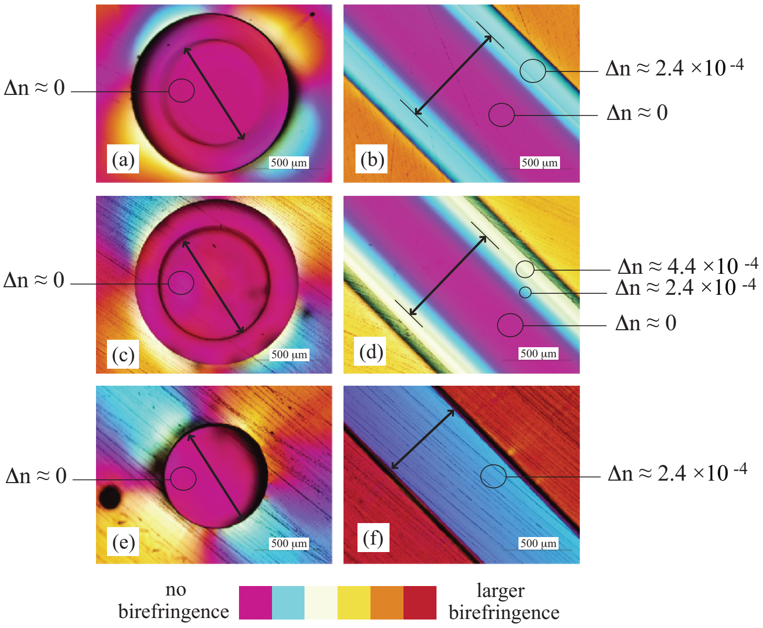

Figure 4.3: Photomicrographs of horizontal (left) and vertical (right) POF slices viewed by polarized optical microscope with sensitive tint plate insertion: (a)(b) P(MMA/BzMA)POF, (c)(d) GIPOF (molecule doped), and (e)(f) SIPOF. Core diameter is marked in solid arrow in each photomicrograph. The approximate birefringence values marked in the photomicrographs are obtained from color chart provided by Olympus.

Core edge of the P(MMA/BzMA)POF exhibits minor birefringence that is observed in blue, where the core edge of the GIPOF exhibits higher birefringence that is observed in both blue and white. This difference is suggested to be the effect of the copolymerization.

Birefringence of some other commercially available POFs were also measured using the Berek compensator with polarized optical microscope. Fibers were chosen to have variety in core diameters, materials, refractive index profile, and fabrication method.

Vertical birefringence at the core center of P(MMA/BzMA)POF, SIPOF, and PF(perfluorinated)-GIPOF (Chromis fiberoptics) are shown in Figure 4.4. For the P(MMA/BzMA)POF, birefringence distribution throughout the vertical cross section was measured as well. As a result, P(MMA/BzMA)POF exhibits very low birefringence compared to the other test fibers in the order of 10^{-1} to 10^{-2}. However, birefringence of the P(MMA/BzMA)POF increases from ≈75% position of the core radius.

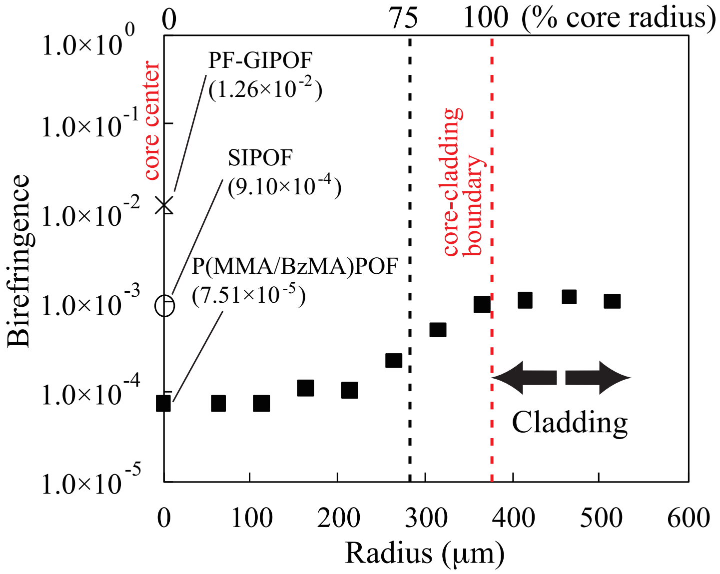

Figure 4.4: Logarithmic graph of vertical birefringence at the center of the test fibers (P(MMA/BzMA)POF, SIPOF, and PF-GIPOF) and radial birefringence distribution in the P(MMA/BzMA)POF.

4.4 Loss, bandwidth, and absorption spectrum of the P(MMA/BzMA)POF

Bandwidth, loss (at 650 nm), and absorption spectrum[1] of the P(MMA/BzMA)POF were compared to those of molecule-doped GIPOF and SIPOF. Fibers with similar core diameter were used. Bandwidth and loss measured at 650 nm is shown in Table 4.2. Absorption spectra of 450 to 800 nm region is shown in Figure 4.5. From these measurements, it is apparent that nothing notable was observed in terms of the basic transmission characteristics of the P(MMA/BzMA)POF, in which it is very ordinary compared to the other POFs.

---

[1] All three measurements were carried out referring to [92, 93].

Table 4.2: Transmission properties of the POFs (measured at 650 nm)

fiber	core/fiber diameter (μm)	bandwidth (50 m)	transmission loss (dB/km)
SIPOF	730/750	200 MHz	160
GIPOF	750/1125	1.49 GHz	172
P(MMA/BzMA)POF	750/1125	1.07 GHz	201

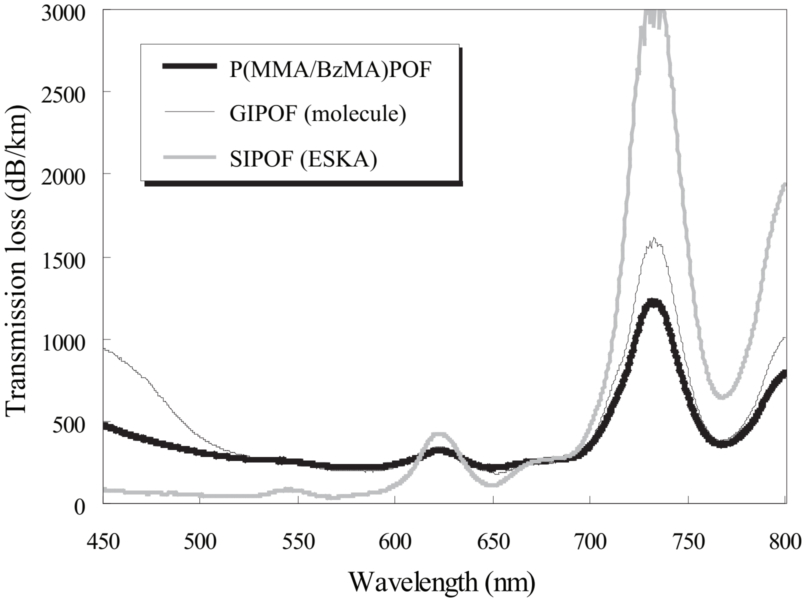

Figure 4.5: Spectral attenuation of the test fibers.

4.5 Conclusions

The optimum copolymer composition for eliminating orientational birefringence was suggested to be MMA:BzMA=82:18 (weight) in which the refractive index profile of Fiber 2 had shown a good match to the elimination composition of orientational birefringence than the other fibers fabricated in different copolymer compositions.

From the images of the polarized light microscopy, in any fiber type, horizontal birefringence was suggested to be negligibly low compared to the vertical birefringence. By comparing the vertical birefringence of P(MMA/BzMA=82/18)POF with other MMFs (Figures 4.3, 4.4), P(MMA/BzMA)POF had exhibited significantly low birefringence compared to the other test fibers in the order of 10^{-1} to 10^{-2}. However, birefringence of the P(MMA/BzMA)POF shifted higher from ≈75% of the core radius.

Loss, bandwidth, and spectrum of the P(MMA/BzMA)POF were similar compared to molecule-doped GIPOF and SIPOF. Measurement knowhow such as light source, detector, and light coupling conditions used in former POF researches were therefore suggested to be applicable in P(MMA/BzMA)POF measurements.

Chapter 5

MODAL ANALYSIS

5.1 Preface

This chapter deals only with the straightened fibers in order to clearly observe the intrinsic polarization-maintaining property of the modes, while the photoelastic effect is absent. In particular, extinction ratio (ER) measured at the offset launching and the local orientational birefringence are analyzed in a parallel manner. ER of mode group that corresponds to the local point of the core cross section was measured independently. Near field pattern (NFP) was used to help the discussion.

5.2 Modal dependence on extinction ratio

ER was measured using the point launching with 1 m test fiber straightened. Tested fibers (listed in Table 5.1) are: P(MMA/BzMA)POF[1], SIPOF[2] (Mitsubishi Rayon, ESKA), glass-based MMF[3], and PF-GIPOF[4] (Chromis Fiberoptics, Giga-POF). Fibers were chosen to have variety in core diameters, materials, refractive index profile, and fabrication method.

Figure 5.1(a) shows the intensity curve obtained from the test fibers (markers) at center launching (no offset). The solid line is intensity measured directly from the PMF without a following test fiber (blank)[5]. As a result, P(MMA/BzMA)POF shows a similar curve as the case of blank configuration, while the other MMFs do not show as high contrast between the maximum and the minimum intensity. Specific ERs obtained from the curves are: 14.0, 0.5, 1.5, 3.1, and 20.6 (dB) for

---

[1] poly-methyl methacrylate/benzyl methacrylate copolymer plastic optical fiber

[2] step-index plastic optical fiber

[3] multimode fiber

[4] perfluorinated graded-index plastic optical fiber

[5] Configuration when ”Optical fiber” is removed from Figure 3.8(b) (Section 3.5.2.1)

Table 5.1: Property of the test fibers

fiber	core/cladding diameter (μm)	refractive index profile	fabrication method
P(MMA/BzMA)POF	750/1125	graded	preform drawing
SIPOF	730/750	step	extrusion
glass-based MMF	50/125	graded	preform drawing
PF-GIPOF	50/490	graded	extrusion

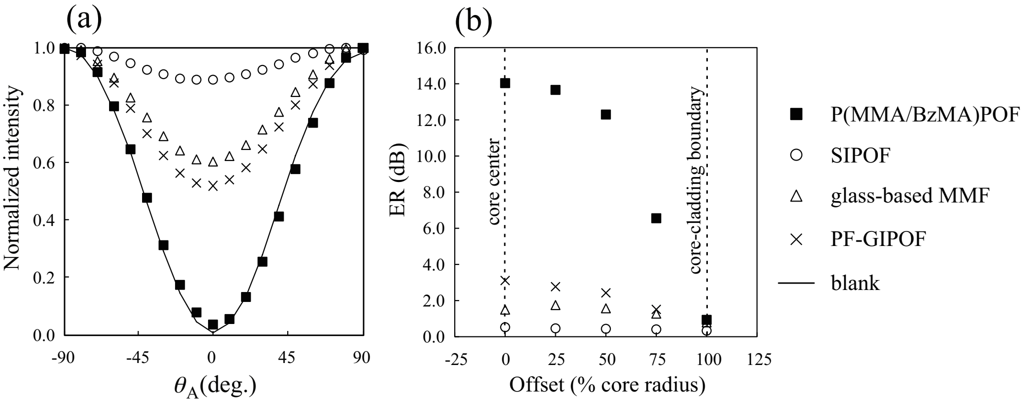

Figure 5.1: (a) Normalized intensity for a 180° rotation of θ_A at a propagation of 1 m straight test fiber (wavelength= 633 nm): the markers (square, circle, triangle, and cross) represent data obtained by center launching of the test fibers (P(MMA/BzMA)POF, SIPOF, glass-based MMF, and PF-GIPOF, respectively). The solid curve is obtained at a blank configuration measured by removing the test fiber in between the PMF and the analyzer. (b) ER obtained by launching different offset points at the core.

P(MMA/BzMA)POF, SIPOF, glass-based MMF, PF-GIPOF, and the blank configuration, respectively.

Figure 5.1 (b) shows the ER shifting while the lateral offset is created from the core center (0%) to the core-cladding boundary (100%). Although P(MMA/BzMA)POF has ER of 14.0 dB at the center launching, the value drastically decreases to 6.6 dB at 75% offset. At 100% offset launch, ER is low as the other test fibers.

5.3 *NFP at offset launching*

Figure 5.2 shows the one-dimensional NFP of the output light from the P(MMA/BzMA)POF. Here, all intensity values were normalized by the maximum obtained from the 0% parallel Nicol intensity profile that is shown in Figure 5.2(a) with solid line. Profiles are similar in the cases of 0, 25, and 50% offset. In these three offset cases, the parallel Nicol pattern has the maximum at the center, and the field radius distributes in the range of ± 290 to ± 310 μm. However, the profile becomes flatter and wider (approximately ± 340 μm) at the 75% offset launch.

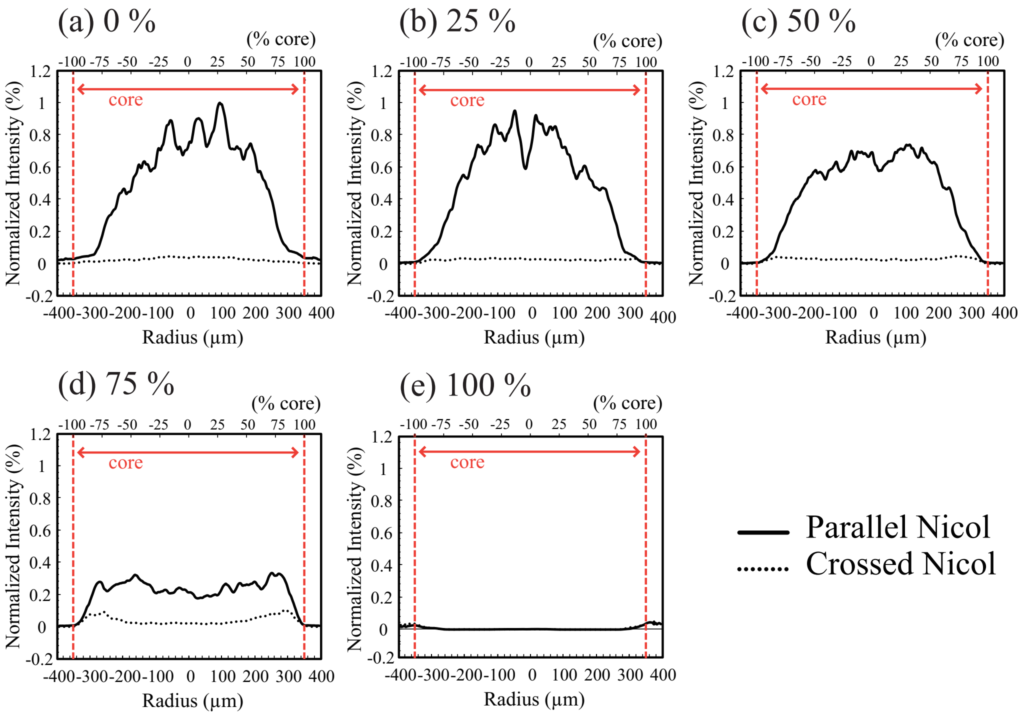

Figure 5.2: One-dimensional NFP of the P(MMA/BzMA)POF at parallel and crossed Nicol configurations in offset launching of: (a) 0%, (b) 25%, (c) 50%, (d) 75%, and (e) 100% of the core radius. All intensity values were normalized by the maximum obtained from the 0% parallel Nicol data. Solid and broken lines represent when the light from the PMF and the analyzer configures parallel and crossed Nicol, respectively.

5.4 Discussion

In addition to the data obtained from the ER and NFP measurements, mode-dependent polarization maintaining property needs to involve the result of birefringence measurement as well.

In the radial distribution of the vertical birefringence shown in Figure 4.4 (Section 4.3), when comparing the core center, P(MMA/BzMA)POF exhibits very low birefringence compared to the other test fibers in the order of 10^{-1} to 10^{-2}. However, it is also noted that the birefringence of P(MMA/BzMA)POF increases in at the 75% position of the core radius.

From the radial distribution of the oriental birefringence (Figure 4.4), the NFP (Figure 5.2), and the point-launched ER (Figure 5.1), changes are observed commonly at the 75% radius point of the P(MMA/BzMA)POF. Drastic ER decrement at this point is therefore considered to be the result of predominant light propagation at the core edge that has the higher birefringence than in the core center. ERs measured at the center-launching of the PF-GIPOF and the SIPOF were not high as the value obtained from P(MMA/BzMA)POF, where the birefringence at the center of these fibers show significantly high value compared to the P(MMA/BzMA)POF. The above cases suggest that the vertical birefringence of the launching point has a strong correlation to the ER.

Because ER measured from the straightened fiber is considered to have no photoelastic birefringence, it therefore should be affected only by the fiber's orientational birefringence and the waveguiding manner. The reason in which the SIPOF has shown the lowest ER (Figure 5.1) is explained as follows. Due to the reflection-based waveguiding, light coupled to the SIPOF core at a certain angle to the guide axis experiences refractive index anisotropy[6]. The initial polarization state is therefore disturbed. Repeated total reflection at cylindrical interface also disturbs the input polarization. Hence, the SIPOF output is considered to be practically randomly polarized at even 1 m propagation. Above model may explain why the GI fibers in general have higher ER than the SI fiber.

When explaining the polarization-maintaining mechanism of the P(MMA/BzMA)POF, it is

---

[6] As shown in Figure 4.3(f), SIPOF has birefringence in the guide axis direction. Only the ray oscillating parallel or perpendicular to this direction is safe from experiencing this refractive index anisotropy. Thus, all the coupled light except for the lowest order mode experiences birefringence.

noted that the NFP profiles of 0 to 75% offset is similar to E-field distribution of the LP_{01} mode (compare Figure 5.2(a-c) and Figure 2.3, 2.4 in Section 2.3.3). Since the angle of the input is same among each offset[7], similar mode distribution at each offset should have been obtained[8]. Although these NFPs are also similar to the Gaussian beam profile (now compare Figure 5.2(a-c) and Figure 2.6 in Section 2.6), the actual case is considered to be clearly different from the propagation in the homogeneous medium. Figure 5.3 illustrates the two models of LP_{01} mode and Gaussian beam. The obvious reason that do not support the Gaussian beam model (homogeneous medium model) seen from the laboratory measurement is that the intensity peak position do not move while creating the offset. In addition, the beam diameter at 1 m position should totally be larger when the laser beam was released in the air. However, both models could coincide when considering the core diameter of P(MMA/BzMA)POF.

Figure 5.4 shows the speckle pattern[9] of a 50 μm-core glass-based MMF and a 750 μm-core GIPOF. The speckles in the glass-based MMF has radial variation, in which more speckles exist in the center part. On the other hand, radial distribution is hardly seen in the GIPOF image while the speckles themselves are observed fairly clear. One notable thing is that the speckle of Gaussian beam tend to be coarser than the fiber speckles at the same length of propagation. Degree of speckle coarseness is said to be similar among the two fibers, which both actually have fine speckles. Hence, this statement also conflicts with the homogeneous medium model.

From the above discussion, a fair reason of why high ER can be obtained in a large spot diameter using the P(MMA/BzMA)POF is: (1) dominant power is delivered into LP_{01} at non-angular launching within 75% diameter offset, and (2) breakage of LP_{01} degeneration hardly occurs because of the reduced birefringence.

---

[7] Launching angle: always parallel to the guide axis, i.e., PMF in Figure 3.8(b) is stuck perpendicular to the core cross section of the MMF.

[8] Refer Section 2.2.3 for an explanation about the relationship between input angle and the mode.

[9] intensity distribution seen across a MMF's cross section, interference pattern of modes.

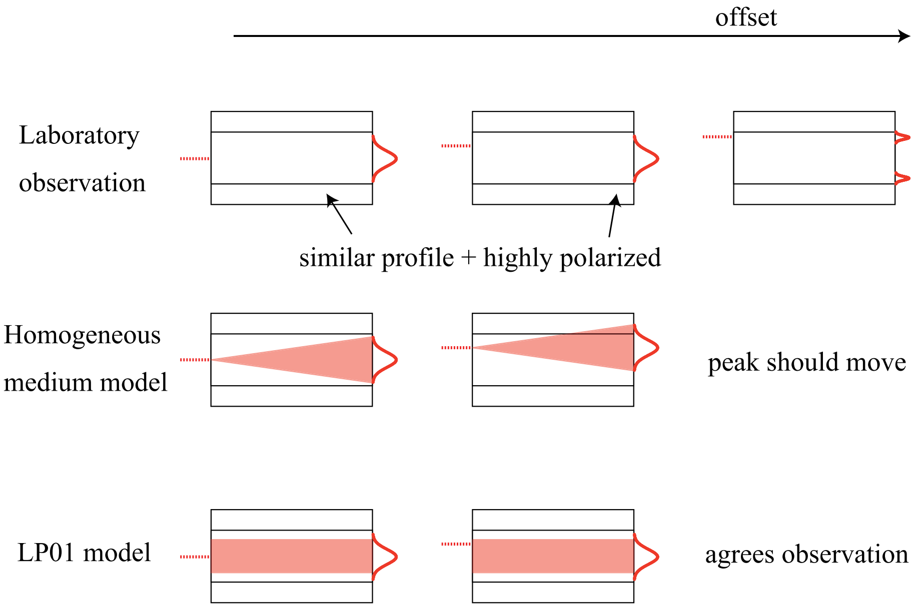

Figure 5.3: Schematic diagrams of laboratory observation (top) and the two models of Gaussian beam (middle) and LP_{01} mode (bottom).

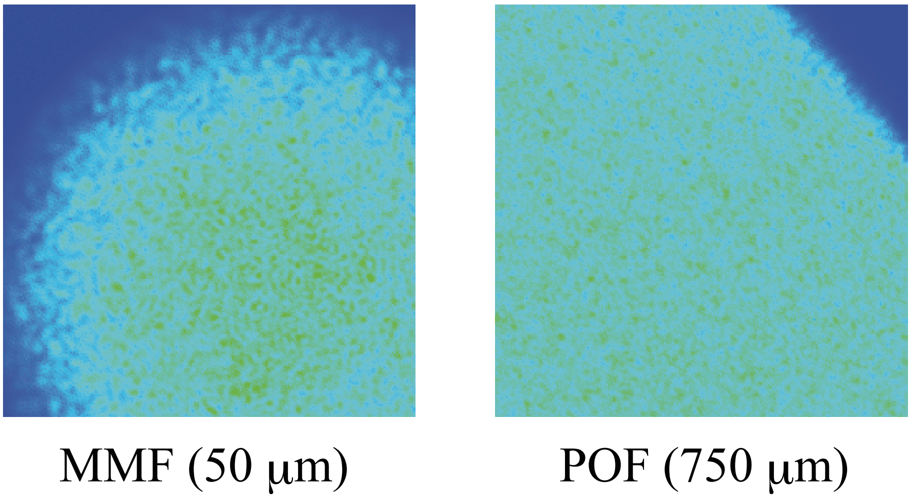

Figure 5.4: Speckle patterns of a 50 μm-core glass-based MMF and a 750 μm-core GIPOF. Images were taken by the NFP camera.

5.5 Conclusions

At the purpose to clarify the contribution of birefringence reduction to the enhancement of polarization-maintaining property of a MMF, ER measurement at offset launching was performed. As a result, drastically high ER was obtained from the P(MMA/BzMA)POF compared the other MMFs. An inverse relationship between birefringence magnitude and ER was observed as well. NFP had provided an evidence of spacial distribution where the light had been propagating down. Polarization-maintaining property of the P(MMA/BzMA)POF was discussed based on the two models of homogeneous medium model and LP_{01} mode model. As the result, reduced birefringence is suggested to be avoiding the breakage of LP_{01} degeneracy, where the actual case was considered to be somewhat different from the Gaussian beam propagation.

Chapter 6

BENDING ANALYSIS

6.1 Preface

This chapter discusses about the phase shift that is induced by the photoelastic birefringence originating from fiber macrobending. Figure 6.1 shows the polarized light microscopy images of the straightened and the bent P(MMA/BzMA)POF[1] cross sections. As shown in Figure 6.1(a), the straightened fiber has a symmetrical distribution of birefringence, which is lowest around the core center and higher at the cladding in both right and left sides of the guiding axis. On the other hand, the bent fiber has its birefringence unsymmetrically distributing depending whether on the inner or outer side of the curvature. Magnitude of photoelastic birefringence depends on the local MMA/BzMA composition. As seen in the two photomicrographs, the core edge of the inner side of the curvature that originally had blue coloration is changing to purple after the bending while dominant part of the core is experiencing increase in birefringence. It is therefore apparent that the birefringence does not necessarily increase after the bending. In the case of P(MMA/BzMA), it depends on the point where the copolymer composition lies between the elimination compositions of the two types of birefringence[2] in addition to the original birefringence as a result of internal stress and molecular orientation. Mueller calculus[3] is a well-known tool that is capable in predicting polarization state using such initial and external birefringence changes. In this aspect, the stance of the laboratory measurements performed here is the basis preparation for quantifying the behaviors of the birefringence change in P(MMA/BzMA)POF and other multimode fibers (MMFs).

Setup shown in Figure 3.9(b) (Section 3.5.3) was used. Since macrobending loop(s) are created along the x_1-x_3 plane, optical axes of the fiber should be x_1 and x_2. Both pinhole and PMF launching

---

[1] poly-methyl methacrylate/benzyl methacrylate copolymer plastic optical fiber

[2] Elimination compositions of two types of birefringence: orientational (MMA:BzMA=82:18), photoelastic (92:8).

[3] Mueller calculus: calculation of Stokes vector

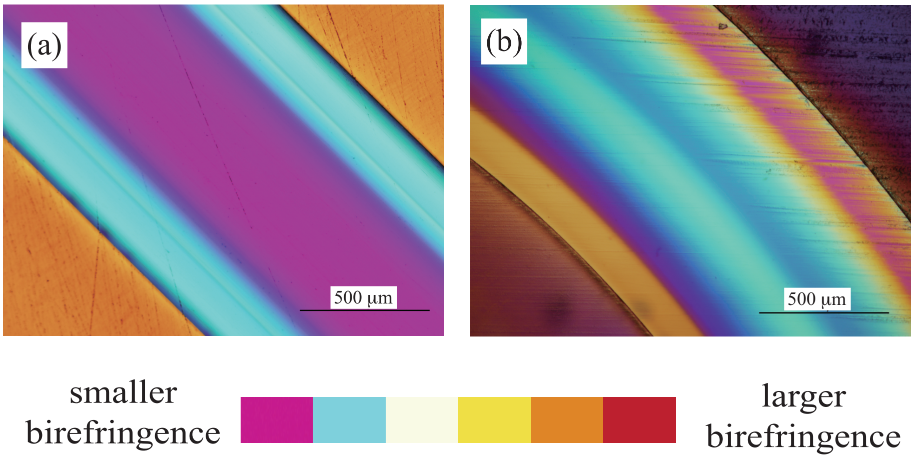

Figure 6.1: Photomicrographs of the P(MMA/BzMA)POF slices viewed by polarized optical microscope with sensitive tint plate insertion: (a) straightened, (b) bent. Amount of the birefringence that corresponds to each color is shown in the color bar in the bottom.

were used (Figure 3.8, Section 3.5.2). Based on this hypothesis, extinction ratio (ER) was measured at variation of θ_{pol}[4]. Amount of retardation was estimated using quarter wave plate (QWP)[5] and an analysis using calculation[6].

6.2 *Macrobending conditions*

First, ER measurement was performed at the pinhole-macrobending setup with different bending conditions. Fiber loop(s) were created on bending rods that varies in diameter, namely, 10 cm (rod)×1 (loop), 5 cm×2, and 3 cm×3. ERs at three input angles ($\theta_{\mathrm{pol}} = 0, 45, 90°$) were measured for straightened/bent fibers. Tested fibers were: P(MMA/BzMA)POF, SIPOF[7] (Mitsubishi Rayon, ESKA), and GIPOF[8] (molecule-doped). Fiber length was 1 m.

---

[4] θ_{pol}: Angle between vibration plane of the input light and the bending (x_1-x_3) plane. Refer Section 3.5.2 for detail.

[5] Refer Section 3.5.4.1 for the detail explanation of the usage of QWP.

[6] Refer Section 3.5.5 for the detail of calculation

[7] step-index plastic optical fiber

[8] graded-index plastic optical fiber

Results are shown in Figure 6.2(a)(c)(e). As shown in Figure 6.2(a), ER at $\theta_{\mathrm{pol}} = 45°$ is lower than the case of $\theta_{\mathrm{pol}} = 0$ and 90° when the P(MMA/BzMA)POF is under the macrobending, while there is no θ_{pol} dependence in ER measured when the fiber is straightened. GIPOF (Figure 6.2(c)) and SIPOF (Figure 6.2(e)) do not have such θ_{pol} dependence throughout all bending conditions.

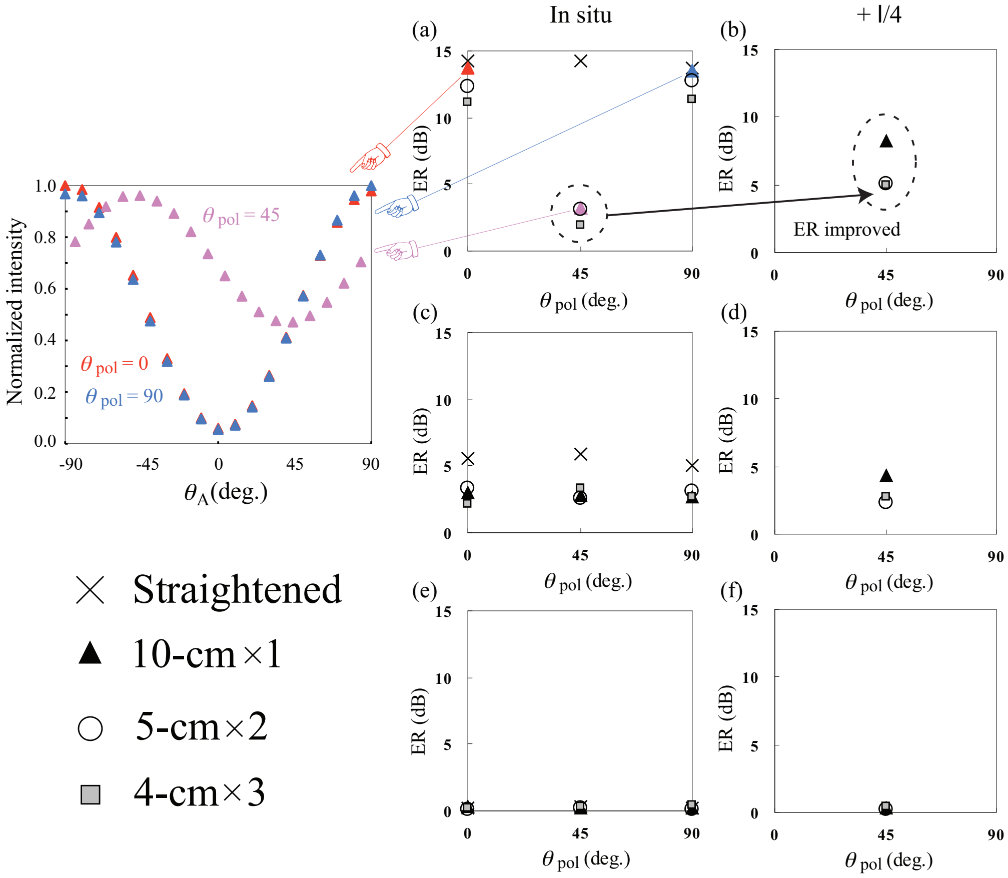

Figure 6.2: ER obtained at each input polarization angles of $\theta_{\mathrm{pol}} = 0, 45, 90$: (a) P(MMA/BzMA)POF in situ, (b) P(MMA/BzMA)POF QWP, (c) GIPOF in situ, (d) GIPOF QWP, (e) SIPOF in situ, and (f) SIPOF QWP. In situ is the data obtained before inserting a QWP. ”QWP” is the data obtained after inserting a QWP in the condition of $\theta_{\mathrm{pol}} = 45$ and $\theta_{\mathrm{QWP}} = 0$. Crosses, filled triangles, open circles, and gray squares are the data obtained from different macrobending conditions; which are straight, one loop on 10 cm, two loops on 5 cm, and three loops on 4 cm, respectively. As highlighted in broken ovals, ER improvement of P(MMA/BzMA)POF at $\theta_{\mathrm{pol}} = 45°$ after QWP insertion suggests that the macrobending acts to induce retardation in the P(MMA/BzMA)POF, which the improved ERs are consequence to the compensated retardation.

ER measured at $\theta_{\text{pol}} = 45°$ after QWP insertion is shown in Figure 6.2(b)(d)(f). ER measured from the P(MMA/BzMA)POF had improved by inserting the QWP as shown in Figure 6.2(b). Minor ER improvement is seen in the GIPOF under 10-cm×1 macrobending (Figure 6.2(d)), and no improvement is seen for all conditions in the SIPOF (Figure 6.2(f)).

Intensity curves corresponding to the plots at $\theta_{\text{pol}} = 45°$ are shown in Figure 6.3. Here, the curves in open and filled squares are measured data for each before (in situ) and after inserting the QWP ($+\lambda/4$). Retardation in the P(MMA/BzMA)POF waveguiding is obtained by fitting Eq. 3.14 (Section 3.5.5) to each in situ curve with an optimum R (nm) (Figure 6.3: broken lines). Next,

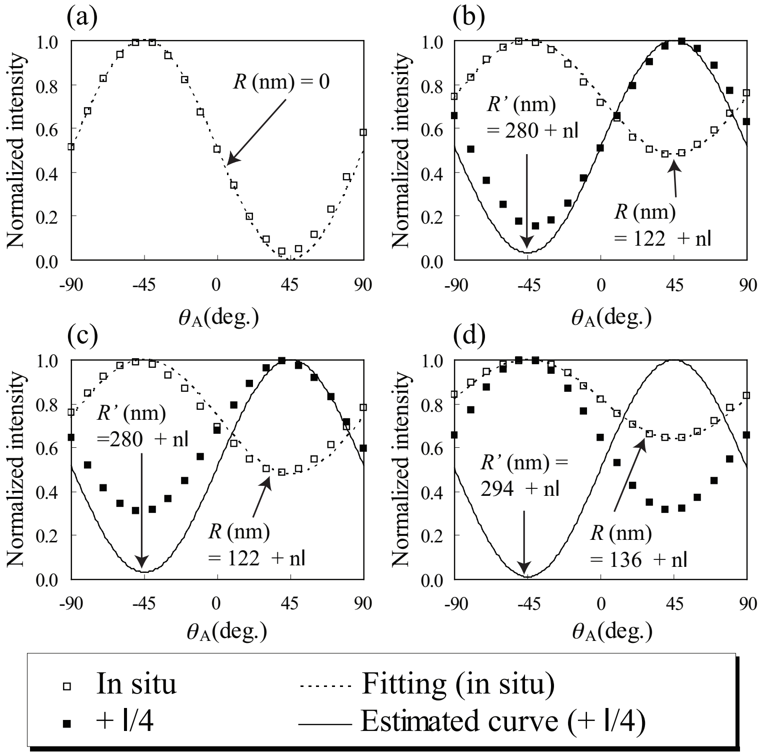

Figure 6.3: Intensity curve measured from 1 m P(MMA/BzMA)POF transmission for different macrobending conditions ($\theta_{\text{pol}} = 45°$, $-90° < \theta_A < 90°$): (a) straight, (b) 10-cm×1, (c) 5-cm×2, and (d) 4-cm×3. Open squares are measured curves without a QWP in the setup. Broken lines are numerical curves fitted on open square curves. Filled squares are measured curves in Figure 3.7 apparatus at $\theta_{\text{QWP}} = 0°$. Solid lines are numerical curve of the estimated retardation after adding $\lambda/4$ to the obtained retardation values for in situ measurements.

Table 6.1: In situ and predicted retardation at $\theta_{\text{pol}} = 45°$ P(MMA/BzMA)POF waveguiding for different macrobending conditions. (R and R' are the in situ retardation and the predicted retardation after passing a QWP, respectively. λ is 633 (nm) and n is a positive integer.)

bending condition	R (nm)	R' (nm)
straight	0	N/A
10 mm × 1	122+nλ	280.2+nλ
5 mm × 2	122+nλ	280.2+nλ
4 mm × 3	136+nλ	294.2+nλ

158 nm retardation (quarter of the laser wavelength) is added to each R, which is the predicted retardation after the QWP insertion (R'). Table 6.1 shows R and R' values for all macrobending conditions. The curves corresponding each R' are shown in solid lines in Figure 6.3.

As a result, a fairly good match between R' and the measurement is obtained for the loosest bending condition (10-cm×1) as shown in Figure 6.3. However, prediction does not meet very well for the other two bending conditions. The harshest macrobending condition (4-cm×3) has its measurement curve even farther to the prediction than the case of 5-cm×2. This result suggests that the retardation generated by the bent P(MMA/BzMA)POF is intermodal. In the harsher macrobending condition, photoelastic birefringence exhibits at higher contrast in the fiber, whereas a consequence, retardation becomes greater between the guided modes that the ER can no longer be restored using the QWP.

6.3 Mode-selective measurement of extinction ratio under macrobending

Next, mode-selective measurement was performed for straightened and bent P(MMA/BzMA)POFs. ERs obtained by the point launching at the condition of $\theta_{\text{pol}} = 45°$ are shown in Figure 6.4(a)(b), respectively. When the fiber is straightened, the ER gradually decreases from 14 to 1 dB from the core center (0%) to the core-cladding boundary (100%) ((a) filled circles), i.e., the ER shows an offset dependence. However, ER measured using the QWP is more consistent ((a) open circles).

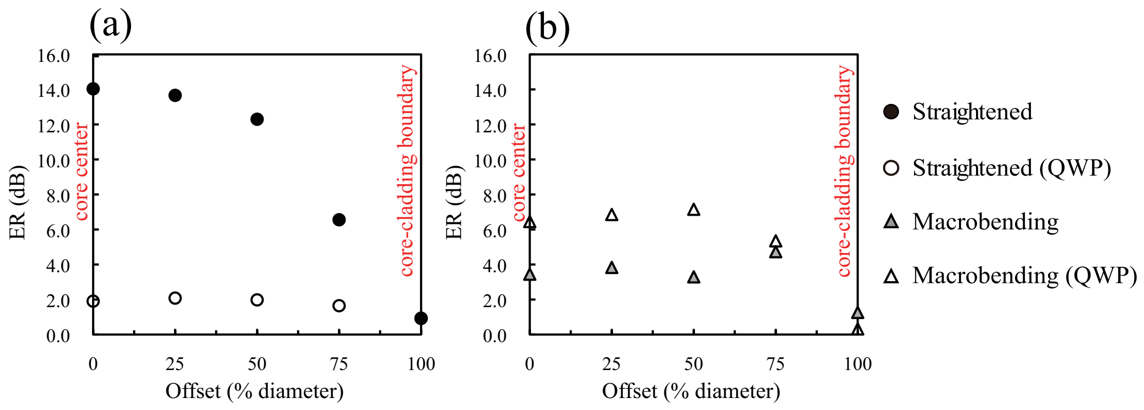

Figure 6.4: ER obtained by point-launching different offset points in the P(MMA/BzMA)POF core at $\theta_{\mathrm{pol}} = 45°$: (a) straightened, (b) macrobending. Filled circle, open circle, filled triangle, and open triangle markers represent data obtained for the cases: straightened, straightened+QWP, bent, and bent+QWP, respectively.

When the fiber is at the macrobending, ER value is consistent until 75% offset ((b) filled triangles). The restored ERs obtained using the QWP are consistent among all the offsets as well ((b) open triangles).

Intensity curves obtained at $\theta_{\mathrm{pol}} = 45°$ for different point-launching offsets are shown in Figure 6.5. Retardation values obtained by the fitting are shown in Table 6.2. When the fiber is straightened, the curve measured without the QWP insertion loses initial contrast when the offset is larger, whereas the curves measured with the QWP are all similar among all the offsets (Figure 6.5(a)). The corresponding retardations (R, R_{QWP}) appear in a similar manner as shown in Table 6.2. R increases as the offset increases (38 to 88 nm), but R_{QWP} values are similar among all the offsets, which are ranging within 135 to 140 nm. Difference between the prediction (R+158) and the measurement (R_{QWP}) are therefore inconsistent among the offsets. When the fiber is at the macrobending, curves for both before and after the QWP insertion are similar among all offsets (Figure 6.5(b)). Similarly, both R, R_{QWP} for the bent cases are relatively consistent among all the offsets. The mismatch between R+158 and R_{QWP} is larger at the straightened cases than the bent cases.

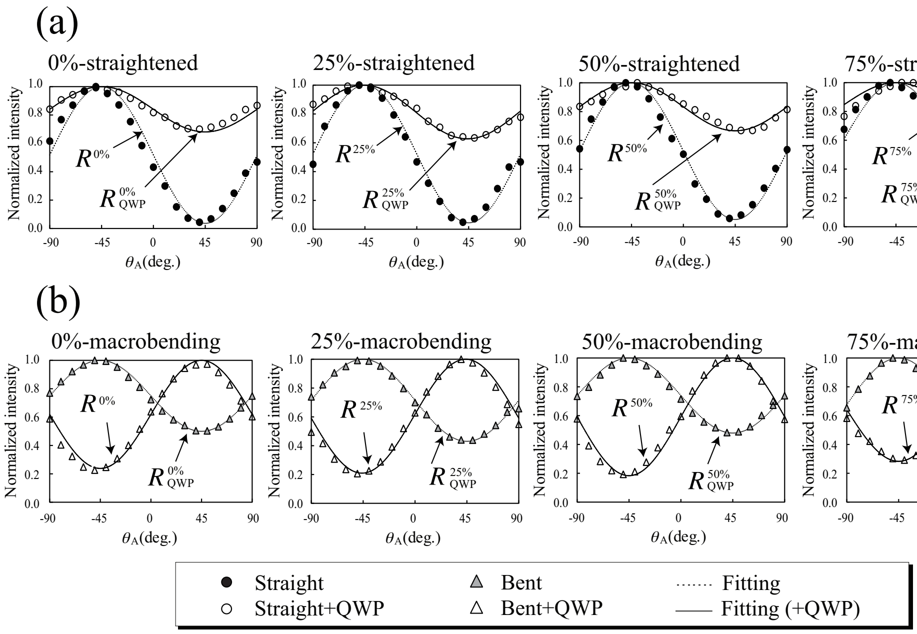

Figure 6.5: Intensity curves measured from 1 m P(MMA/BzMA)POF ($\theta_{\rm pol}$ = 45°, $-90° < \theta_A < 90°$) at point-launching offsets of 0, 25, 50, 75% when the fiber was (a) straightened and (b) at macrobending. Broken and solid lines are numerical curves (Eq. 3.14) fitted respectively on filled and open triangles in order to obtain retardations, R and $R_{\rm QWP}$, for each offset conditions.

Table 6.2: Retardation of the P(MMA/BzMA)POF at $\theta_{\rm pol}$ = 45° at different launching offset positions for the cases of straightened and at the macrobending. R and $R_{\rm QWP}$ are the retardation obtained from the intensity curves before and after the QWP insertion, respectively. R+158 is a predicted retardation calculated by adding $1/\lambda$ to R.

Retardation (nm)	Straightened	Macrobending
$R^{0\%}$, $R^{0\%}_{\rm QWP}$ ($R^{0\%}$+158)	38, 139 (196)	124, 225 (282)
$R^{25\%}$, $R^{25\%}_{\rm QWP}$ ($R^{25\%}$+158)	42, 135 (200)	117, 230 (275)
$R^{50\%}$, $R^{50\%}_{\rm QWP}$ ($R^{50\%}$+158)	45, 138 (203)	122, 235 (280)
$R^{75\%}$, $R^{75\%}_{\rm QWP}$ ($R^{75\%}$+158)	88, 140 (246)	108, 218 (266)

6.4 Fiber length dependence

Figure 6.6 shows ER at different fiber length that was measured by cutback starting from 20 m. P(MMA/BzMA)POF, SIPOF, and GIPOF were tested. At the long fiber length, fiber was bent in arbitrary loops in about 30 cm diameter. Therefore, the test includes the effect of photoelastic birefringence, but at a natural bend.

At fiber lengths 1 m and shorter, ER measured from P(MMA/BzMA)POF ranges in 9.0-10.3 dB. ER measured at 5 m (4.4 dB) and 10 m (3.7 dB) denotes that the P(MMA/BzMA)POF still has the polarization maintaining property at 10 m propagation. At 20 m, it is no longer considered to have that function (0.8 dB at 20 m). Despite the higher ER measured from the GIPOF than the SIPOF at lengths 1 m and shorter, they are both below 0.5 dB after 5 m propagation; thus, these two fibers practically have no polarization maintaining property after 5 m propagation.

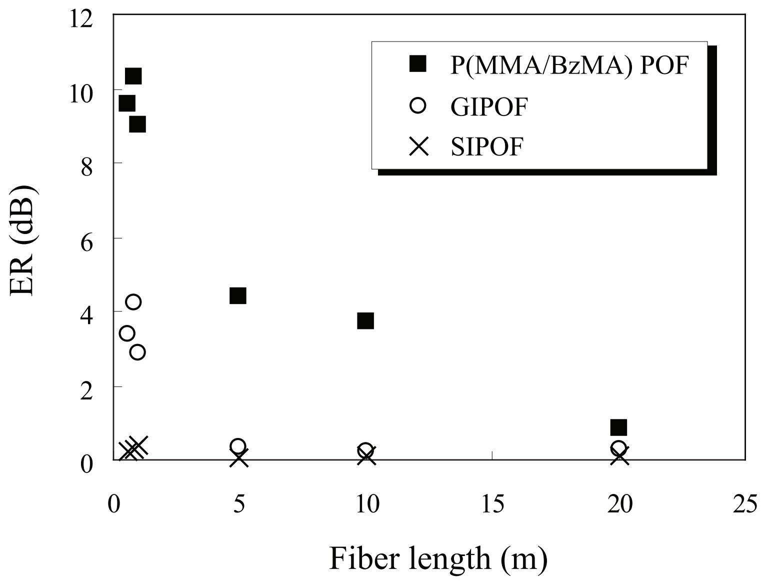

Figure 6.6: Extinction ratio of the POFs at different operating length.

6.5 Discussion

The greater ER measured from the straightened P(MMA/BzMA)POF compared to the straightened GIPOF is suggested to be the effect of the lower orientational birefringence in the P(MMA/BzMA)POF core edge (Figure 4.3(b)(d)). Input angle dependence seen in the ER data measured from the bent P(MMA/BzMA)POF is not seen in the cases for the other two POFs (Figure 6.2). For the bent P(MMA/BzMA)POF, similar ERs measured at horizontal ($\theta_{\mathrm{pol}} = 0$) and vertical ($\theta_{\mathrm{pol}} = 90°$) inputs allow us to characterize its macroscopic refractive index anisotropy, which is described in a representation ellipsoid that has x_1 and x_2 in Figure 3.7 as its principal (optical) axes. Degraded ER at $\theta_{\mathrm{pol}} = 45°$ and its improvement after the QWP insertion also support the existence of these principal axes. This result suggests that the macrobending acts to induce retardation by the local photoelastic birefringence in the P(MMA/BzMA)POF, hence, the restored ERs are the consequence of the added quarter-wavelength retardation, which the QWP improves ER when the retardation of an incident light is less than 158 nm. The retardation generated by the propagation through the bent P(MMA/BzMA)POF is suggested to be the consequence of refractive index difference of the two principal axes, where an incident light oriented in 45° to the principal axes will split to each components and propagate in respective speeds. When the P(MMA/BzMA)POF is straightened, the representation ellipsoid is considered to be a sphere (i.e., isotropic refractive index) as the ER is not dependent to the θ_{pol} (Figure 6.2(a)). The absence in such input angle dependence for the SIPOF is understandable if its output is randomly polarized, which agrees the earlier discussion on the straightened SIPOF as well. For the GIPOF, from the slight ER improvement observed at the loosest macrobending condition (Figure 6.2(d)), polarization state of the guided light in the GIPOF is suggested to be regulated better than in the SIPOF, but not as excellently as in the P(MMA/BzMA)POF.

From the fitting of the P(MMA/BzMA)POF curves, a fairly good match between R' and the measurement is obtained for the loosest bending condition (10-cm×1) as shown in Figure 6.3. However, prediction does not meet very well for the other two bending conditions. The harshest macrobending condition (4-cm×3) has its measurement curve even farther to the prediction than the case of 5-cm×2. This result suggests that the retardation generated by the bent P(MMA/BzMA)POF is intermodal. In the harsher macrobending condition, photoelastic birefringence exhibits at higher contrast in the fiber, whereas a consequence, retardation becomes greater between the guided modes that the ER can no longer be restored using the QWP.

When launched different points of the P(MMA/BzMA)POF core, the ER decrease observed in the straightened fiber (Figure 6.4(a) filled circle) has an inverse relation to the magnitude of orientational birefringence (Figure 4.4, Section 4.3), which agrees the observation in the previous section that the core center (0%) shows the lowest orientational birefringence and the ER obtained by launching that point is the highest. Similarly, the other measurement points also show such inverse relationship among the orientational birefringence and the ER. ERs measured after the QWP insertion are similar at all offsets. This result suggests that the accumulated effect of the orientational birefringence in each optical path of the mode is observed in the ER values. For example, the modes launched at the core edge exhibit low ER, because its optical path distributes to the region with high orientational birefringence. On the other hand, the modes launched within the core central region exhibit high ER, because it propagates the region with low orientational birefringence. The ER degraded by the influence of the orientational birefringence do not restores by using the QWP; thus, the output is considered to be partially randomized in such cases. Since the light propagates in a multimode graded-index fiber by refraction, the angle of the optical path changes frequently. Thus, the orientational birefringence influences the light in a different manner at each point, so the polarization of the output light is practically randomized. This principle also explains the lack of correlation between measured and predicted retardations of the straightened fiber (R_{QWP} and R+158 in Table 6.2, respectively). On the other hand, ER measured at the macrobending do not have a notable dependence to the amount of offset (Figure 6.4(d)). Both before and after the QWP insertion, ER values are similar among offsets 0 to 75%. The retardation values obtained from their intensity curves are similar as well (Table 6.2). ER measured at 100% offset is practically zero, which is explained by the high orientational birefringence in this region (Figure 4.4). The above results suggest that the photoelastic birefringence in each local point of the core is similar in the employed bending condition. Therefore, the effect of photoelastic birefringence to the ER is suggested to be less-dependent on the launched modes than that of orientational birefringence.

From the discussion of earlier chapter, Figure 6.4 is said to be showing the splitting manner of LP_{01} into LP_{01}^{x1} and LP_{01}^{x2}. Phase difference and the generation of optical axis agrees the LP_{01} model as well. This statement agrees with the mode coupling and bending investigation of POFs by Ishiyama *et al*[94].

At the longer fiber length, P(MMA/BzMA)POF still exhibits the polarization maintaining property at 10 m, but not at 20 m. The GIPOF completely loses the polarization maintaining property at 5 m, and the SIPOF has none at 0.6 m. Because the affection of photoelastic birefringence is minimized in the cutback measurement (fiber was either straight, or weakly bent), the observed ER degradation is considered to be largely resulting from the longer distance propagation.

6.6 Conclusions

ER measurement combined with macrobending was performed at the purpose to observe the optical axis in MMFs. As a result, optical axis was clearly observed in the P(MMA/BzMA)POF, which was the only MMF that shows a regular phase shifting behavior. Quantification of retardation was fairly successful using QWP and fitting, which is expected to be applicable for numerical expressions and calculations using Stokes vector notation. The offset launching measurement had suggested that the breakage of LP_{01} degeneracy is creating the optical axes when bent.

Chapter 7

PRESSURE SENSOR FABRICATION

7.1 Preface

As already explained in Chapter 1, fiber optic (FO) pressure sensor is one of the famous application of optical fibers. Table 1.2 (Section 1.5.8) summarizes known FO pressure sensors that have been proposed using silica-based fibers. From this table, it is noted that the extrinsic sensors[1] are mainly using multimode fibers (MMFs) with DC light, whereas the intrinsic sensors[2] are mainly using singlemode polarization-maintaining fibers (SM-PMFs). Recently, structural monitoring using FO sensors is attracting attention, because of its smart design that uses full benefit of the optical fiber's characteristics[95, 36, 47, 48]. In detail, such FO sensors use reflection and pulse modulation to provide both pressure and spatial information. For this unique application of optical fiber, intrinsic sensor structure is a requirement.

Both extrinsic and intrinsic sensors that use glass-based optical fibers have been developed for years; thus, those models that are available in the market have satisfactory sensitivity for each sensor purpose. As already noted in the first chapter, FO sensors vary widely in their material and composition in which each offering different value propositions on sensitivity, dynamic range, size, shape, and etc. By viewing Table 1.2, it is apparent that the extrinsic FO sensors have concerns regarding laser/detector linearity, while the intrinsic FO sensors tend to have concerns with temperature affection. Those problems may be taken care by modifying the electric circuit or wrapping up the fiber with highly insulating (in terms of heat) jacket, but those procedures conflicts with the cost performance. Hence, the essential point at developing a FO sensor is to have a smart application so that the effort for compensating the disadvantages could be minimized.

---

[1] Extrinsic sensor: type of FO sensor that has the fiber just for light delivery and collection.

[2] Intrinsic sensor: type of FO sensor that has the fiber itself acts as the sensing medium

To the recent popularity of plastic optical fiber (POF) sensors, POFs have smart applications that cannot be done using the glass optical fibers[50, 51, 49, 52, 54, 56, 60, 61, 50]. Biomedical use such as structural monitoring of organs, implanted body parts, proportion, and etc is considered to be a suitable applications of the POF sensor[52, 53]. This is because of the elasticity of POFs compared to the glass fibers that is brittle and likely to make wounds when broke. In terms of pressure sensors, several designs using POF are being reported. As shown in Table 1.3, sensing with two POFs with lateral offset[60, 61, 50] and POF-OTDR[3][56, 57, 58, 59] are being proposed. The main reason for the usage of POF is the cost performance (by easy light coupling and so on).

Here, a pressure sensor using the P(MMA/BzMA)POF[4] as a phase retarder fiber is proposed. The proposed sensor is an interferometric type (intrinsic) that uses a polarized DC light. Characteristic of the proposed sensor is summarized below.

1. Interferometric design (less affection of source/detector linearity)
2. Intrinsic sensor (potential to be applied for structure monitoring)
3. Requires only one fiber (existing interferometric sensors require more than two)
4. Robust light coupling (core diameter 667 μm, 62 μm for glass)
5. Using POF (can be applied for biomedical use)

The most noteworthy point in above is that the sensing requires only one fiber in which no existing fibers besides the P(MMA/BzMA)POF can accomplish this. The proposing sensor can replace the two paths of working and reference fibers by ordinary and extraordinary modes that exist within one fiber. In other words, modes are distributed into two groups that each corresponds to fast or slow optical axis that appears with a responding manner to the applied pressure. This way, the phase difference between two groups of modes interfere to a particular polarization state at the output, so the phase shift is detectable only by placing a polarizer before the power detector. Thus, the pressure sensing part is one portion of the fiber itself unlike the design using photoelastic crystal[38] (fiber itself can act like the crystal). Again, this design works only by using the P(MMA/BzMA)POF,

---

[3] optical time-domain reflectometer

[4] poly-methyl methacrylate/benzyl methacrylate copolymer plastic optical fiber

because the absence of orientational birefringence[5] and attendance of photoelastic birefringence[6] can be obtained simultaneously from P(MMA/BzMA) in a certain composition. Therefore, the proposing sensor has a simple design ever reported in addition to the beneficial characteristics of an interferometric/intrinsic sensor. In the aspect of intrinsic sensor, plastics are more elastic (opposite of brittle) than the glass[7]; thus, employment of POF may result in enhancement of the sensor sensitivity.

First, a fiber with an optimum composition was chosen by measuring extinction ratio (ER) response to the vertical stress using P(MMA/BzMA)POF with different copolymer compositions. In the latter part of the section, preliminary design of the FO pressure sensor using the P(MMA/BzMA)POF was demonstrated with a discussion of its polarimetric sensitivity and dynamic range.

7.1.1 Extinction ratio measurement under vertical pressure

ER response to the applied pressure of Fibers 1-3 (Section 4.2, Table 4.1) was measured in order to characterize the behavior of change in polarization state. 1 m test fibers were measured with the center 0.4 m involved under the applied pressure. Input polarization was tilted 45° to the pressure vector. Figure 7.1 shows the result.

The figure suggests that Fiber 2 provides a regular change in polarization state responding to the pressure. This behavior suggests a phase shifting as described in the upper part of the figure. The other two fibers do not show such periodic shifting of the ER value. Composition of Fiber 2 is considered to be the optimum as a phase retarder fiber that would be responding to a pressure in a regular manner, because it is expected to induce photoelastic birefringence in a certain magnitude while having minor affection of orientational birefringence. The other two fibers has its composition matching neither to the elimination compositions of the orientational nor the photoelastic birefringence. These fibers are expected not to be responding to the pressure in a regular manner. This is because the phase change that occurs while the light propagate down the fiber will be even more

---

[5] orientational birefringence: birefringence that has its origin in polymer chain orientation.

[6] photoelastic birefringence: birefringence that exhibit as a function of stress

[7] [Young's modules (10^9 N/m^2,GPa)] PMMA: 2.3, glass: 50-90

complicated if the two types of birefringence are both affecting in a similar magnitude. Therefore, ER measurement has supported Fiber 2 most favorable as a phase retarder POF for pressure sensing purpose.

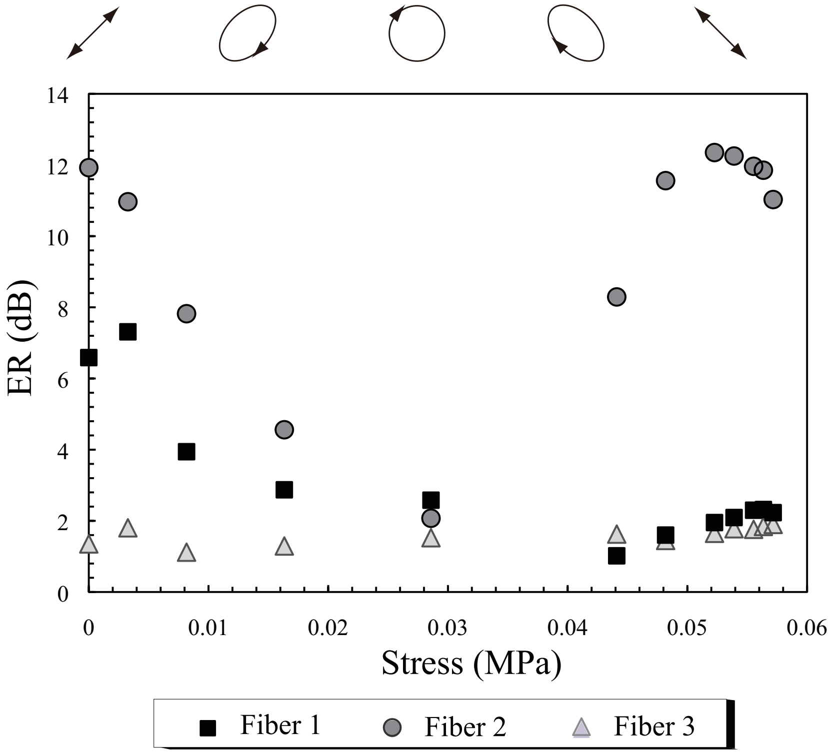

Figure 7.1: ER versus pressure plotting of Fibers 1-3 at θ_{pol}=45°. Change in state of polarization of Fiber 2 is shown in the top.

7.1.2 Retardation measurement

Soleil-Babinet compensator was used to measure the actual retardation when Fiber 2 is exposed to the pressure. Compensator scale that gives the highest ER value was considered to be the exact amount of phase difference that was compensated. Result is shown in Figure 7.2. The circle marker in the figure is the same data as shown in Figure 7.1.

As a result, ER measured with the compensator is consistent, which suggests that the phase was restored back in a good accuracy at each pressure. Retardation values are ranging around the quarter of the wavelength (158.3 nm). However, they are not showing as high periodicity than the ER values.

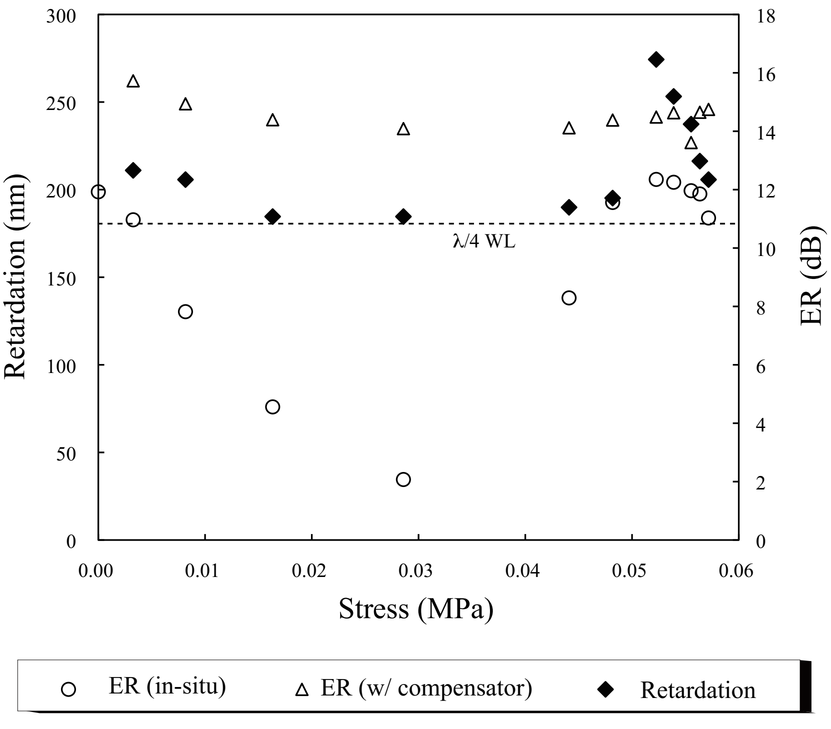

Figure 7.2: ER measurement of Fiber 2 with and without Soleil-Babinet compensator. Retardation was estimated from the compensator scale that gives the highest ER. Quarter wavelength is shown by a broken line for reference. Right and left vertical axes are ER (dB) and Retardation (nm), respectively.

7.2 Sensor design and fabrication

Pressure measurement setup was designed as described in Figure 7.3. Polarizers in parallel Nicol configuration that were oriented diagonally (45° in x_1-x_2 plane) referring to the pressure vector were placed at input and output sides of the phase retarder POF (Fiber 2). A 633 nm polarized light[8] was coupled to the fiber that was rested straight on the bottom plate (x_1-x_3 plane) with a 400-μm-diameter pinhole in between. The pinhole was in physical contact to the fiber end and positioned at the core center in order to launch dominant modes while avoiding the cladding modes. Power was monitored while changing the pressure. Acrylic boards were used for both top and bottom plates so that the two substrates have similar stiffness and the pressure from top and bottom will be similar. At the sides of the phase retarder POF, two more copolymer fibers with the same diameter (1000 μm) were rested for stabilizer purpose in order to uniformly apply the pressure from the plate. Precision weights were placed by sequence on the top plate. Summation of the applied pressure to the fiber P (Pa) was calculated using the equation below.

$$P = Wg/(3L)a, \tag{7.1}$$

where each parameters are, W (kg): applied weight, g (m/s^2): gravitational acceleration, L (m): fiber and stabilizer length involved, and a (m): fiber diameter. Here, g, L, and a are fixed values, which are, 9.8, 0.4, and 1.0 $^{-4}$, respectively. P, L, and a are illustrated in Figure 7.3.

The sensor mechanism is as described below. A phase change is induced by the photoelastic birefringence that is defined by,

$$\text{Photoelastic birefringence} = c \cdot \Delta\sigma, \tag{7.2}$$

$$\Delta\sigma \propto P \tag{7.3}$$

where $\Delta\sigma$ is difference in principal stresses (σ_1-σ_2 in Figure 7.3(a)), and c is photoelastic coefficient[84]. The fast and slow axes of the phase retarder POF is decided from the refractive

---

[8] 650 nm is the transmission window of P(MMA/BzMA)POF (Section 4.4, Figure 4.5).

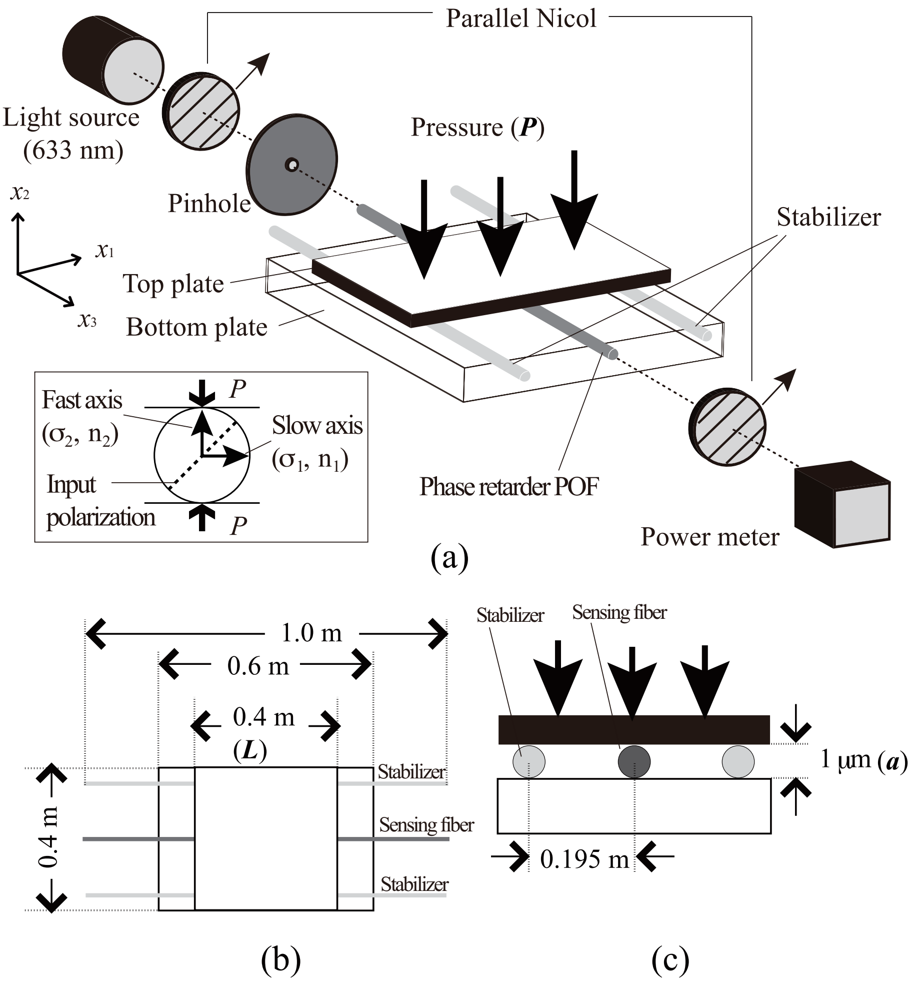

Figure 7.3: (a) Diagram of pressure measurement setup using the phase retarder POF. Angle relation of pressure vector *P*, input polarization, and fast/slow axes is shown schematically. (b) x_1-x_3 view. (c) x_1-x_2 view. Pressure is applied in -x_2 direction. Parallel-Nicol is aligned diagonally to the pressure vector.

index profile relationship to the composition that is shown in Figure 4.1 (Section 4.2, Fiber 2). The center flat part of the phase retarder POF's (Fiber 2) refractive index profile lays above the zero-photoelastic line, which means that it is off-balance to the side of BzMA rich. The sign relation of photoelastic birefringence of the PMMA and the PBzMA are negative ($c < 0$) and positive ($c > 0$), respectively[84]. Therefore, the phase retarder POF's profile suggests that it responds in a positive manner to the stress. The second polarizer filters the component that is same as the direction of input polarization, whereas a result, the phase change is detectable in power.

7.3 Performance

7.3.1 Polarimetric sensitivity

Power obtained for measurement range 0.00 to 0.06 MPa is shown in Figure 7.4. Cases when the parallel-Nicol orientation to the pressure vector was horizontal (0°) and vertical (90°) were also measured. The flat power profiles of these two measurements suggest a clean wavefront of the two groups of modes corresponding to the fast and slow axes when the parallel-Nicol is in the right angle (that is 45°).

Numerical data is shown in Table 7.1. Phase shift ϕ at each measurement plot is obtained referring to the $\phi = \pi$ that is estimated from the minimum point of the curve in Figure 7.4. Birefringence B is obtained from Eq. (7.4) with values, $\lambda = 633.3$ nm and $L = 0.4$ m. ϕ and B are listed on Table 7.1.

$$B = \frac{\phi\lambda}{2L}. \tag{7.4}$$

Plot of pressure versus birefringence is shown in Figure 7.5. Polarimetric sensitivity dB/dP is the slope of the figure, which is 3.13×10^{-5} (MPa^{-1}) at the range of 0.00 to 0.06 MPa. From the similar slope seen at the low and high pressure ranges (Figure 7.5 right), the sensor is considered to have a fairly linear response to the pressure at 0-0.06 MPa.

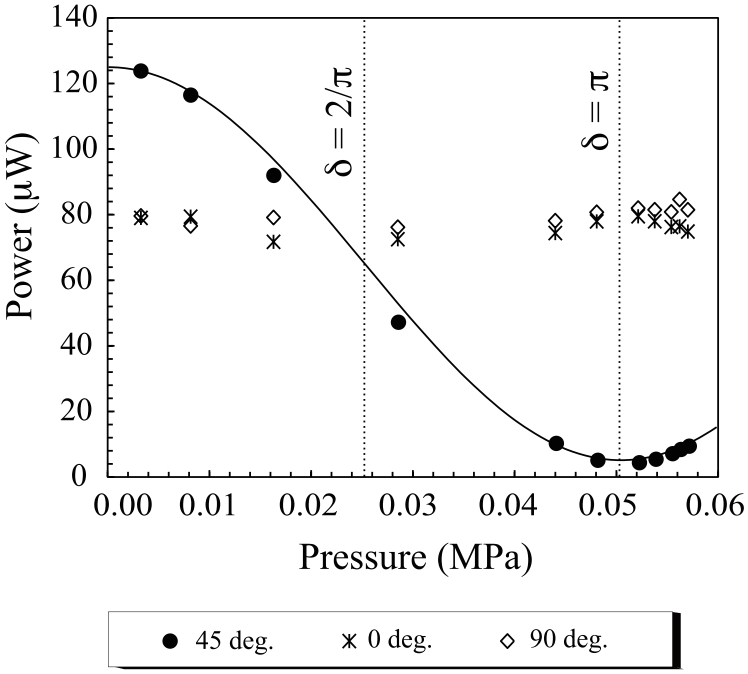

Figure 7.4: Power response to the applied pressure at 0.00 to 0.06 MPa. λ= 633.3 nm is used. Cases when the parallel-Nicol orientation to the pressure vector was horizontal (0°) and vertical (90°) was also measured.

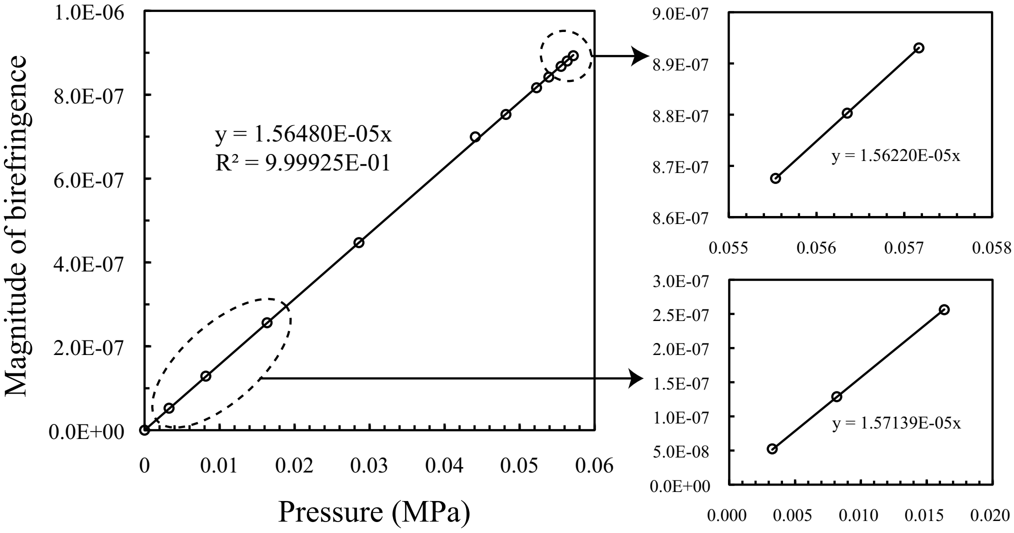

Figure 7.5: Birefringence shift at pressure change plotted for deriving polarimetric sensitivity. Obtained polarimetric sensitivity was 3.13×10^{-5} (MPa^{-1}).

Table 7.1: Numerical data of applied pressure P, obtained power, phase shift ϕ, and birefringence B. ϕ and B are values at λ= 633.3 nm

P (MPa)	Power (μW)	ϕ (π rad)	B
3.27×10^{-03}	123.8	0.0662	5.24×10^{-08}
8.17×10^{-03}	116.5	0.1627	1.29×10^{-07}
1.63×10^{-02}	92.0	0.3236	2.56×10^{-07}
2.86×10^{-02}	47.2	0.5650	4.47×10^{-07}
4.41×10^{-02}	10.3	0.8836	6.99×10^{-07}
4.82×10^{-02}	5.1	0.9511	7.53×10^{-07}
5.23×10^{-02}	4.4	1.0316	8.17×10^{-07}
5.39×10^{-02}	5.4	1.0637	8.42×10^{-07}
5.55×10^{-02}	7.1	1.0959	8.68×10^{-07}
5.64×10^{-02}	8.4	1.1120	8.80×10^{-07}
5.72×10^{-02}	9.4	1.1281	8.93×10^{-07}

7.3.2 Dynamic range

Power obtained for measurement range 0.00 to 0.47 MPa is shown in Figure 7.6. A theoretical curve calculated simply from the Malus's Law is superimposed on the plots with a broken line in Figure 7.6. The curve of Malus's Law takes the form of Eq. (7.5). Here, all kinds of optical losses and temperature affection are ignored. With the input polarization tilted $\pi/4$ radian referring to the slow (x_1) and the fast (x_2) axes, projection components to the respective directions are $A\sin(\pi/4)$ and $A\cos(\pi/4)$ in which A is the amplitude of the incident lightwave. Amplitudes of the two components that pass through the second polarizer (that is also tilted $\pi/4$ to the optical axes) are $A\sin(\pi/4)\sin(\pi/4)$ and $A\cos(\pi/4)\cos(\pi/4)$. Phase shift ϕ between x_1 and x_2 components is calculated from the polarimetric sensitivity (dB/dP) that was obtained in the earlier section. The physical

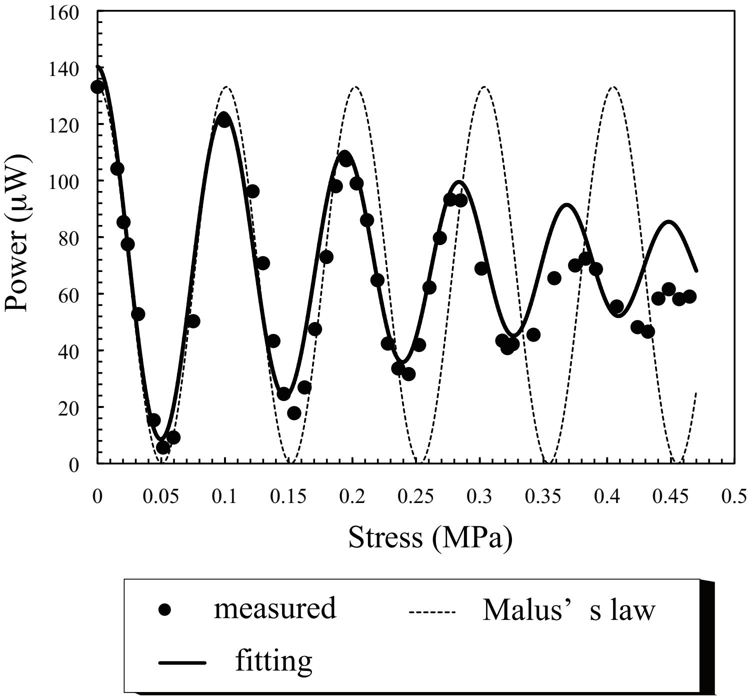

Figure 7.6: Power response to the applied pressure at the test range of 0.00 to 0.47 MPa. Plot of filled circle is the measured pressure values. Broken and solid lines are fitting of Eqs.(7.5) and (7.8) respectively.

meaning of this curve is a simple polarizer-analyzer system with an anisotropic medium that creates phase difference. As observed clearly, in comparison to the the Maul's curve, the measured curve loses the power contrast as the pressure increases. At the same time, a gradual shrinkage of oscillation pitch (means that the polarimetric sensitivity decreases) is also observed.

$$\begin{aligned} I_{\text{Malus}} &= (A\cos(\pi/4)\cos(\pi/4))^2 + (A\sin(\pi/4)\sin(\pi/4))^2 \\ &+2A^2\cos(\pi/4)\sin(\pi/4)\cos(\pi/4)\sin(\pi/4)\cos\phi. \end{aligned} \tag{7.5}$$

To characterized the measured curve, a curve obtained by modifying the last term of Eq. (eq:fitting) was superimposed on the graph with a solid line. The fitting curve takes the form of Eq. (eq:fitting2). Here, an $1/\exp^{\alpha}$ is multiplied on the last cosine and an exponent β is given on ϕ. Both α and β are function of pressure P.

$$\begin{aligned} I_{\text{fitting}} &= (A\cos(\pi/4)\cos(\pi/4))^2 + (A\sin(\pi/4)\sin(\pi/4))^2 \\ &+2A^2\cos(\pi/4)\sin(\pi/4)\cos(\pi/4)\sin(\pi/4)(\frac{1}{\exp^{\alpha}}\cos\phi^{\beta}), \end{aligned} \tag{7.6}$$

$$\alpha = \alpha(P) = P(2.5 + P^2), \tag{7.7}$$

$$\beta = \beta(P) = 1 + P^{0.08}. \tag{7.8}$$

Each of $1/\exp^{\alpha}$ and β are functioning as the role of decreasing contrast and the oscillation pitch, respectively. As a result, a fairly good match between the fitting and the measured curve was obtained.

7.4 Discussion

The optimum composition that eliminates orientational birefringence but still induces photoelastic birefringence was suggested to be 82:18 by the refractive index relationship. The periodic shift of ER value observed with the pressure gain had illustrated a clear change in polarization state in the phase retarder POF, whereas the other test fibers fabricated in different compositions did not show such property. However, birefringence measurement does not agree the above, because it indicates that Fiber 1 has the minimum birefringence among the test fibers. Retardation measurement using the compensator did not provide convincing values.

For the sensor, at 0 to 0.06 MPa, polarimetric sensitivity of 3.13×10^{-5} (MPa^{-1}) is obtained with a high reliability. It suggests that the phase change in the phase retarder POF is as stable as to be detectable only by using a polarizer. The phase retarder POF with an optimized composition has a relatively high sensitivity to pressure compared to some reported sensor fibers fabricated in glass[96, 97]. This result agrees the initial assumption that a polymeric material contributes to enhance the sensitivity because of its high elasticity.

However, the sensor performance is no longer simple after where the phase shift is larger than π as seen in Figure 7.6. The terms α, β in fitting (Eq. (eq:fitting2)) are expressing contrast drop and the inconsistency in power oscillation pitch. These factors are considered to be the effect of (1) multiple inter-modal interference that may be significant in the large-core MMF, i.e., interference at over-π retardation produces multiple states of polarization as an output because the slight phase variation among the modes becomes greater, or (2) birefringence shift regarding the change in LP_{01}^{x}, LP_{01}^{y} mode field diameter due to the fiber deformation. At around 0.45 MPa, the polarization state of the output light is considered to be practically random.

7.5 Conclusions

An intrinsic type pressure sensor using a P(MMA/BzMA)POF was fabricated with expectations of less noise and satisfactory sensitivity/dynamic range in addition to the design benefits such as simplicity, robustness, and safety.

Noise affection was considered to be sufficiently low. Sensitivity was fairly high compared to the other glass-based measurements, which agrees the initial expectation for the reason of using polymer fiber. In terms of the dynamic range, the intensity response is no longer obeying the Malus's law after a π retardation. However, a function that can predict the pressure versus intensity relationship at the high pressure range was obtained by modifying the primitive expression. Hence, an acceptable performance was demonstrated by the proposed sensor.

Chapter 8

CONCLUSIONS

The proposed work is a partial assembly of the technologies of the birefringence-reduced copolymer and the POF. The materials that are discussed in the whole dissertation are limited to MMA and BzMA, which are somewhat well known in terms of their birefringent property at either in homo/copolymer states. Similarly, POF technology employed here is not very special in terms of the fiber fabrication. The focusing point of this work is the birefringence affection to the multimodal fiber optic waveguiding, which was not done in the past. Some of the measurements are originally built and developed, such as birefringence measurement of optical fibers, ER measurement in various launching conditions, and polarimetric pressure sensing setup.

Using the nature of MMF and the two different types of birefringence that could exhibit in the plastic, polarization-maintaining and phase-retarding functions were proposed and characterized. Using both functions of the P(MMA/BzMA)POF, a pressure sensor design was proposed and characterized in terms of its polarimetric sensitivity and dynamic range. Specs of each of the above devices are summarized below.

Polarization-maintaining

The P(MMA/BzMA)POF acts as a polarization-maintaining fiber at the conditions of: (1) fiber is straightened and (2) orientational birefringence is minimized. POF fabricated in P(MMA/BzMA) demonstrated a drastically high polarization-maintaining property (14 dB) in comparison to the various kinds of known multimode fibers. At the point launching, ER was suggested to be highly affected by the local orientational birefringence. When the core center was launched, the output polarization was considered to be linear. In the case when the core edge was launched, the optical path in which the guided modes propagate reaches to the high-orientational birefringence region; thus, the initial polarization was considered to be randomized during the refraction-based waveguiding.

In the P(MMA/BzMA)POF waveguiding, ER was found to decrease parabolically from 14.0 dB to 0.9 dB as the launching position shifts from the core center to the core-cladding boundary. From the NFP and the polarized light microscopy, a correlation between birefringence of the launching point and the polarization-maintaining property was observed. With 400-μm spot diameter, ER over 13 dB was measured when the 1-m P(MMA/BzMA)POF was straightened. ER over 12 dB was ensured at the point-launching up to 50% offset of its core radius.

Evidences from all measurements supported the LP_{01} model as the polarization-maintaining principle of the P(MMA/BzMA)POF. The reduced birefringence is suggested to be preventing the degeneracy breakage. However, the Gaussian beam model still cannot be denied when considering the huge core diameter of this fiber.

Phase retarder

The idea of phase retarder fiber uses the photoelastic birefringence as the phase retarding mechanism. Macro-bending and vertical stress was suggested to be an effective method for characterizing the photoelastic birefringence in the P(MMA/BzMA)POF. ER change among different input polarization angles was observed in the P(MMA/BzMA)POF waveguiding, which was clearly in a correlation to the symmetrical axis of the macro-bending loop(s) or the stress vector. Such phenomenon was not observed at any other known MMFs. Furthermore, the ER restoration performed using a quarter-wave plate suggests that the ER degradation in P(MMA/BzMA)POF waveguiding is caused by the retardation, which is generated when the input polarization experiences the refractive index anisotropy caused by the photoelastic birefringence. Such retardation generated in a bent/pressed P(MMA/BzMA)POF was suggested to be intermodal since such ER restoration was less-efficient at the harsher macro-bending conditions. Notable point is the high regularity observed in the P(MMA/BzMA)POF waveguiding of the polarized light, which was not seen for the GI and SIPOFs. With 400-μm spot diameter, ER over 13 dB was ensured when the fiber was bent in a 10-cm-diameter loop with its input polarization either in parallel or crossed orientation to the bending plane.

ER was suggested to be less-dependent on the launching conditions when the fiber was at the macrobending than the straightened case. The output polarization state after propagating through a bent fiber was suggested to be elliptical/circular, so that it could be restored back towards linear using the QWP.

Pressure sensor

A preliminary model of fiber-optic pressure sensor using P(MMA/BzMA)POF was demonstrated. Target application of the proposed sensor is structure monitoring at biomedical scenes, which uses full advantage of fiber-optic sensor and plastic. While the conventional fiber-optic pressure sensors were using interferometry between the functioning and reference fibers, the proposing one do not require the reference fiber. Such a smart design was accomplished because of the unique characteristics of the P(MMA/BzMA)POF, which can replace the two paths of SMFs by fast and slow optical axes that exhibit in one fiber. An interferometry requires sensitive installation of coupler and splitter, but the proposing design using P(MMA/BzMA)POF requires only two sets of polarizers, which is very simple. In addition, the large core diameter (667 μm, whereas SMF is less than 10 μm) contributes for improving the robustness in terms of the light coupling.

As a result, the measured intensity had a regular response to the pressure at 0 to 0.06 MPa. Polarimetric sensitivity obtained from that pressure range was 1.56×10^{-5} (MPa^{-1}) which was relatively high. At the higher pressure, contrast and oscillation pattern of power had degraded gradually. This phenomenon was considered to be the effect of (1) the interference between multiple wavefront, (2) change in birefringence slope due to the fiber deformation, (3) or their combination. Despite few unclear points and fluctuation of repeatability of the first model, the total performance is considered to be sufficient to claim the validity of this design.

FURTHER WORKS

This final section lists up some of the points that the author still considers to be insufficiently investigated or improvable.

→ 82:18 was claimed to be the optimum for minimizing orientational birefringence, just like films and tablets, but also for the POF core. Refractive index profile and ER measurements had shown supporting results to the above statement, however, the birefringence measurement do not agree this. The comparison of refractive index profile and birefringence (Figures 4.1 and 4.2) clearly tells this concern. The author's publication in JJAP (full journal paper) slightly discusses about this point with some emphasis that it is an ”assumption,” and there is no laboratory evidence to support it. Room temperature quenching right after the heat draw is one factor that is likely to be the answer for it.

→ The effort to measure fiber retardation using Soleil-Babinet compensator is said to be failed. Although it precisely restores the phase difference, the scales are not trustable. In fact, when the author was doing this measurement, it had relatively poor repeatability. A recommendation that might help to improve this point is to turn the scale only in one direction. Switching clockwise and counterclockwise probably disturbs the crystal overlap in some way.

→ The polarization-maintaining property was not investigated enough in terms of the difference in refractive index profile. In particular, polarization-maintaining property was said to be high because the copolymer fiber is a GI MMF instead of SI. However, actually, the SIPOF of Mitsubishi Rayon that was used for comparison had some birefringence in the order of $\times 10^{-4}$, which is too high to compare with the copolymer. Total reflection of straight ray paths and refraction-based waveguiding were not precisely compared. In order to clarify this point, a GI fiber with a similarly high birefringence needs to be prepared. That is said to be challenging, because the graded concentration of either the dopant or copolymer is the requirement but also acts to affect the birefringence uniformity. Any dopant molecule or copolymers that has nothing to do with birefringence reduction needs to be chosen for such case.

→ The molecule-doped GIPOF that was used for comparison did not show as high ER as the copolymer fiber, however, the difference in birefringence values are said to be very minor compared to the difference in ER. In addition, a low-birefringent GI fiber using molecule dopants could be fabricated if the draw tension was kept very low. Although not included in this dissertation, some of the experiments that the author carried out in terms of the draw tension suggested that it is impossible to obtain ER over 7 dB using the GI fiber with molecule dopants even with a very loose drawing. This point suggests that birefringence in directions other than vertical and horizontal may be needed to be characterized. Perhaps, the method to measure birefringence in the optical fiber might need to be improved.

→ When taking images by polarized optical microscope using tint plate, the periodic change in color may cause misunderstanding to the auditor/reviewer about the magnitude of birefringence. May be convenient if some image processing software could convert all the colors.

→ Up to now, amount of phase difference is successfully measured using the pressure sensing setup. It is strongly recommended to find some way to distinguish the ”point” where the pressure was applied. The author used 1 m fiber and different kinds of plates (40 x 40, 60 x 40, and 80 x 40 (cm)) to press it, but no special difference was observed in terms of the involved length (length under the pressure). Some combination of partial mode launching and local application of pressure (e.g., 10 cm) may be effective. Later it is also recommended to use the pulse instead of DC.

LIST OF PUBLICATIONS

1 R. Furukawa, A. Tagaya, S. Iwata, and Y. Koike, ”*Waveguiding Property of a Plastic Optical Fiber Fabricated Using Low-Birefringence Copolymer,*” Japanese Journal of Applied Physics, Vol. 46, No. 47, L1182- L1184 (2007).

2 R. Furukawa, A. Tagaya, S. Iwata, and Y. Koike, ”*Polarization-Maintaining Mechanism of a Birefringence-Reduced Plastic Optical Fiber Fabricated Using Poly(methyl methacrylate/benzyl methacrylate) Copolymer,*” The Journal of Physical Chemistry C, Vol. 112, pp. 7946-7952 (2007).

3 R. A. Furukawa, A. Tagaya, and Y. Koike, ”*Modal analysis of a multimode polarization-maintaining plastic optical fiber fabricated using poly(methyl methacrylate/benzyl methacrylate) copolymer,*” Applied Physics Letters, Vol. 93, No. 10, 103303/1-3 (2008).

4 R. A. Furukawa, A. Tagaya, and Y. Koike, ”*Differential mode analysis of a polarization-maintaining graded-index plastic optical fiber using macrobending,*” Japanese Journal of Applied Physics, accepted for publication.

International conferences

1 R. A. Furukawa*, A. Tagaya, S. Iwata, and Y. Koike, ”*Design of a polarization maintaining graded index plastic optical fiber by random co-polymerization,*” 16th International Conference of Plastic Optical Fiber, Turin, Italy, September 11, 2007

2 R. Furukawa*, A. Tagaya, and Y. Koike, ”*Mode-selective Extinction Ratio Measurement of a Polarization-Maintaining Graded Index Plastic Optical Fiber Based on a Poly-(Methylmethacrylate/Benzylmethacrylate) Copolymer,*” 17th International Conference of Plastic Optical Fiber, Santa Clara, USA, August 27, 2008

BIBLIOGRAPHY

[1] J. A. Brydson, *Plastic Materials*. Butterworth Scientific, London, UK, 1982.

[2] B. B. Kine and R. W. Novak, *In Encyclopedia of Polymer Science and Engineering, 2nd ed.*, vol. 1. Wiley, New York, 1986.

[3] M. Yamaguchi and K. Masuzawa, “Birefringence control for binary blends of cellulose acetate propionate and poly(vinyl acetate),” *European Polymer Journal*, vol. 43, pp. 3277–3282, August 2007.

[4] A. Tagaya, H. Ohkita, T. Harada, K. Ishibashi, and Y. Koike, “Zero-birefringence optical polymers,” *Macromolecules*, vol. 39, pp. 3019–3023, Apr 2006.

[5] Y. Koike, K. Yamazaki, H. Ohkita, and A. Tagaya, “Zero-birefringence optical polymer by birefringent crystal and analysis of the compensation mechanism,” in *Macromolecular Symposia*, vol. 235, pp. 64–70, 2006.

[6] A. Tagaya, H. Ohkita, T. Harada, K. Ishibashi, and Y. Koike, “Zero-birefringence optical polymers,” *Macromolecules*, vol. 39, no. 8, pp. 3019–3023, 2006.

[7] A. Tagaya, H. Ohkita, M. Mukoh, R. Sakaguchi, and Y. Koike, “Compensation of the birefringence of a polymer by a birefringent crystal,” *Science,*, vol. 301, pp. 812–814, Aug 2003.

[8] E. Nihei, T. Ishigure, and Y. Koike, “Optimization of modal and material dispersions in high-bandwidth graded-index polymer optical fiber,” in *ACS Symposium Series*, vol. 672, pp. 58–70, 1997.

[9] S. Takahashi and S. K. Ichimura, “Time domain measurements of launching-condition-dependent bandwidth of all-plastic optical fibres,” *Electronics Letters*, vol. 27, pp. 217–21, Jan 1991.

[10] K. Takahashi, T. Ishigure, and Y. Koike, “Index profile design for high-bandwidth w-shaped plastic optical fiber,” *Journal of Lightwave Technology*, vol. 24, pp. 2867–2876, July 2006.

[11] Y. Ebihara, T. Ishigure, and Y. Koike, “Low dispersion perfluorinated polymer based graded index polymer optical fiber,” in *Polymer Preprints, Japan*, vol. 54, p. 1352, 54th SPSJ Annual Meeting 2005, 2005.

[12] T. Ishigure, Y. Aruga, and Y. Koike, “High-bandwidth pvdf-clad gi pof with ultra-low bending loss,” *Journal of Lightwave Technology*, vol. 25, pp. 335–345, January 2007.

[13] S. E. Golowich, W. White, W. A. Reed, and E. Knudsen, “Quantitative estimates of mode coupling and differential modal attenuation in perfluorinated graded-index plastic optical fiber,” *Journal of Lightwave Technology*, vol. 21, pp. 111–121, January 2003.

[14] Kajiwara *O plus E (Japanese)*, vol. 84, September 1982.

[15] Y. Namihira, Y. Ejiri, and K. Mochizuki, “Birefringence in elliptical-cladding single-polarisation fibres,” *Electronics Letters*, vol. 18, pp. 89–91, January 1982.

[16] T. Okoshi, “Single-polarization single-mode optical fibers,” *IEEE Journal of Quantum Electronics*, vol. QE-17, pp. 879–884, JUNE 1981.

[17] H. Yoshida, Y. Kikuchi, and Y. Tamaki, “0. 63um polarization maintaining optical fiber cable,” in *Proceedings of International Wire and Cable Symposium*, pp. 415–420, 1986.

[18] M. P. Varnham, D. N. Payne, R. D. Birch, and E. J. Tarbox, “Single-polarization operation of highly birefringent bow-tie optical fibers.,” *Electronics Letters*, vol. 19, pp. 42–44, Mar 1983.

[19] V. Ramaswamy, R. H. Stolen, M. D. Divino, and W. Pleibel, “Birefringence in elliptically clad borosilicate single-mode fibers.,” *Applied Optics*, vol. 18, pp. 4080–4084, Dec 1979.

[20] M. J. Adams, D. N. Payne, and C. M. Ragdale, “Birefringence in optical ffibers with elliptical cross-section,” *Electronics Letters*, vol. 15, pp. 298–299, May 1979.

[21] J. D. Love, S. R. A., and A. W. Snyder, “Birefringence in elliptically deformed optical fibers,” *Electronics Letters*, vol. 15, pp. 615–616, Sep 1979.

[22] N. Imoto, N. Yoshizawa, J. I. Sakai, and H. Tsuchiya, “Birefringence in single-mode optical fiber due to elliptical core deformation and stress anisotropy.,” *IEEE Journal of Quantum Electronics*, vol. QE-16, pp. 1267–1271, Sept 1980.

[23] M. Tanaka and S. Kawanishi, “Fabrication of dispersion controlled and polarization maintaining photonic crystal fiber for high performance systems and devices,” vol. 3, pp. 6–11, Optical Fiber Communication Conference, 2005. Technical Digest. OFC/NFOEC, March 2005.

[24] P. S. J. Russell, “Photonic crystal fibers,” *Science*, vol. 299, pp. 358–362, 2003.

[25] K. Hansen, “Highly nonlinear photonic crystal fiber with zero-dispersion at 1.55pm,” OFC2002, postdeadline paper, 2002.

[26] S. Kawanishi and K.Okamoto, “Polanzation maintaining holey optical fiber (in japanese),” IE1CE Soc.Conf., 2000.

[27] A. Ortigosa-Blanch, J. C. Knight, W. J. Wadsworth, J. Arriaga, B. J. Mangan, T. Birks, and P. S. J. Russell, “Highly birefringent photonic crystal fibers,” *Optics and Photonics News*, vol. 12, p. 17, December 2001.

[28] K. Suzuki, H. Kubota, S. Kawanishi, M. Tanaka, and M. Fujita, “High-speed bi-directional polarisation division multiplexed optical transmission in ultra low-loss (1.3 db/km) polarisation-maintaining photonic crystal fibre,” *Electronics Letters*, vol. 37, pp. 1399–1401, Nov 2001.

[29] D. N. Payne, A. J. Barlow, J. J. Ramskov-Hansen, M. R. Hadley, and R. J. Mansfield, “Fabrication and properties of low birefringence spun fibers.,” in *Fiber-Optic Rotation Sensors and Related Technologies, Proceedings of the 1st International Conference.*, vol. 32, pp. 185–195, 1982.

[30] M. J. Li and D. A. Nolan, “Fiber spin-profile designs for producing fibers with low polarization mode dispersion,” *Optics Letters*, vol. 23, pp. 1659–1661, Nov 1998.

[31] R. E. Schuh, X. Shan, and A. S. Siddiqui, “Polarization mode dispersion in spun fibers with different linear birefringence and spinning parameters,” *Journal of Lightwave Technology*, vol. 16, pp. 1583–1588, Sep 1998.

[32] W. Yong and C. Xu, “Spun fiber bragg grating sensors with strong resistance to transverse pressure,” in *Lasers and Electro-Optics Society Annual Meeting-LEOS, 19th Annual Meeting of the IEEE Lasers and Electro-Optics Society, LEOS*, pp. 368–369, 2007.

[33] W. Daum, J. Krauser, P. E. Zamzow, and O. Ziemann, *POF-Polymer Optical Fibers for Data Communication*. Springer-Verlag Berlin Heidelberg New York, 2002.

[34] G. P. Agrawal, *Fiber-Optic Communication Systems*. John Wiley & Sons, Inc., New York., 3 ed., 2002.

[35] S. Iwata, H. Tsukahara, E. Nihei, and Y. Koike, “ero birefringence polymer and analysis of orientation function,” in *Polymeric Materials Science and Engineering, Proceedings of the ACS Division of Polymeric Materials Science and Engineering* (P. of the 1996 Fall ACS Meeting, ed.), vol. 75, p. 321, Aug 1996.

[36] J. D. Muhs, “Fiber optic sensors: Providing cost-effective solutions to industry needs.” http:\\otrc.tamu.edu\Pages\Fiber%20Optics%20Strain%20Gages.pdf.

[37] K. Kyuma and M. Nunoshita, *Hikarifaiba sensa (Japanese)*. Jyouhouchousakai, S60.

[38] J. W. B. Spillman, “Multimode fiber-optic pressure sensor based on the photoelastic effect,” *Optics Letters*, vol. 7, no. 8, pp. 388–390, 1982.

[39] B. E. Jones, “On the jones birefringence.,” in *Proceedings of The Royal Society of London, Series A: Mathematical and Physical Sciences*, vol. 390, pp. 73–90, Nov 1983.

[40] R. T. Murray, “Family of grating sensors.,” in *IEE Conference Publication*, no. 221, pp. 114–116, 1983.

[41] J. A. Bucaro and J. H. Cole, “Acousto-optic sensor development,” in *Proc. IEEE Electronics and Aerospace Systems Conf., Pt. III* (N. Y. IEEE, ed.), p. 572, EASCON, 1979.

[42] G. A. Rines, “Fiber-optic accelerometer with hydrophone applications,” *Applied Optics*, vol. 20, no. 19, pp. 3453–3459, 1981.

[43] J. N. Fields, C. K. Asawa, O. G. Ramer, and M. K. Barnoski, “Fiber optic pressure sensor.,” *Journal of the Acoustical Society of America*, vol. 67, pp. 816–818, Mar 1980.

[44] E. Pinet, E. Cibula, and D. Donlagic, “Ultra-miniature all-glass fabry-perot pressure sensor manufactured at the tip of a multimode optical fiber,” in *Proceedings of SPIE*, vol. 6770, p. 67700U, Fiber Optic Sensors and Applications V, SPIE, Sep 2007.

[45] J. D. Prohaska, E. Snitzer, B. Chen, M. H. Maher, E. G. Nawy, and W. W. Morey, “iber optic bragg grating strain sensor in large-scale concrete structures,” in *Proceedings of SPIE*, vol. 1798, pp. 286–294, Fiber Optic Smart Structures and Skins V, Sep 8-9 ::H:1992:H::, Boston, MA, USA, 1993.

[46] G. P. Agrawal, *Nonlinear Fiber Optics*. Optics and Photonics, 525 B Street, Suit 1900, San Diego, CA, 92101-4495, USA: Academic Press, San Diego, CA, 3rd ed., 2001.

[47] M. Kihara and H. Ohno, “Distributed optical fiber sensor using brillouin scattering,” in *Post-conference Digest*, vol. 88, pp. 1918–1919, OSA Trends in Optics and Photonics Series, Conference on Lasers and Electro-Optics (CLEO), 2003.

[48] H. Ohno, H. Naruse, N. Yasue, Y. Miyajima, H. Uchiyama, Y. Sakairi, and Z. X. Li, “evelopment of highly stable botdr strain sensor employing microwave heterodyne detection and tunable electric oscillator,” in *Proceedings of SPIE*, vol. 4596, pp. 74–85, Advanced Photonic Sensors and Applications II, Nov 2001.

[49] M. Lomer, A. Galindez, A. Quintela, and J. M. Lopez-Higuera, “Continuous liquid level sensor using plastic optical fibers and hollow metallic waveguides,” in *The 17th International Conference on Plastic Optical Fibers*, 2008.

[50] M. Oliverto, G. Perrone, A. Vallan, S. Abrate, V. Cacciatore, G. Perale, and A. Perale, “Plastic optical fiber based sensing system for crack monitoring,” in *The 17th International Conference on Plastic Optical Fibers*, 2008.

[51] M. M. Werneck, E. S. Yugue, F. L. Maciel, J. L. Silva-Neto, C. C. Carvalho, and M. A. L. Miguel, “Application of a pof and ruby florescence based temperature system in an electric power substation,” in *The 17th International Conference on Plastic Optical Fibers*, 2008.

[52] M. Komatsu, S. Honma, M. Morisawa, and S. Muto, “Gas sensing system with pof humidity calibrator,” in *The 17th International Conference on Plastic Optical Fibers*, 2008.

[53] C. Kai, S. Honma, M. Honma, and S. Muto, “Bedridden prople’s condition monitor using pof moisture sensors,” in *The 17th International Conference on Plastic Optical Fibers*, 2008.

[54] J. Vaughan, C. Woodyatt, P. Scully, and K. Persaud, “Polymer optical fibre sensor to monitor skin moisture and perspiration,” in *The 16th International Conference on Plastic Optical Fibers*, 2007.

[55] G. Emiliyanov, O. Bang, P. Hoiby, L. H. Pedersen, E. M. Kjaer, and L. Lindvold, “Multi-antibody biosensing with topas microstructured polymer optical fiber,” in *The 16th International Conference on Plastic Optical Fibers*, 2007.

[56] K. Kreber, P. Lenke, S. Liehr, J. Witt, M. Schauker, M. Large, and T. Theil, “Technolog and applications of smart tchnical textiles based on pof,” in *The 17th International Conference on Plastic Optical Fibers*, 2008.

[57] S. Liehr, P. Lenke, M. Wendt, and K. Krebber, “Perfluorinated graded-index polymer optical fibers for distributed measurement of strain,” in *The 17th International Conference on Plastic Optical Fibers*, 2008.

[58] P. Lenke, S. Liehr, and K. Krebber, “The 17th international conference on plastic optical fibers,” in *2008*.

[59] J. Witt, C.-A. Bunge, M. Schukar, and K. Krebber, “Real-time strain sensing based on pof otdr,” in *The 16th International Conference on Plastic Optical Fibers*, 2007.

[60] G. Durana, M. Kirchof, M. L. S. de Ocariz, H. Poisel, J. Zubia, G. Aldabaldetreku, and C. Vazquez, “Installation and performance of a polymer optical fiber-based elongation sensor,” 2008.

[61] H. Lame and D. Gallego, “Ultrsound interferometric plastic optical fiber (pof) sensors for optoaccoustic biomedical imaging,” in *The 17th International Conference on Plastic Optical Fibers*, 2008.

[62] D. C. Lee, J. J. Lee, I. B. Kwon, and D. C. Seo, “Monitoring of fatigue damage of composite structures by using embedded intensity-based optical fiber sensors,” *Smart Materials and Structures*, vol. 10, pp. 285–292, April 2001.

[63] G. N. Harbach, H. G. Limberger, and R. P. Salathe, “Uv induced fiber bragg gratings (fbg) written in fully polymerized polymer optical fibers (pof),” in *The 16th International Conference on Plastic Optical Fibers*, 2007.

[64] J. Yu, X. Tao, and H. Tam, “Trans-4-stilbenemethanol-doped photosensitive polymer fibers and gratings,” *Optics Letters*, vol. 29, p. 156, 2004.

[65] Z. Xiong, G. D. Peng, B. Wu, and P. L. Chu, “Highly tunable bragg gratings in single-mode polymer optical fibers,” *IEEE Photonics Technology Letters*, vol. 11, pp. 352–354, Mar 1999.

[66] M. Born and E. Wolf, *Principle of Optics*. Cambridge University Press, New York, 7th ed., 1999.

[67] Okamoto, *Hikaridouharo no kiso (Japanese)*. Korona-sha, 1992.

[68] P. Diament, *Wave Transmission and Fiber Optics*. Macmillan, New York, 1990.

[69] A. W. Snyder and J. D. Love, *Optical Waveguide Theory*. Chapman & Hall, London, 1983.

[70] M. Abramowitz and I. A. Stegun, *Handbook of Mathematical Functions*. Dover, New York, 1970.

[71] D. Marcuse, *Theory of Dielectric Optical Waveguides*. Academic Press, San Diego, CA, 2 ed., 1991.

[72] G. Cancellieri, *Single-Mode Optical Fibers*. Pergamon Press, Elmsford, NY, 1991.

[73] J. A. Buck, *Fundamentals of Optical Fibers*. Wiley, New York, 1995.

[74] Ohkoshi, Okamoto, and Hotate, *Hikari faiba (in Japanese)*. Ohm-sha, 1983.

[75] D. Gloge, “Weakly guiding fiber,” *Applied Optics*, vol. 10, pp. 2252–2258, Oct 1971.

[76] L. B. Jeunhomme, *Single-Mode Fiber Optics*. Marcel Dekker, New York, 1990.

[77] Sakakibara, *Kouhakougaku (in Japanese)*. Korona-sha, 1998.

[78] Wikipedia, “Gaussian beam.”

[79] Sam, “Sam’s laser faq.” http:\ \an.hitchcock.org\repairfaq\sam\laserfil.htm.

[80] Y. Koike and A. Tagaya, *Advanced Polymeric Materials One Point1, Photonics Polymer*. Kyoritsu Press, 2004.

[81] S. O. Kasap, *Optoelectronics and photonics: Principles and Practices*. Prentice-Hall, Inc. Upper Saddle River, NJ 07458, 2001.

[82] J. F. Nye, *Physical Properties of Crystal*. Oxford University Press, 1957, 1985.

[83] H. Ohkita, *Synthesis of Zero-Birefringence Optical Polymers and Analysis of the Generation Mechanism of Birefringence in Polymers*. PhD thesis, Integrated Design Engineering, H16.

[84] A. Tagaya, H. Ohkita, T. Harada, K. Ishibashi, and Y. Koike, “Zero-birefringence optical polymers,” *Macromolecules*, vol. 39, no. 8, pp. 3019–3023, 2006.

[85] S. Iwata, *Zero-Birefringence Optical Polymer*. PhD thesis, Integrated Design Engineering, H8.

[86] T. Harada, “Zero-zero birefringence optical polymer,” Master’s thesis, Integrated Design Engineering, H18.

[87] Wikipedia, “Iridescence.”

[88] N. M. Bityurin, V. N. Genkin, V. P. Zubov, and M. B. Lachinov, “On the gel-effect mechanism in radical polymerization,” *Polymer Science USSR*, vol. 23, no. 8, pp. 1873–1882, 1981.

[89] Y. Ohtsuka and Y. Koike, “Determination of the refractive-index profile of light-focusing rods: accuracy of a method using interphako interference microscopy,” *Applied Optics*, vol. 19, no. 26, pp. 2866–2872, 1980.

[90] U. of Cambridge, “Doitpoms teaching and learning packages.” http:\\www.doitpoms.ac.uk\tlplib\optical-microscopy\plates.php.

[91] Olympus, “Berek compensator.” pamphlet; Polarized optical microscope DP70.

[92] H. Endo, “W-shaped polymer optical fiber,” Master’s thesis, Integrated Design Engineering, H15.

[93] K. Ohdoko, “Propagating modes characterization and design for the optimum waveguiding in a graded-index polymer optical fiber,” Master’s thesis, Integrated Design Engineering, H14.

[94] Y. Ishiyama, “Design of waveguide structure and mode coupling management in gi pof,” Master’s thesis, Integrated Design Engineering, H18.

[95] F. T. Inc., “Fiso technologies inc. - fiber optic sensors & solutions.” http:\\www.fiso.com\index.php?module=CMS&func=view&id=105.

[96] H. K. Gahir and D. Khana, “Design and development of a temperature-compensated fiber optic polarimetric pressure sensor based on photonic crystal fiber at 1550 nm,” *Applied Optics*, vol. 46, no. 8, pp. 1184–1189, 2007.

[97] J. Chen and W. J. Bock, “A novel fiber-optic pressure sensor operated at 1300-nm wavelength,” *IEEE Transactions on Instrumentation and Measurement*, vol. 53, pp. 10–14, Feb 2004.